TRANSITIONING FROM BENCHTOP TO POINT-OF-CARE FOR EARLY DETECTION OF PREECLAMPSIA USING MICRORNA

A Dissertation

by

MONIKA BALBINA SCHECHINGER

Submitted to the Office of Graduate and Professional Studies of
Texas A&M University
in partial fulfillment of the requirements for the degree of

DOCTOR OF PHILOSOPHY

Chair of Committee,	Gerard L. Coté
Co-Chair of Committee,	Samuel Mabbott
Committee Members,	Mahua Choudhury
	Vladislav V. Yakovlev
Head of Department,	Mike McShane

May 2020

Major Subject: Biomedical Engineering

ABSTRACT

Preeclampsia is a condition that develops late in pregnancy and accounts for 75,000 maternal and 500,000 newborn deaths each year. Preeclampsia is commonly identified late in pregnancy using a generalized symptoms-based approach. Treatment options are limited at this stage. As such, this work investigated an alternative approach for diagnosing preeclampsia through the development of a diagnostic test for epigenetic biomarkers—i.e., miRNA-17 and miRNA-20a—associated with the onset of preeclampsia. The upregulation of these miRNAs occurs around the 9th week of pregnancy, inducing gene expression which causes the onset of symptoms that evolve into preeclampsia. A diagnostic tool was developed to pinpoint these biological changes by quantitatively determining the concentration of miRNA-17 and miRNA- 20a. This was achieved using an adapted split sandwich assay, 3D paper fluidics, Raman reporter labeled and functionalized gold nanoparticles, and surface enhanced Raman spectroscopy (SERS). The assay was incorporated into a 3D paper fluidic platform that uses both lateral and vertical flow. This design ensures that assay-specific sensing reagents and buffers are stored within the paper fluidic platform, which, in turn, promotes the binding of nanoparticles with miRNA-17 and miRNA-20a in solution for ultimate detection. The resultant SERS signal produced by the assay was analyzed using a handheld Raman system. The results were then used to quantify miRNA-17 and miRNA-20a concentrations ranging from 100 pM to 100 fM in solution.

DEDICATION

To my mom Dorota, my dad Marek, and my sister Caroline for always supporting me and reminding me to always put my heart and soul into my work. You all have been my rock and I will never forget how you have been there for me throughout this process. Mom, thank you for always listening to me and picking up all my phone calls. Because I knew that I could always call you, I knew I was never alone, and you helped me from getting lost. Most importantly you always reminded me to be true to myself. Dad, thank you for sparking my interest in and pointing me in the direction of research. You have always seen the potential in me even when I was unaware. I will cherish always your enthusiasm for my research and the many questions you ask about it. Caroline, thank you for being my "editor" and constantly reminding me of my character and merit. Your grit and determination will always be an inspiration to me; thank you for showing me that anything is achievable with a lot of hard work. Finally, a separate thanks goes to Theo for his unconditional love and loyalty. I'll always be grateful for your boundless energy that has powered me through many all-nighters.

ACKNOWLEDGEMENTS

First and foremost, I would like to thank my chair Dr. Gerard Coté for providing me with the opportunity to perform this research. I am indebted to you for all your mentorship and guidance. Your support of my candidacy has been invaluable to me, and I am so grateful for your critical eye and willingness to troubleshoot issues with me at every step in the process. Thank you also to my co-chair, Dr. Samuel Mabbott, for mentoring me throughout my time in Scotland at the University of Strathclyde and later on in the United States.

I would also like to acknowledge my committee members. Dr. Mahua Choudhury, thank you for introducing me to such a meaningful area of clinical research. Your insight and support have been so helpful throughout this process. Our lively discussions have helped deepen my understanding of my work, which has benefited a great deal from your expertise in epigenetics and preeclampsia. Finally, Dr. Vladislav Yakovlev, thank you for helping me improve my understanding of optics and mentoring me throughout my research career.

Separately, a hearty thanks to my colleagues in the Biomedical Engineering Department at Texas A&M and my lab mates in the Optical BioSensing Lab. I am grateful in particular to Dr. Haley Marks for first introducing me to Raman spectroscopy. I would also like to acknowledge my undergraduates, Lauren Kwiatkowski and Jacob Powell for their help in running these experiments.

CONTRIBUTORS AND FUNDING SOURCES

Contributors

This work was supervised by a dissertation committee consisting of my chair Dr. Gerard Coté, co-chair Dr. Samuel Mabbott, and member Dr. Vladislav Yakovlev of the Department of Biomedical Engineering and Dr. Mahua Choudhury of the Pharmacy Department.

The qRT-PCR analysis of the bovine serum in Chapter 3 was provided by Dr. Min Hi Park of the Pharmacy Department and was published in 2019. Data analyses provided in Chapter 4 were conducted in part by undergraduate research assistant, Lauren Kwiatkowski, with the aid of Jacob Powell from the Department of Biomedical Engineering.

All other work conducted for the dissertation was completed by the student independently.

Funding Sources

Graduate study was supported by a fellowship from Texas A&M University and Texas A&M Engineering Experiment Station.

This work was also made possible in part by the Texas A&M Health Sciences Research, Award no. 10072-2, and the Discovery Foundation. Its contents are solely the responsibility of the authors and do not necessarily represent the official views of the Texas A&M Health Sciences Department and Discovery Foundation.

NOMENCLATURE

A	Adenine
Abs	Absorbance
Ag	Silver
AgNPs	Silver Nanoparticles
ANOVA	Analysis of Variance
Au	Gold
AuNPs	Gold Nanoparticles
BSA	Bovine Serum Albumin
C	Cytosine
c	Concentration
CCD	Charge-Coupled Device
Cl	Chloride
cm	Centimeter
COD	Coefficient of Determination
CV	Coefficient of Variation
DDW	Deionized Distilled Water
DLS	Dynamic Light Scattering
DNA	Deoxyribonucleic Acid
dsDNA	Double Stranded DNA
DTNB	5,5-dithio-bis-(2-nitrobenzoic acid)

fM	Femtomolar
G	Guanine
H	Hydrogen
h	Hour
$HAuCl_4$	Chloroauric Acid
HCl	Hydrochloric Acid
HEG	Hexaethylene Glycol
IVD	*In-vitro* Diagnostics
k_d	Apparent Dissociation Constant
kDa	Kilodalton
I_{LIMIT}	Intensity Limit
L	Liter
l	Path Length
Laser	Light Amplification by Stimulated Emission of Radiation
LFA	Lateral Flow Assay
LNA	Locked Nucleic Acid
LOD	Limit of Detection
LOQ	Limit of Quantification
LSP	Localized Surface Plasmon
LSPR	Localized Surface Plasmon Resonance
M	Molar
m	Meter

miRNA	microRNA
MGITC	Malachite Green Isothiocyanate
min	Minutes
mL	Milliliter
mm	Millimeter
ms	Millisecond
mV	Millivolt
mW	Milliwatt
n	Hill Coefficient
N	Nitrogen
Na	Sodium
NA	Numerical Aperture
NC	Nitrocellulose Membrane
NIR	Near-Infrared
nm	Nanometer
nM	Nanomolar
NP	Nanoparticle
NTA	Nanoparticle Tracking Analysis
O	Oxygen
OD	Optical Density
oligos	Oligonucleotides
p	Probability Value

PBS	Phosphate Buffered Saline
PCR	Polymerase Chain Reaction
PE	Preeclampsia
PEG	Poly(ethylene) Glycol
POC	Point-of-Care
POCT	Point-of-Care Technology
pM	Picomolar
PNA	Peptide Nucleic Acids
qRT-PCR	Quantitative Reverse Transcription-Polymerase Chain Reaction
R	Correlation Coefficient
rcf	Relative Centrifugal Force
RGB	Red Green Blue
rpm	Revolutions Per Minute
RT-PCR	Reverse Transcription-Polymerase Chain Reaction
RNA	Ribonucleic Acid
RRM	Raman Reporter Molecule
s	Seconds
SAM	Self-Assembling Monolayers
SDEV	Standard Deviation
SERS	Surface-Enhanced Raman Spectroscopy
ssDNA	Single-Stranded DNA
T	Thymine

TCEP	Tris(2-carboxyethyl) phosphine
TEM	Transmission Electron Microscopy
TRITC	Tetramethyl Rhodamine Isothiocyanate
U	Uracil
UV-Vis	Ultraviolet-Visible Spectrophotometry
V	Volt
VFA	Vertical Flow Assay
v/v	Volume Per Volume
W	Watt
WHO	World Health Organization
w/v	Weight Per Volume
2D	Two-Dimensional
3D	Three-Dimensional
3’	Three Prime
5’	Five Prime
α	Significance Level
ε_λ	Molar Absorptivity/ Molar Extinction Coefficient
λ	Wavelength
λ_{max}	Absorption Maximum
µL	Microliter
µM	Micromolar

TABLE OF CONTENTS

Page

LIST OF FIGURES

Page

LIST OF TABLES

Page

CHAPTER I

INTRODUCTION

The success of humankind, from an evolutionary perspective, is dependent on our survival and advancement throughout the years. Each generation faces a new set of challenges which test our capacity for innovation. At the forefront of these challenges are issues surrounding our health and wellbeing.[1] On this front, advancements in medical devices and diagnostics in recent years have played a crucial role in improving quality of life and healthcare practices.

In particular, our current healthcare system depends on the accurate and timely diagnosis of disease. Despite recent advances, we need more technologies to diagnose diseases based on real-time information relating biological markers, i.e., biomarkers, to the existence or onset of disease. This technology has great promise in developing diagnostic tests for diseases such as preeclampsia that are difficult to diagnose early on, when treatment may be most effective.

I.1 What is Preeclampsia?

I.1.i Influence of Preeclampsia Worldwide

Preeclampsia is a hypertensive, multisystem disorder during pregnancy[2] that is connected to abnormal placentation through atypical formation of uterine arteries potentially causing endothelial dysfunction, oxidative stress, and systemic inflammation.[3, 4] In the United States, preeclampsia affects ~4% of all pregnancies and is among the top causes of death during pregnancy.[4] Preeclampsia is also the leading

cause of premature birth and low birth rate, causing an additional $2.18 billion each year in US healthcare costs on top of the normal cost associated with birth.[5] Worldwide, preeclampsia affects 2-8% of all pregnancies and is a leading cause of maternal and perinatal mortality and morbidity, with 76,000 maternal and over 500,000 fetal deaths each year.[6, 7]

Preeclampsia is believed to originate during the formation of the placenta, but complications and symptoms develop much later during pregnancy. Physical effects associated with preeclampsia can be severe. In the mother, these include end-organ dysfunction, heart failure, pulmonary edema, and stroke.[3] In the fetus, low birth weight, premature birth, still birth, and a variety of perinatal complications can result.[4, 5] Currently, no diagnostic tool may detect preeclampsia during the 1st or 2nd trimesters. As a result, treatment options for preeclampsia take the form of management strategies, i.e., close monitoring of the patient to track disease progression and the administration of antihypertension medications and magnesium sulfate.[8-10]

Preeclampsia also poses long term complications for both the mother and child, but these consequences are less understood than the complications during pregnancy. Women who develop preeclampsia during pregnancy are at a heightened risk of cardiovascular disease and also are predisposed to long term hypertension, dysrhythmias, heart failure, insulin resistance, and stroke.[11] They are also more vulnerable to mental health conditions such as anxiety, depression, and posttraumatic stress.[12] The development of preeclampsia during pregnancy also influences the long term health of the offspring. Complications in offspring linked to preeclampsia include stroke, hypertension,

pulmonary arterial hypertension, coronary artery disease, congenital heart defects, chronic kidney disease, and insulin resistance.[13, 14]

Moreover, though its effects are felt worldwide, preeclampsia's toll is strongest in developing countries and among socioeconomically disadvantaged groups.[15] The World Health Organization (WHO) notes that women in developing countries are seven times more likely to develop preeclampsia than those in the developed world.[16, 17] And in developed nations like the United States, socioeconomic status impacts preeclampsia. Preeclampsia disproportionately affects low-income women and women of color.[18] When compared to Caucasian women, African American women with preeclampsia display an increased prevalence of hypertension and are known to develop more severe complications vis-à-vis their Caucasian counterparts.[19, 20]

I.1.ii Diagnosis and Treatment of Preeclampsia

The classical clinical definition for preeclampsia is keyed to the onset of hypertension and proteinuria after 20 weeks of gestation.[18, 21] However, preeclampsia can also be diagnosed without the presence of proteinuria, if accompanied with evidence of maternal acute kidney injury, liver dysfunction, neurological features, hemolysis or thrombocytopenia, and/or fetal growth restriction.[7, 22] Other symptoms that occur around the 20th week of gestation include headache, problems with vision, vomiting, pain below the ribs, shortness of breath, and sudden swelling of the face, hands or feet.[23, 24]

These symptoms first appear at advanced stages of preeclampsia, at which time the progression of the disease is inevitable. Thus, as noted, treatment options are limited

to symptom management rather than disease dissolution.[22, 25] While observing preeclamptic patients, clinicians monitor their fluids and may provide antihypertensive treatment or corticosteroids for severe hypertension.[26] In some cases, magnesium sulfate is administered to prevent preeclampsia from evolving into eclampsia, a more serious condition associated with seizures.[24] Due to the lack of understanding in the pathophysiology of preeclampsia, the only cure is delivery of the child and placenta at which point symptoms cease.[27]

I.1.iii microRNA: Epigenetic Biomarkers for Preeclampsia

The prediction of PE at an early stage is one of the most important missions in maternal-fetal medicine. An early biomarker that could identify women at risk of developing PE would allow for closer monitoring of such women and help identify candidates for participation in early intervention trials. Epigenetic biomarkers, biomolecules that influence DNA regulation and gene expression, are linked to the onset of disease.[28-30] Within maternal-fetal medicine, there is growing interest in the concept that epigenetic dysregulation during early pregnancy might lead to PE.[31-34]

miRNAs are short non-coding strands of RNA –around 22 nucleotides in length- that are involved in post-regulatory gene expression, which involves translational repression or degradation of mRNAs.[35-37] miRNAs are found in biofluids (serum, saliva, and urine, etc.) making them useful diagnostic biomarkers.[38-41] However, characteristics such as their short length, similarity in sequence, and low concentration

makes sensing miRNA difficult.[42] Notably, miRNA accounts for less than 0.01% of the total RNA with plasma concentrations of 10^3 –10^5 copies/μL.[41, 43, 44]

Recently, an increasing number of studies are identifying epigenetic biomarkers linked to the onset of preeclampsia.[34, 45, 46] One study showed that changes in miRNA biomarker concentrations, associated with the future development of preeclampsia, can be detected as early as the 11^{th} week of gestation.[32, 33, 47] A number of these biomarkers exist as short strands of ssRNA known as microRNA. This non-protein coding nucleic structure is between 19-23 nucleotides long and plays a salient role in gene expression.[30, 42, 48, 49] Specifically, miRNA's role in expression of key genes makes it a useful biomarker for a number of diseases and cancers.[35, 50-53]

While the use of miRNA as biomarkers for disease diagnosis may seem attractive, it presents many challenges for sensing and use in diagnostics.[54] The intrinsic properties of miRNA, including its length and similarity in sequence, in combination with the low concentration of miRNA in the bloodstream, make detecting it increasingly difficult.[39, 41, 55] Laboratory methods for detecting miRNA involve microarray, northern blotting, and reverse transcription-polymerase chain reaction. While each of these techniques are capable of miRNA detection, they each have limitations that impede their usage in clinical applications and point-of-care technology.[56, 57]

Consider, to start, microarray. This is a high-throughput technique capable of detecting and regulating large amounts of miRNA simultaneously for concentrations within the fM to pM range. Microarray, however, lacks both specificity and sensitivity, and it cannot provide quantitative results.[36, 55] As for northern blotting, it is a semi-

quantitative technique used for determining size and examining miRNA expression profiles within the nM to pM range. Although it exhibits good specificity, northern blotting is a low-throughput and time consuming process that lacks sensitivity.[42, 54] Finally, Quantitative RT-PCR is both highly sensitive and specific, and it is capable of providing quantitative results. Additionally, qRT-PCR is considered the gold standard for quantifying gene expression with a low limit of detection in the fM concentration.[58] But it also has significant downsides—chiefly, its high cost and its inability to identify novel miRNA.[59, 60]

I.2 Evolution of Diagnostic Technology

I.2.i Importance of Clinical Diagnostic Testing

In 2018, the United States spent $3.6 trillion on health care, a 4.6% increase from 2017.[61] While *in-vitro* diagnostics account for only about 2.3% of national healthcare expenditures, they influence approximately 60-70% of all clinical decisions and healthcare diagnoses.[62] Thus, the more IVD tests there are available, the more pronounced are treatment outcomes. What's more, along with diagnostic information, IVD allows clinicians to monitor patients and track the treatment and progression of disease.[63-65]

IVD apply advanced biochemical techniques to isolate and measure biological molecules, or biomarkers, that indicate patient health and disease. These diagnostic tests are performed using biological fluids, such as blood, urine, or saliva, which are collected from the patient.[66, 67] The biological sample is then typically sent to a centralized lab to be tested.[63] Sample analysis by way of laboratory testing is often a lengthy process

that is both costly and inconvenient.[68, 69] For this reason, clinicians are increasingly relying on an alternative form of IVD—point-of-care technology—which allows clinicians to quickly test samples on-site.[39, 70, 71]

I.2.ii Point-of-Care Technology

POCT is an alternative approach to IVD aimed at developing low cost diagnostic devices that allow for on-site testing and rapid analysis of patient samples.[72] The potential of POCT to improve healthcare is particularly meaningful for developing countries with limited access to diagnostic testing. To that end, the World Health Organization has established the "ASSURED" criteria to guide the development of POCT. The criteria are based on the perfect model of a diagnostic test for improving clinical treatment of infectious tropical diseases and sexually transmitted infections in developing countries.[73] The WHO's "ASSURED" criteria dictates that POCT must be **A**ffordable, **S**ensitive, **S**pecific, **U**ser-Friendly, **R**apid & Robust, **E**quipment-free, and **D**eliverable (i.e., **ASSURED**).[54, 74] The ASSURED criteria is often referred to when designing diagnostic tests for recently discovered biomarkers. The potential for creating new diagnostic devices at the point-of-care level is significant for conditions like preeclampsia which most often impact underserved populations and lack definitive diagnostic criteria. Since the WHO established the ASSURED guidelines for POCT over a decade ago, Land et al revised the criteria to include **R**eal-time connectivity and **E**ase of specimen collection otherwise known as **REASSURED**.[75] The REASSURED criteria for POCT is summarized in Table 1. Overall, diagnostic devices at the point-of-care level must either

Table 1 Overview of REASSURED criteria for point-of-care technology

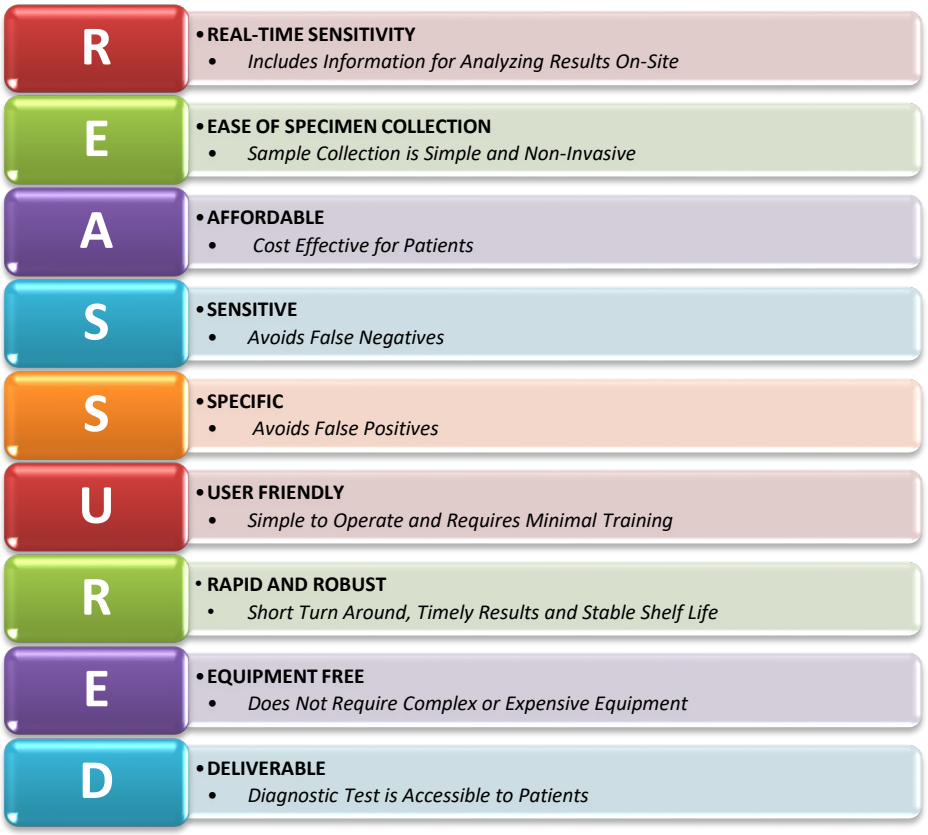

satisfy or exceed the current standard of sample analysis used by centralized labs but do so in a quicker, more efficient, and compact format.

Optical spectroscopy is a potential platform for developing POCT to diagnose preeclampsia that meets the ASSURED criteria.[67, 76] In broad strokes, optical sensing techniques are easily adaptable and can be incorporated into various diagnostic platforms.[64, 77] They also allow for the simultaneous detection of multiple analytes. More specifically, optical spectroscopy uses inherent molecular characteristics to facilitate analyte detection.[55] This makes it an adaptable sensing technique capable of low concentration molecule detection, small molecule detection, and quantitative analysis.[78]

Fluorescence and Raman spectroscopy are particular applications of optical spectroscopy that are promising POCT candidates.[69, 79, 80]

I.2.iii Paper Fluidics for Point-of-Care Testing

Paper fluidics provides a low cost vehicle for designing an optical point-of-care device. Compared to other potential platforms, paper is easily accessible, and its low cost allows it to meet the criteria defined by the WHO for POCT.[74, 81, 82] Paper can also easily be exploited to serve a number of different functions necessary for a versatile POCT tool.[83, 84] The porous structure of paper provides an abundance of surface area for biomolecular interaction and functionalization.[85] Additionally, it allows for storage of compounds and promotes fluid flow through capillary action. Other characteristics of paper that make it useful for POCT include surface characteristics, surface area, capillary flow rate, pore size, and thickness.[86, 87] These characteristics vary based on the grade of paper and are chosen based on their specific application.[88] The various grades of paper available commercially differ in their hardness, purity, chemical functionalization and reactivity. Thus, different grades of paper can be combined to create a multi-functioning device.[89, 90]

I.2.iv Lateral Flow Immunoassays for Point-of-Care

Lateral flow assays are of the one most well-known microfluidic paper-based analytical devices due to their simplicity, low cost, and quick results.[91] Currently, commercial LFAs are used in agriculture, food safety,[92] forensics, and healthcare.[84,

93, 94] This wide array of applications is due to a highly adaptable design. LFAs are 2D microfluidic devices whereby fluid flows horizontally and parallel to the paper's surface.[95] The recognition layer is found on the surface of the porous cellulose membrane and is where the biochemical capture reactions between antigen and antibody or target and probe occur. Assay recognition elements are stored within defined regions of the cellulose membrane known as the reaction or detection zones. Capillary forces govern and maintain fluid flow of the sample through the cellulose membrane.

The architecture of LFAs is comprised of four components: the sample pad, a conjugate pad, the reaction membrane, and an absorbent pad as shown in Figure 1.[96] Each component has primary function that allows for detection of the target analyte. The sample solution is deposited onto the sample pad where capillary flow of the solution is initiated. The conjugate pad contains labeled recognition elements specific to the target analyte. The sample solution flows from the sample pad onto the conjugate pad where the recognition elements are introduced into the sample solution. The resulting solution continues flowing onto the reaction membrane which contains analyte capture elements.[97] The capture elements are immobilized onto reaction membrane, which

Figure 1 Basic architectural design of a lateral flow microfluidic device

typically consists of a nitrocellulose membrane.[98] The regions at which the capture elements are immobilized are known as the control line and test line. The capture elements are either oligonucleotide probes which allow for DNA or RNA hybridization or antibodies/aptamers for analyte binding. Thus, the adaptability of LFAs results from the choice of target-specific capture analytes.[99] Finally, once the sample solution has passed the reaction membrane it is absorbed by the absorbent pad that is used to store the waste. The LFA results in colorimetric changes at the control line and test line that can easily be read by the user.[88]

Despite the numerous advantages of LFAs, their application is restricted to simple sensing applications. The primary limitations of LFAs involve difficulties in multiplexing and providing quantitative results. Cross reactivity is a primary concern in multiplexed LFAs. Compared to laboratory-based assays, LFAs also exhibit limited sensitivity especially at high analyte concentrations. At high analyte concentrations, the decrease in sensitivity and appearance in false positives is due to the hook effect.[95]

I.2.v Vertical Flow Immunoassays for Point-of-Care

In response to the limitations of LFAs, vertical flow assays were developed by stacking multiple 2D microfluidic layers resulting in a stacked membrane with both lateral and vertical flow (Figure 2). Wax printing is commonly used in creating the hydrophobic barriers for the patterned 2D layers. The flow of the solutions is directed from the top layer, through the stacked structure, to the bottom layer.[100] In regard to their application, VFAs employ some of the same basic principles of LFAs. Both platforms

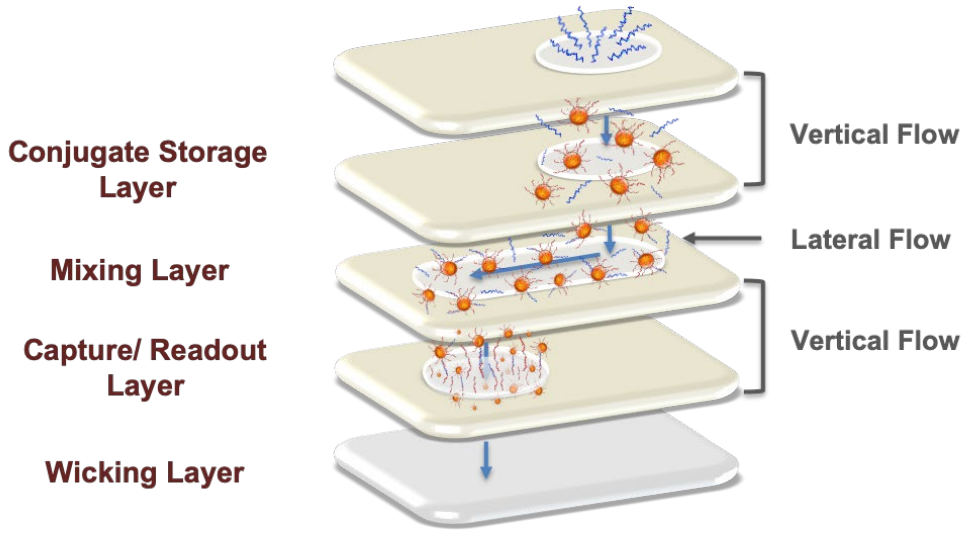

Figure 2 Overview of vertical flow design

include conjugate layers for storing labeled sensing elements and a reaction membrane containing immobilized capture elements.[95]

A major advantage of VFAs is their ability to distribute the sample solution both laterally (*x*, *y* planes) and vertically (*z* plane), which can allow for parallel multiplexed assays.[101] Taking advantage of the stackable structure of VFAs, the device can be designed to include multiple assays by adding or removing different layers. The result is a multiplex assay with minimal user involvement.[95, 102] Furthermore, changes in the design of the patterned 2D layers can be used to control the flow and function of the device.[103, 104] Compared with LFAs, VFAs also require smaller sample volumes due to the shorter path length necessary with vertical flow. A smaller path length results in an increased sensitivity by limiting the amount of sample loss during flow.[105, 106] Due to their complexity VFAs require a large amount of optimization making them highly

analyte-specific. As a result, VFAs lack a universal platform which can be adapted for different analytes.[107, 108]

I.3 Raman Spectroscopy

I.3.i Overview of Raman Spectroscopy

Raman scattering in an inherently weak phenomenon that occurs in approximately one out of every ten million incident photons. Typically, incident photons that interact with a molecule undergo elastic scattering, or Rayleigh scattering, in which the scattered photon is equivalent to the incident photon.[109] Raman scattering is a form of inelastic scattering that occurs when the optical oscillations of a photon interact with the vibrational oscillations of a molecule.[110] The resultant scattered photon will either lose energy and emit at a longer wavelength and lower frequency (Stokes Raman Scattering), or, gain energy and emit at a shorter wavelength and higher frequency (anti-Stokes Raman scattering).[111, 112] This is further shown by the Jablonksi Diagram in Figure 3. As the scattered photon undergoes a change in energy, the molecule exhibits a shift in its dipole moment. Thus, wavelength and energy of scattered photons is dependent on the vibrational state of the molecule when Raman scattering occurs. Molecules in an excited state result in anti-Stokes Raman scattering while molecules in the ground state lead to Stokes Raman scattering.[113, 114]

Raman spectroscopy is an optical technique that measures the shift in frequency/wavelength of a photon that hits a molecule and undergoes inelastic scattering.[115] The change in wavelength of the scattered photon is dependent on the

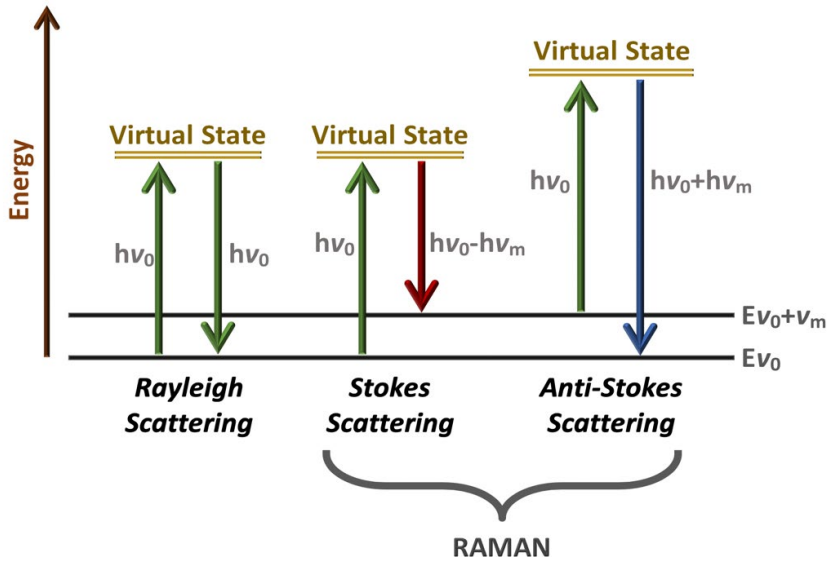

Figure 3. The Jablonski Diagram of elastic, Rayleigh Scattering, and inelastic, Raman Scattering

molecular and chemical composition of the interacting molecule. The resultant Raman spectrum is comprised of various peaks, where each peak is associated with a vibrational mode of a specific bond within the molecule. Thus, the inelastic scattering of a photon with an object results in a Raman spectrum unique to that object and is referred to as the object's "molecular fingerprint."[116, 117]

While Raman spectroscopy has sometimes been used to identify unknown compounds, its inherently weak signal along spectral overlap that is observed with complex samples limits its application in sensing technology. As a result, highly polarizable molecules, known as Raman reporter molecules, are used to produce strong Raman bands that in turn produce discernable peaks.[118] Further signal amplification is achieved from the formation of LSPs that supplement the electromagnetic fields on the surface of roughened metal substrates.[111, 119]

The process for forming plasmons requires incident light to excite the sea of electrons within a metal substrate.[120] As seen in Figure 4, the energy from the light is transferred to electrons which, as a result, begin oscillating throughout the substrate as a wave. This propagating wave of synced electrons moves from inside the metallic substrate toward the surface where energy is transferred to the electrons located at the surface causing the surface to illuminate.[121] The electrons on the surface are subjected to the same oscillating motion felt throughout the molecule, thereby providing further signal enhancement due to the additional electromagnetic field.[120] In general, a plasmonic incident only occurs at the wavelength of light at which the particle naturally resonates.[122] The resulting plasmon is therefore related to the physical characteristics of the particle. The technique for signal enhancement through amplification of electromagnetic fields is known as surface-enhanced Raman spectroscopy.[111]

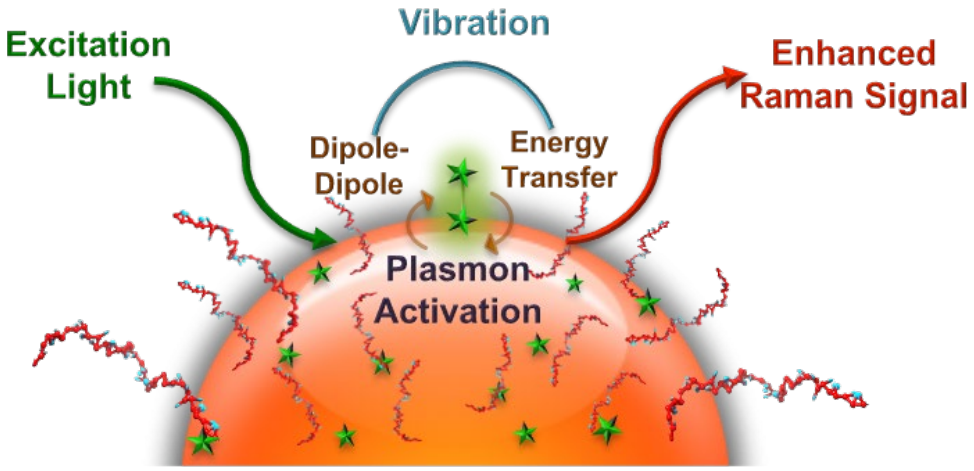

Figure 4 Graphical representation of Localized Surface Plasmon formation at the surface of a metallic nanoparticle to enhance the signal of the analyte at the surface

I.3.ii Colloidal Surface-Enhanced Raman Scattering

Compared to Raman spectroscopy, SERS is capable of sensing molecules at low concentrations due to its enhanced signal.[123] SERS relies on plasmonics and the formation of 'hotspots' to increase the likelihood of photons to undergo Raman scattering. 'Hotspots' occur when neighboring nanoparticles move close to one another, and a region of high-energy results from the polarization of the two nanoparticle surfaces, as shown in Figure 5.[117, 124] Particles located within this high-energy plasmonic 'hotspot' exhibit further signal enhancement.[80] As a result, SERS can provide enhancement factors of up to ~10^6.[80, 125]

The signal enhancement associated with SERS allows it to be useful for sensing small molecules at low concentrations.[126, 127] In sensing applications, nanoparticles are often coated with target-specific probes and highly active Raman reporter molecules

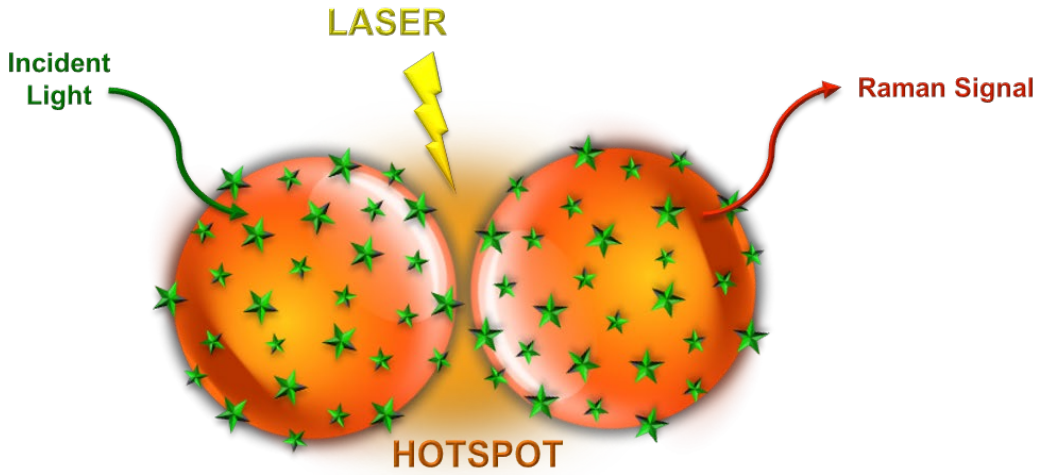

Figure 5 Graphical representation of SERS 'hotspot' formation that emerges from the close proximity of metallics

to allow for indirect analyte sensing.[128] Nanoparticle functionalization facilitates signal enhancement by controlling the formation of 'hotspots' while also providing analyte selectivity.

SERS in combination with metallic nanoparticle detection assays results in a highly adaptable optical sensing platform. In this approach, the metallic nanoparticle surfaces not only provide significant signal amplification, but also function as a substrate for conjugating highly sensitive capture elements.[129] The addition of polymers on the nanoparticle surface promotes colloid stability and extends the shelf life of the assay.[119] While polymers are absorbed by the metallic surface, capture and recognition elements are designed to include reactive sulfide (thiol) or disulfide functional ends which allow them to bind to nanoparticle surfaces through formation of SAMs.[130] The result is a highly organized monolayer. Characteristics of the assay such as the concentration of nanoparticles, the amount of capture elements immobilized on the surface, or the number of RRMs can be adjusted to achieve the necessary sensing requirements.[131] The assay's adaptability, coupled with the low limit of detection achieved through SERS, makes this overall technique appealing for biomarker detection.[132]

CHAPTER II

DEVELOPMENT OF A MIRNA SURFACE-ENHANCED RAMAN SCATTERING ASSAY USING BENCHTOP AND HANDHELD RAMAN SYSTEMS*

II.1 Introduction to Raman Spectroscopy for microRNA Detection

Historically, Raman spectroscopy required the use of large, bulky, and expensive benchtop microscope systems.[133] Thus, taking advantage of SERS' capabilities in clinical applications requires overcoming the shortcomings associated with these traditional systems along with improving assay reproducibility.[126, 134] Recent developments of handheld and portable Raman devices may facilitate quick and easy on-site medical testing.[135] However, the results observed using compact Raman spectrometers are often of lower quality compared with the Raman spectra obtained using most benchtop systems. This is due, in part, to compact spectrometers' low-power laser diode sources and lower resolution (but more cost effective) optical components. Though early systems used NIR wavelengths, systems using shorter, higher energy wavelengths are now available. However, these new systems are typically more expensive or bulky because they require high power sources. Conversely, NIR laser diodes produce lower energy excitation, thus often sacrificing sensitivity, but they require less energy and can be battery operated. In particular, NIR excitation sources are commonly used with biological samples due to their longer sample penetration depths. Further, the longer

* Reprinted with permission from "Transitioning from benchtop to point-of-care for early detection of Preeclampsia using microRNA," by Schechinger, M, et al., 2018, Journal of Biomedical Optics, 23(1), 017002(2018). doi: 10.1117/1.JBO.23.1.017002, Copyright 2020 by SPIE.

wavelengths of NIR sources produce less background noise from autofluorescence of biological samples when compared with shorter wavelength lasers.[127] In contrast, lasers at shorter wavelengths such as 532 nm produce higher energy Raman scattering, which typically provides a clearer SERS signal when used with most common reporter dyes. However, prolonged exposure of a sample to high-energy (i.e., shorter) wavelengths can result in sample evaporation and photochemical degradation, in addition to stronger autofluorescence from tissue. Therefore, optimizing enhancement factors that create a strong and consistent Raman signal is key to compensating for the lower optical resolution associated with portable and handheld Raman systems.

II.1.i Comparison of Sensing Factors for Raman Spectroscopy

The influence of excitation wavelength on the miRNA-17 SERS assay signal was initially investigated. Lasers with excitation wavelengths at 532 and 785 nm were chosen to compare signal enhancement from DNA-coated silver nanoparticles conjugated with Raman reporter molecules. Silver nanoparticles were chosen due to their ability to provide surface oxidation and enhanced Raman scattering.[136] Additionally, the larger extinction coefficient of silver nanoparticles when compared with gold nanoparticles provides larger SERS enhancements. In parallel, the comparative intensity of the assay's SERS signal using different types of photoactive Raman reporter molecules was assessed. Highly polarizable small molecules such as 4-mercaptobenzoic acid,[137] DTNB,[138] and 4-mercaptopyridine[139] are commonly used as reporter dyes since they provide simple, distinct, and readily recognizable Raman spectra. Fluorophores are among the most

common dye molecules used in sensing and are often used in Raman spectroscopy because they are widely available. However, their overwhelming emissions can sometimes interfere with the Raman signal and cause a large degree of background signal when not properly quenched.[69] Finally, the use of synthetic non-fluorescent dyes—most often those with triphenylmethane backbones such as crystal violet, Victoria blue, and malachite green—has become increasingly popular since it avoids fluorescence emission and offers absorbance overlap with common Raman excitation laser lines. For our study, three types of molecules commonly used as Raman reporters were investigated, namely: (1) a chromophore, MGITC, with absorption maxima at 620 nm, (2) a fluorophore, TRITC, with absorption maxima at 550 nm, and (3) a Raman active molecule, DTNB, with an absorption maxima at 402 nm.[140, 141] As a fluorophore, TRITC also features a characteristic emission wavelength at 576 nm (Figure 6(a)).[142]

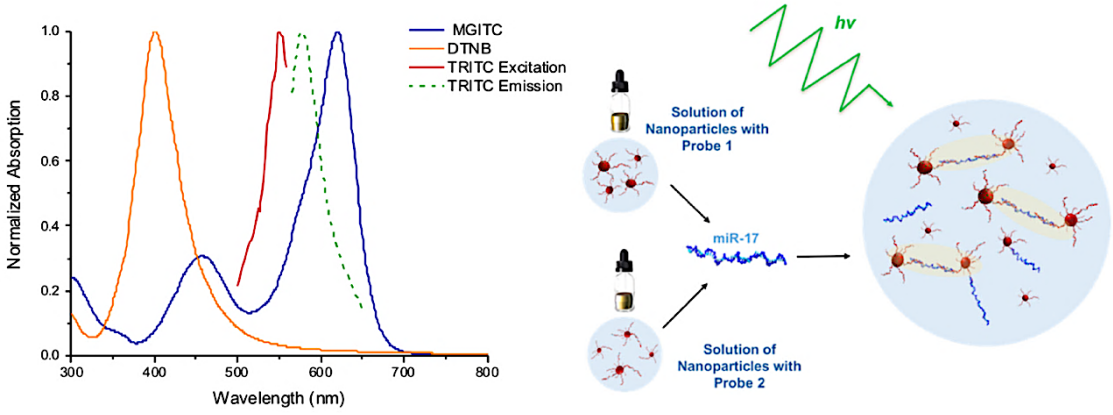

(a) (b)

Figure 6 (a) Comparison of absorption spectra of the three Raman reporter molecules (MGITC, DTNB, and TRITC) and the fluorescent excitation and emission spectra for the fluorophore, TRITC; (b) a graphic representation of the assay

After comparing the non-fluorescent chromophore, Raman active molecule, and fluorophore, the molecules that showed adequate signal enhancement with the benchtop system were then examined using a handheld Raman device with an excitation laser at 785 nm.

This study used a "turn on" sandwich nanoparticle assay developed for detecting nanomolar levels of microRNA-17 using SERS (Figure 6(b)).[143] Silver nanoparticles were functionalized by immobilizing modified oligonucleotide strands at the surface of the nanoparticle. Two independent thiol-modified strands of PEGylated oligonucleotide were designed, with each strand complementary to half of the target miRNA (Figure 7).[144, 145] Probe 1 was designed to bind to the 5′ end of the target, whereas probe 2 was constructed to bind to the second half of the target at the 3′ end, with a HEG spacer between the end of the DNA probe and the thiol modification.[146-148] Nanoparticles were functionalized entirely with either probe 1 or probe 2, and then mixed at a 1:1 volume ratio. If miRNA-17 is present, the target strand is oriented in between two nanoparticles and hybridization to the target draws the nanoparticles close to one another, allowing plasmons to couple and form an area of high-energy known as a "hotspot." [118, 149, 150]

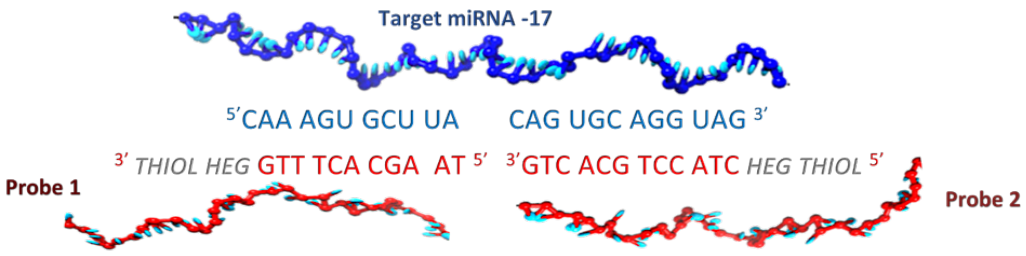

Figure 7 Schematic of two modified DNA probes selected for hybridization to the target analyte miRNA-17.

The high affinity of the nanoparticle probes with the target analyte causes a nanoparticle to simultaneously bind with multiple targets, creating an aggregate or matrix of interconnected units of nanoparticles bound with miRNA. This sandwich-type assay is common among detection assays in which an enhancement in the SERS signal is observed when the target is present.[130, 151]

II.2 Designing a Sensing Assay for miRNA-17

Benchtop Raman spectra were obtained using a 10X ThermoScientific DXR Raman confocal microscope (Thermo Fisher Scientific; Waltham, Massachusetts) with 900 and 830 g/mm gratings for excitation lasers with wavelengths of 532 and 785 nm, respectively. To capture the spectra, a thermoelectrically cooled charged-coupled device (CCD) camera was used in combination with the Raman microscope. Additional handheld Raman spectra were collected using the IDRaman mini 2.0 system (Ocean Optics; Florida). Table 2 shows a summary of the defined optical parameters used for each Raman system as well as a brief overview of their sensing capabilities.[152-155]

The nanoparticles were characterized using a Zetasizer Nano ZS90 (Malvern, United Kingdom) as well as a transmission electron microscope (TEM) (FEI Company;

Table 2 Summary of optical specifications of the Raman system tested (benchtop and handheld)

	EXCITATION WAVELENGTH	RAMAN SHIFT	SPECTRAL RESOLUTION	POWER AT SOURCE	POWER AT SAMPLE	SPOT SIZE	INTEGRATION TIME
BENCHTOP							
THERMO SCIENTIFIC							
DXR RAMAN	532 780	50-1800 cm^{-1}	2 cm^{-1}	24 mW 80 mW	10 mW 24 mW	10 µm	1.0 s
HANDHELD							
OCEAN OPTICS							
IDRAMAN MINI	785	400-2300 cm^{-1}	18-20 cm^{-1}	100 mW	50 mW	2.5 mm	100 ms

Hillsboro, Oregon) to determine their surface charge (zeta potential) and diameter. The absorption characteristics of the nanoparticles were determined using an Infinite® 200 Pro multimode micro-plate reader (Tecan, Switzerland).

The target miRNA-17 oligonucleotide (sequence: 5′CAA AGU GCU UAC AGU GCA GGU AG3′) was synthesized by Integrated DNA Technologies (IDT). The two half-compliment strands of modified ssDNA were designed: sensing probe 1 (sequence: $^{5'}$THIOL HEG CTA CCT GCA CTG$^{3'}$) and sensing probe 2 (sequence: $^{5'}$TAA GCA CTT TG HEG THIOL$^{3'}$). The probes were designed based on the sequence of the target miRNA-17 oligonucleotide (sequence: $^{5'}$CAA AGU GCU UAC AGU GCA GGU AG$^{3'}$) (Figure 7). Hydroxylamine silver nanoparticles were synthesized using an adaptation of the rapid, room temperature synthesis method developed by Leopold and Lendl.[136] The concentration of each sample was calculated using Beer– Lambert's Law.

The modified oligonucleotide probes were purchased in a disulfide form and were subsequently reduced to contain thiol "sticky-ends" and washed before being immobilized onto the nanoparticle surface. To ensure a consistent degree of surface functionalization, the molar ratio of immobilized oligonucleotides added per nanoparticle was set at 1000:1 and the calculated volume of oligonucleotides [24.6 μL of probe 1 (34.9 μM); 41.8 μL of probe 2 (20.6 μM)] was added to one of two samples containing 1 mL of nanoparticles. Each sample contained nanoparticles functionalized entirely with either probe 1 or probe 2. The samples were stored separately at room temperature to ensure that neither sample contained a combination of the two probes. Following the addition of the oligonucleotides, the samples were left to react overnight on a shaker table (VWR mixer vortex). After

shaking, 60 μL of 250 μM citrate HCl solution (pH 3.0) was added to each sample to expedite the reaction,[156] and the samples reacted for an additional 20 min while shaking. Next, each sample of now functionalized silver nanoparticles was centrifuged for 20 min at 3.3 rcf to wash away any unconjugated oligonucleotides. For both samples, the resultant supernatant was removed and discarded without disturbing the pellet at the bottom of the tube. Pellets were then resuspended in PBS buffer (0.1 M, pH 7.4).

Following nanoparticle functionalization with either probe 1 or probe 2, the solution of nanoparticles conjugated with probe 1 was labeled using one of the three different types of Raman reporter dyes (MGITC—sample a, DTNB—sample b, and TRITC—sample c). Only nanoparticles functionalized with probe 1 were labeled. No dye was added to nanoparticles functionalized with probe 2. Using the stock concentration of each dye, the amount of dye was calculated to achieve an ideal ratio of 1000 dye molecules per one nanoparticle. This calculated volume [85.9 μL of dye (10 μM)] was then added to samples containing 1 mL of nanoparticles functionalized with probe 1. The samples were then shaken for 1 h before being left overnight at room temperature. Samples were washed by centrifuging the solution of nanoparticles for 20 min at 7000 rpm to remove any excess unconjugated dye. The resultant supernatant was discarded, and the nanoparticle pellets were resuspended in PBS buffer at a pH of 7.4.

II.2.i Assay Analysis Using a Laboratory Benchtop Raman Microscopy

The different variations of the assay (sample assay a with MGITC; sample assay b with DTNB; and sample assay c with TRITC) were loaded separately into a black Greiner

384-well plate and examined using the confocal benchtop Raman microscope. The wells were filled to their maxima volumes of 30 µL. Equal volumes of nanoparticles conjugated with probe 1 and probe 2 were added to each well. The remaining 10 µL volume was composed of either PBS or 1 nM target miRNA-17 suspended in PBS. Wells without miRNA-17 were designated as control samples and used to compare the sensitivity for each embodiment of the assay. Target miRNA-17 was suspended in PBS at a concentration of 1 nM. This concentration remained constant among all experimental samples. A pipette was used to mix the resultant solution of nanoparticles thereby allowing the target to be dispersed throughout the nanoparticle detection assay. Prior tests showed that for 30 µL of sample, the SERS intensity gradually increased until it reached steady maxima intensity after 1 h. Therefore, the sample were placed in the measurement plate and set aside for 1 h to allow for optimal aggregate formation. Subsequent SERS analysis was performed using a Thermo Scientific DXR Raman Microscope at excitation wavelengths of 532 and 785 nm (Figure 8).

The nanoparticle assay was tested further to determine its specificity for miRNA-17 and to identify any possible changes in the baseline signal due to the addition of a non-complementary target strand. The non-complementary strand used was miRNA-34a-3p (Sequence: $^{5'}$CAA UCA GCA AGU AUA CUG CCU$^{3'}$). Once again, two separate samples solution of nanoparticles were created containing either the nanoparticle assay in PBS or the nanoparticle assay combined with 10 µL of a 1 nM solution of miRNA-17. Additionally, a third sample was created by mixing 20 µL of the nanoparticle assay (10 µL of probe 1 solution of nanoparticles and 10 µL of probe 2 solution of nanoparticles)

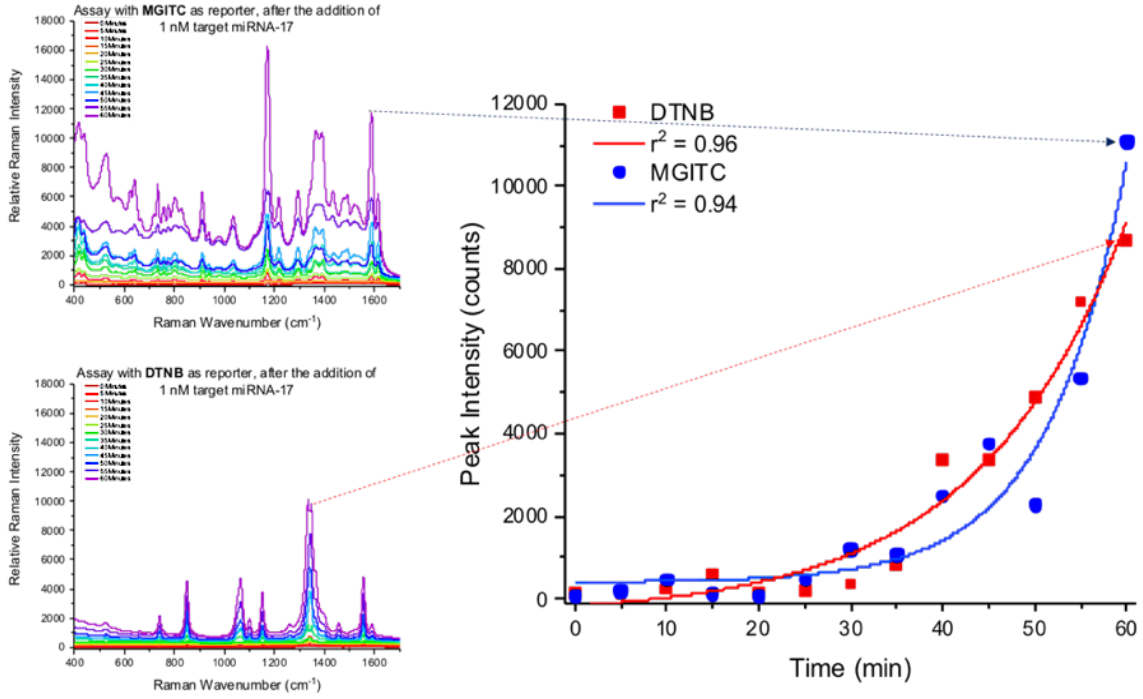

Figure 8 The change in relative Raman intensity with respect to time after the addition of 1 nM target miRNA-17

with 10 µL of a 1 nM solution of miRNA-34a-3p in PBS. Once synthesized, all three samples were left to react for 1 h. Using an excitation laser at 532 nm, the Raman signal for each of the samples was then observed with the benchtop Raman microscope.

II.2.ii Assay Analysis Using a Handheld Raman System

The various sample assays were loaded into 2 mL glass scintillation vials for analysis using a handheld device. A sample volume of 600 µL was used for each vial, with each containing: 200 µL of silver nanoparticles functionalized with a Raman reporter and probe 1, 200 µL of silver nanoparticles with probe 2, and 200 µL of either PBS or target suspended in PBS. The concentration of the miRNA-17 in PBS was 1 nM—the same

molar ratio used with the benchtop Raman system. Similarly, the subsequent reaction time necessary for maxima SERS intensity was also denoted as 1 h. These assays were analyzed using the IDRaman mini handheld Raman system by Ocean Optics. The sample vials were loaded directly into a specially designed chamber, which used an excitation laser at 785 nm. The IDRaman mini used the maxima laser power at level 5 (100 mW at the source and 50 mW at the sample),[154, 155] with an exposure time of 100 ms.

II.3 Results and Discussion

II.3.i Characterization Data

TEM images showed that the diameter of the synthesized silver nanoparticles was 29 nm (SDEV ± 2 nm) (Figure 9(a)). Experimentally, this diameter was confirmed via UV–Vis spectroscopy measurements. The maximum absorbance intensity was located at a peak wavelength of 405 nm (Figure 9(b)), which corresponds to ~30 nm and an extinction coefficient of (1.45×10^{10} M^{-1} cm^{-1}). Based on the values for extinction coefficient and absorbance maximum at 405 nm, the silver nanoparticle concentration was calculated using Equation 1 as 81.6 nM.

$$Abs = c\varepsilon_{\lambda}l \qquad \text{Equation 1}$$

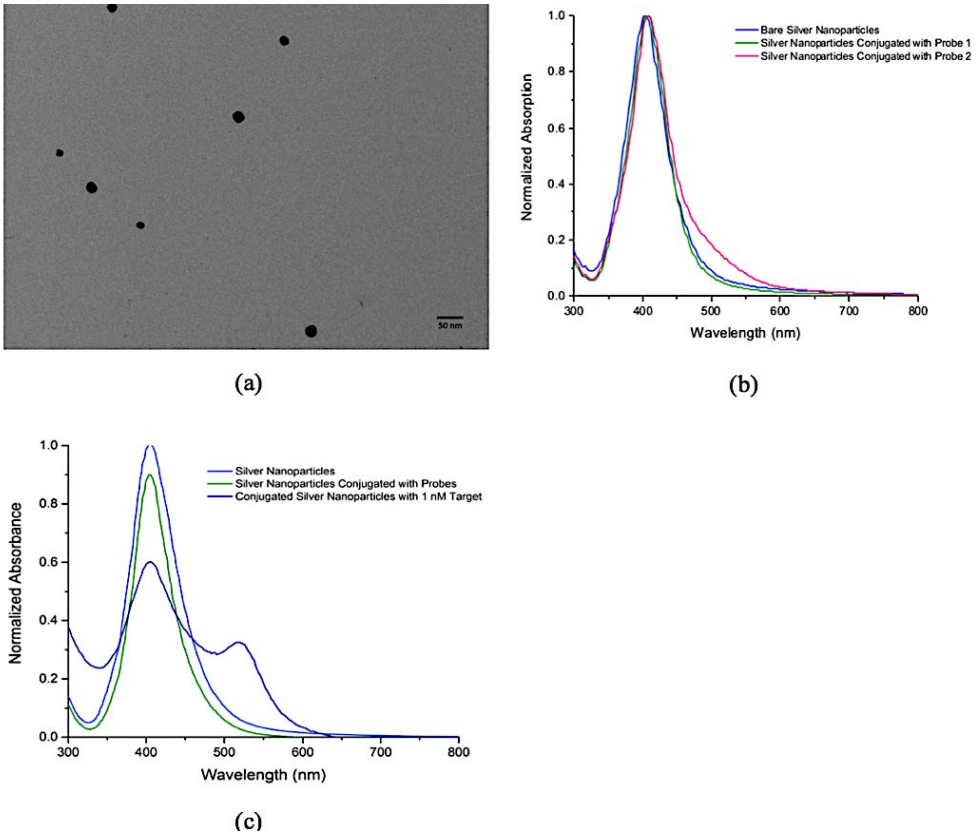

Figure 9 (a) TEM images of silver nanoparticles; (b) absorption spectra of silver nanoparticles conjugated with probe 1 and probe 2; and (c) the extinction spectra for bare unconjugated silver nanoparticles, a combined solution of silver nanoparticle conjugated with either probe 1 or probe 2, and an aggregated combined solution resulting from the addition of the target analyte, miRNA-17

The solutions of silver nanoparticles were used to synthesize individual stock solutions of nanoparticles conjugated with probe 1 and nanoparticles with probe 2. Following conjugation, the absorption spectra were collected for both stock solution of nanoparticles and used to confirm successful nanoparticle conjugation with probes (Figure 9(b)). In both cases, the absorption maximum increased by 2 nm indicating successful conjugation of the nanoparticles with probe. The absorption spectra were also used to verify colloid stability and the lack of aggregate formation. No change in nanoparticle size

was concluded based on the minimal shift in the absorption maximum associated with conjugation. Furthermore, the nonexistence of secondary peaks confirms the absence of aggregates that cause a shift in the absorption maximum toward higher wavelengths and the emergence of secondary peaks.

The assay was also tested to determine its capability to form aggregates in the presence of miRNA-17. The formation of aggregates is the underlying factor, which provides an increase in relative Raman intensity when the target is present, as it facilitates plasmonic coupling. The absorption spectra of unconjugated silver colloid and DNA-functionalized silver nanoparticles were obtained, as was a combined assay solution of nanoparticles of functionalized nanoparticles assembled with miRNA-17 (Figure 9(c)). The samples of plain and functionalized nanoparticles produced a single peak at ~405 nm corresponding to its LSPR. The combined assay with miRNA-17 provided absorption spectra with two LSPR peaks, one at ~405 nm representing the unbound probe nanoparticles and a second at ~520 nm indicating the plasmonic coupling that occurs when particles are brought in close proximity with one another by the target miRNA.

II.3.ii Comparison of Different Raman Reporter Molecules Using a Benchtop Raman System

The benchtop Raman system was first used to investigate the role of excitation wavelength in SERS signal enhancement (Figure 10). A diode-pumped, solid-state green laser, which produces an excitation wavelength in the visible spectrum (532 nm), was first

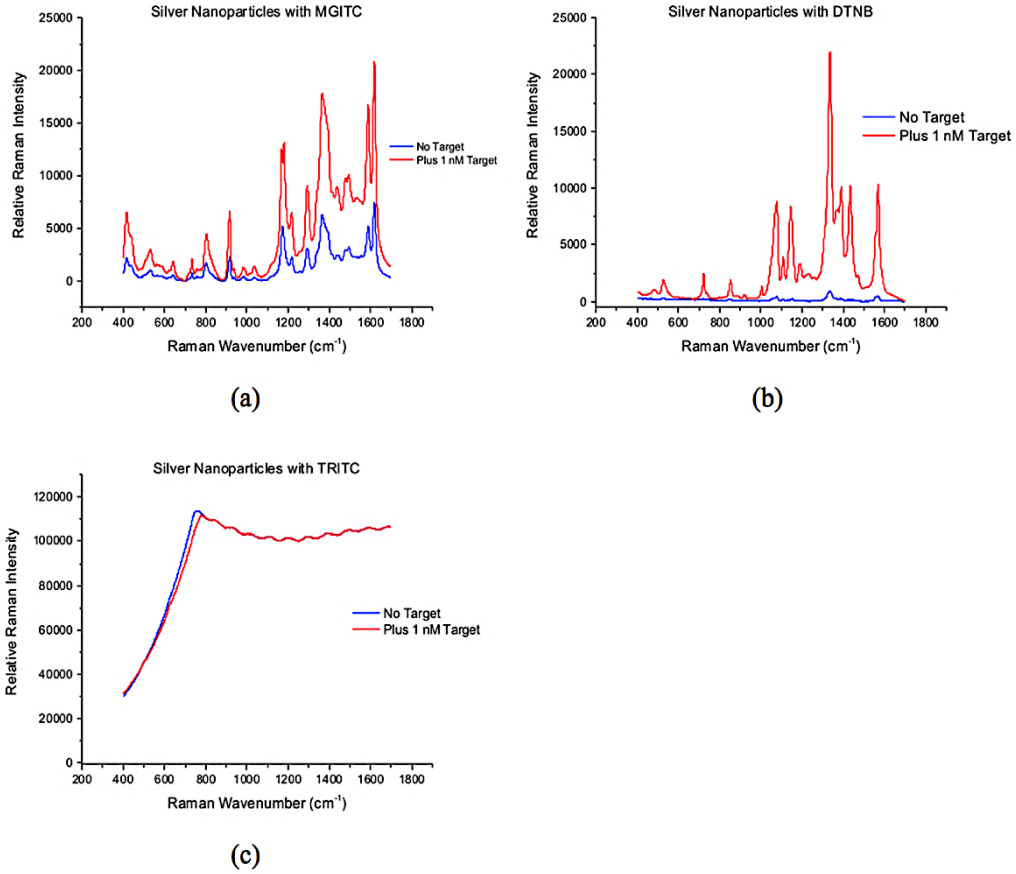

Figure 10 The average Raman spectra obtained using an excitation wavelength of 532 nm from various combinations of silver nanoparticles and photoactive dyes including: (a) MGITC, a chromophore; (b) DTNB, a Raman active molecule; and (c) TRITC, a fluorophore

used in combination with the benchtop Raman system to examine the SERS spectra for the three Raman reporter molecules using the miRNA-17 assay developed.

The SERS signal was significantly different for the three Raman reporter molecules when excited using the same laser source. For the 532 nm excitation wavelength, the assay containing DTNB produced a slightly higher maxima signal after the addition of 1 nM target miRNA-17 compared with the assay containing MGITC, thus

indicating increased sensitivity for DTNB. With respect to the TRITC reporter assay, employing a 532 nm laser (Figure 10(c)) caused the highest relative signal intensity of all reporter molecules and saturated the CCD—even at the lowest laser power setting (0.1 mW). The signal using a 532 nm laser was overwhelmingly strong due to the broad fluorescent emission of TRITC centered at 576 nm.

The excitation laser was then replaced with a red frequency-stabilized single mode diode laser, which produced an excitation wavelength in the NIR, at 785 nm. The SERS signal was once again collected for each Raman reporter molecule using the assay specific to miRNA-17 (Figure 11). The use of an NIR excitation laser at 785 nm produced Raman spectra similar to those obtained using the 523 nm laser. The three assays containing the same concentration of DNA-functionalized silver nanoparticles tagged with the three different Raman reporter dyes were then compared (Figure 11). This time, silver nanoparticles labeled with MGITC produced the highest Raman intensity when 1 nM of the target miRNA-17 was present. In the presence of the target, the MGITC assay demonstrated an observable increase in the relative Raman intensity. Silver nanoparticles labeled with DTNB still produced signal enhancement both with and without the presence of the target, as was the case with the visible 532 nm source. In the presence of the target, both assays containing MGITC and DTNB showed an observable increase in the relative Raman intensity, though the sensitivity of the MGITC assay was significantly higher. No enhancement was observed for silver nanoparticles labeled with TRITC before the addition of the target miRNA. The spectrum associated with TRITC was visible only after the addition of the target.

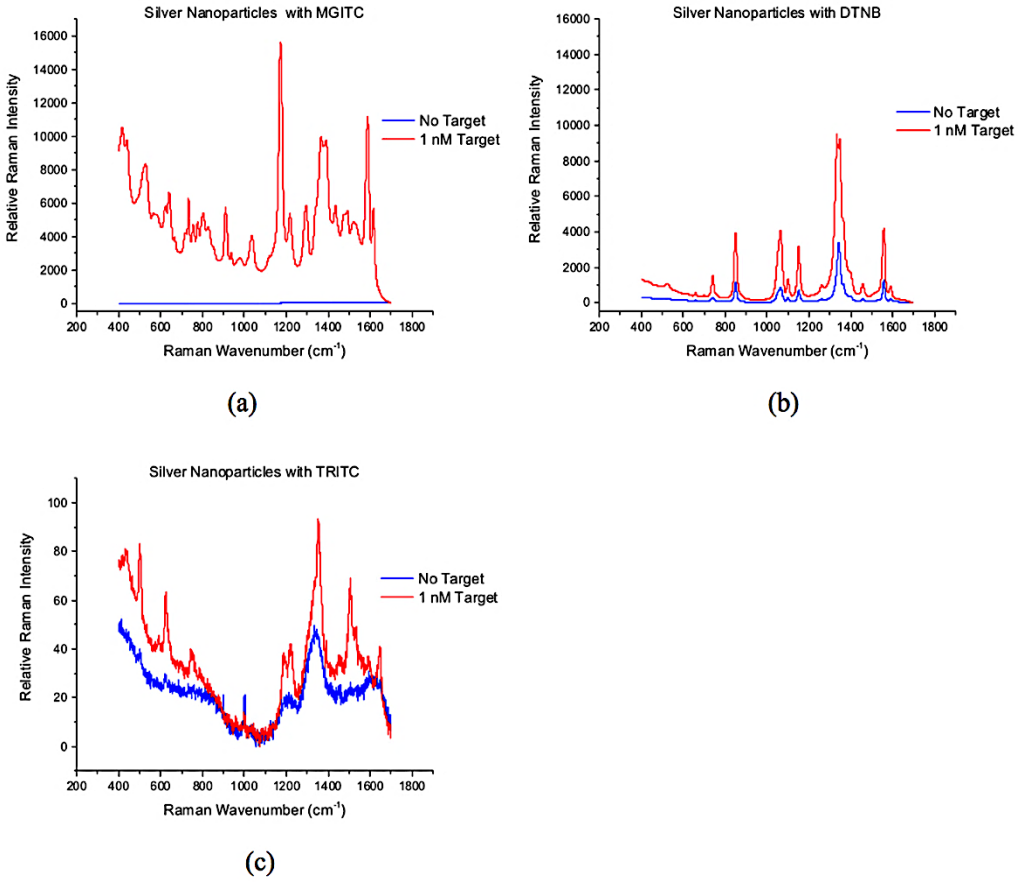

Figure 11 The average Raman spectra obtained using an excitation wavelength of 785 nm from various combinations of silver nanoparticles and photoactive dyes including: (a) MGITC, a chromophore; (b) DTNB, a Raman active molecule; and (c) TRITC, a fluorophore

A quick comparison of the SERS spectra collected using the laser at 532 and 785 nm revealed that MGITC and DTNB were effective in sensing for miRNA-17 for both excitation wavelengths. The use of TRITC as a Raman reporter molecule proved ineffective at both wavelengths due to its inability to provide a discernable signal in the presence of miRNA-17. While MGITC and DTNB were effective at both excitation wavelengths, a noticeable increase in the overall signal intensity was visible when the 532

nm laser was used. The maxima signals observed for both MGITC (Figure 10(a)) and DTNB (Figure 10(b)) were almost 10,000 counts greater than those observed using an excitation wavelength of 785 nm (Figure 11). This significant rise in signal indicates the formation of more resonant plasmons within the assay when near the excitation wavelength of 532 nm.

The formation of aggregates occurred because DNA-miRNA hybridization facilitated SERS by combining neighboring plasmons to produce high-energy "hot spots," which caused a resultant red-shift in the LSPR.[130, 144, 157] With the visible (532 nm) source benchtop system, the jump in SERS intensity observed using DTNB yielded the greatest sensitivity. Conversely, the jump in SERS intensity observed using DTNB with the NIR benchtop system was less significant compared with that of the control. Instead, MGITC was the most dramatic and distinguishable, thus denoting MGITC as a seemingly favorable option when using 785 nm laser. These results imply that if the excitation wavelength is increased (red shifted), the Raman reporter molecule should be selected such that its absorbance also undergoes a redshift to avoid losses in the sensitivity of the overall assay system.

The spectra collected were further analyzed by examining the maxima relative Raman intensity using characteristic peaks specific to each Raman reporter. The SERS peak at 1586 cm^{-1}, assigned to the stretching and bending of an in-plane ring,[158] was chosen for evaluating the assay labeled with MGITC. The strong peak at 1343 cm^{-1}, which corresponds to the symmetric N–O stretching of the nitro group,[159-161] was used to analyze the nanoparticle assay labeled with DTNB. The assay constructed using

nanoparticles labeled with the fluorescent molecule did not produce observable Raman spectra inherent to TRITC. It was thus eliminated from further analysis since the lack of discernable spectra made it difficult to assign a characteristic peak for additional examination. The maxima relative Raman intensity shown in Figure 12(a) was defined by Raman intensity observed, whereas Figure 12(b) shows the relative Raman intensity at 1586 and 1343 cm^{-1} for the two useful Raman reporter molecules, MGITC and DTNB. The values seen in Figure 12 correspond to the average of five spectra with error bars of one standard deviation. Meanwhile, each spectrum used is the average of 10 consecutive 1 s scans.

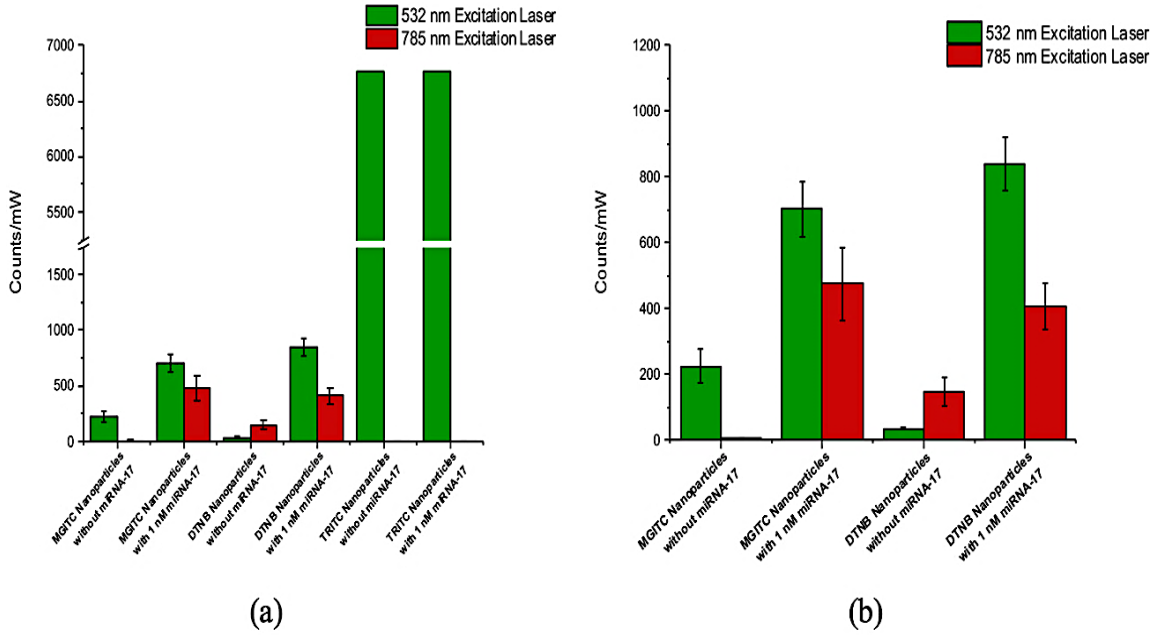

Figure 12 Graphical representation of the relative Raman intensity examined at characteristic Raman peaks, normalized for the laser power and ω^4 dependence of Raman scattering for (a) Raman reporter molecules (MGITC—peak at 1586 cm^{-1}, DTNB—peak at 1343 cm^{-1}, and TRITC) using both 532 and 785 nm excitation wavelengths and (b) an adjusted graph for MGITC and DTNB

The 532 nm laser resulted in the greatest signal enhancement for all three dyes (Figure 12). MGITC provided signal enhancement for spectra taken both with and without 1 nM of target miRNA-17 but produced higher enhancement with the target. The addition of miRNA-17 caused an increase in signal approximately equal to 3.5 times the initial signal intensity observed without miRNA-17 (Figure 12(b)). Signal enhancement was much greater in the presence of target using the assay labeled with DTNB for 532 nm. In the case of DTNB, the change in signal was over 16-fold. Unlike MGITC, DTNB produced relatively minor signal enhancement when the target was not present due to the lack of resonate localized surface plasmons. In turn, this resulted in a baseline spectrum at low relative Raman intensities. When combined with the 785 nm laser, silver nanoparticles labeled with MGITC produced the most drastic increase in intensity as compared with nanoparticles labeled with DTNB, which produced the greatest change in intensity when used with the 532 nm laser.

The difference in relative Raman intensity for the assay with DTNB at 532 nm excitation and the assay with MGITC at 785 nm excitation indicates a potential to sense precise target concentrations. To achieve the greatest signal enhancement, researchers typically choose a dye with an excitation wavelength that almost directly corresponds to the excitation wavelength of the incident laser.[162] Our results indicate that signal enhancement can also be achieved at incident wavelengths beyond those that directly correspond to the dye's excitation wavelength. The data collected showed that if the laser's excitation wavelength was in the vicinity of the dye's excitation wavelength, signal enhancement still occurred. Namely, the DTNB assay (absorption maxima of 402 nm)

functioned properly for the 532 nm excitation, and the MGITC assay (absorption maxima of 620 nm) performed better at 785 nm. However, the TRITC (absorption maxima of 550 nm) assay functioned poorly at 785 nm and was saturated at 532 nm.

II.3.iii Evaluation of Assay Specificity

A non-complementary strand of miRNA, miRNA-34a-3p, was used as a negative control to test the specificity of the assay for defined target analyte, miRNA-17, and its effect on the baseline signal (Figure 13). The solution of the combined nanoparticle assay

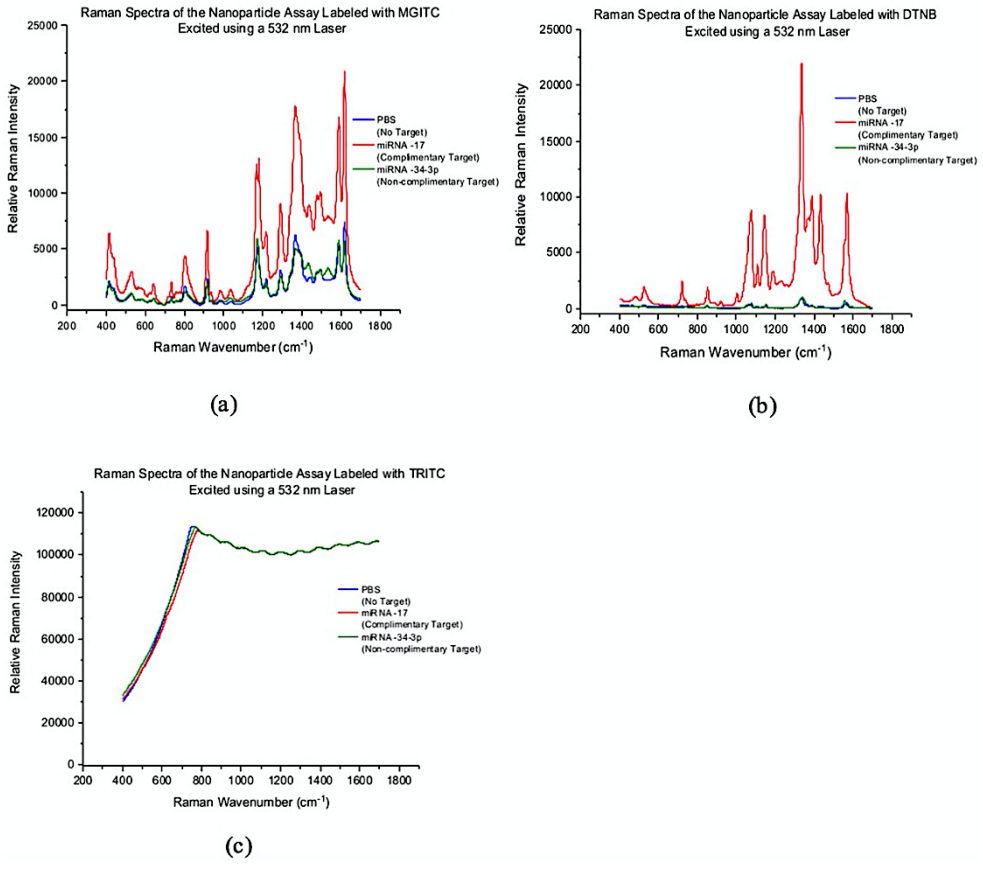

Figure 13 Raman spectral data of the specificity of the assay when labeled with (a) MGITC, (b) DTNB, or (c) TRITC and excited using a 532 nm laser

and non-complementary analyte was tested with all three Raman reporter molecules using an excitation laser of 532 nm. The graph shows that the resultant signal from the combination of the nanoparticle assay with miRNA34a-3p closely resembles that of the assay in PBS. Specifically, the maximum signal intensity of both the assay in PBS and the assay with miRNA34a-3p is about equal. Data also show that the addition of the non-complementary analyte did not alter the baseline signal.

II.3.iv Comparison of Different Raman Reporter Molecules Using a Handheld Raman System

Based on the results obtained using the benchtop Raman system, assays containing MGITC and DTNB were chosen for additional analysis in conjunction with the handheld Raman system. The volume of the sample needed for analysis was raised to 600 μL to ensure sufficient volume was present within the 15 mm glass vial, but the relative concentrations of assay components remained constant. Spectra were obtained using the handheld IDRaman mini for both the MGITC (Figure 14(a)) and DTNB (Figure 14(b)) dyes. Unlike the benchtop results, DTNB produced the strongest overall intensity signal for the IDRaman mini 2.0, with MGITC producing a significantly lower signal and exhibiting a higher noise floor. These results underscore the optical differences between the handheld and benchtop systems, implying that one cannot directly translate SERS systems from benchtop to handheld devices based solely on wavelength. Variations in the SERS response of the same two assays due to small differences in the filters, gratings, integration area, power, and source—along with the 10-fold change in resolution—are

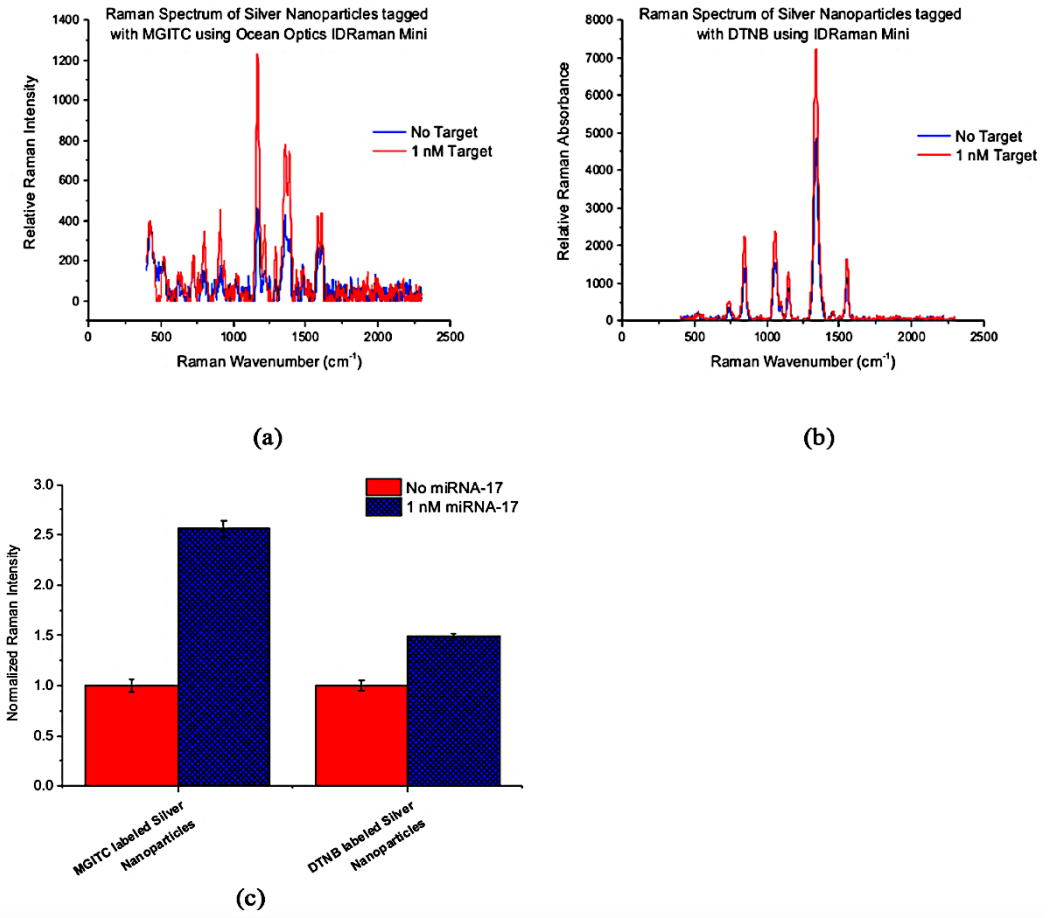

Figure 14 Raman spectra for silver nanoparticles labeled with (a) MGITC and (b) DTNB in the presence of 1 nM target obtained using the handheld IDRaman mini; (c) comparison of normalized Raman intensity for MGITC (SERS Peak at 1586 cm^{-1}) and DTNB (SERS peak at 1343 cm^{-1})

significant enough to warrant changing the Raman reporter molecule entirely. Thus, using the same characteristic peaks as previously defined for MGITC (1586 cm^{-1}) and DTNB (1343 cm^{-1}), the maxima relative Raman intensity was determined and then normalized for further analysis. The normalized plot in Figure 14(c) indicates that the assay labeled with MGITC showed the largest sensitivity, just as observed with the benchtop system for the NIR wavelength. Notably, there was a dramatic decrease in the sensitivity of the

DTNB SERS signal with the assay when transitioning from the benchtop to handheld system due to the stronger signal with no target.

II.4 Summary

For both the benchtop and handheld Raman systems, nanoparticles, when combined with hybridized miRNA-DNA, provided pronounced SERS spectra when using MGITC and DTNB photoactive Raman molecules with 532 and 785 nm excitation lasers. Comparison with the benchtop assays synthesized with different Raman reporter molecules indicated that for the designed assay DTNB, with the addition of 1 nM of target, was the highest performing Raman reporter molecule when combined with a 785 nm excitation laser, which is most often used in miniaturized Raman systems. Laser excitation wavelength heavily affected signal enhancement, which was smaller between target and no target when transitioning from the benchtop Raman system to the handheld Raman device. Additional data analysis indicated that signal enhancement is possible when using excitation lasers that do not directly coincide with the optical properties of the Raman reporter molecule. Nevertheless, enhancement is typically increased when excitation lasers most closely match the absorption maxima. Our results suggest that an understanding of plasmonics and the excitation and emission properties of assay components is necessary to facilitate the use of handheld Raman POC systems to advance clinical disease diagnosis in applications such as microRNA biomarker detection for early detection of preeclampsia.

CHAPTER III

A SERS APPROACH FOR RAPID DETECTION OF MICRORNA-17 IN THE PICOMOLAR RANGE*

III.1 Introduction to SERS for Point-of-Care

Traditional research techniques for isolating and examining miRNA from biological samples that are not suitable for the point-of-care use microarray, northern blotting, and RT-PCR.[35] In practice, both microarray and northern blotting profiling techniques are used for samples with miRNA concentrations within the nM to pM range. RT-PCR has a lower detection limit and is used to profile miRNA at fM concentrations.[42]

Chemical assays are particularly attractive for sensing applications because they provide high-precision analytical results when combined with sensitive spectroscopic techniques like Raman spectroscopy.[126] The use of miRNA for early disease detection, particularly for preeclampsia, is lacking, but SERS is potentially capable of overcoming difficulties with isolating and detecting miRNA at low concentrations.

* Reprinted with permission from "A SERS Approach for Rapid Detection of microRNA-17 in the Picomolar Range," by Schechinger, M, et al., Analyst, 144(13), 2019, United Kingdom of Great Britain and Northern Ireland. Copyright 2020 by Royal Society of Chemistry.

III.2 Experimental

III.2.i Instrumentation

A Zetasizer Nano ZS90 (Malvern, UK) was used to determine nanoparticle size and zeta potential. The nanoparticle size was confirmed using a TEM (FEI). Additionally, the function of the nanoparticle detection assay, with respect to aggregate formation due to the addition of miRNA-17, was examined using TEM images of the assay combined with target miRNA-17. The relative concentrations of the nanoparticles, probes, target, and relevant combinations were calculated using Beer-Lambert's Law based on known extinction values and the absorbance values (Figure S1) collected with an Infinite® 200 Pro multimode microplate reader (Tecan, Switzerland). The SERS signal was observed using a ThermoScientific DXR Raman confocal microscope (10x NA, 900 g/mm grating, 532 nm Excitation Wavelength, 10 mW). The SERS spectra resulted from the average of 5 spectra with each spectrum consisting of the average of 10 consecutive 1 s scans.[163]

III.2.ii Silver Nanoparticle Synthesis

Silver colloid was synthesized using a similar method to that originally developed by Leopold and Lendl.[136] While under vigorous stirring, 1 mL of hydroxylamine hydrochloride (NH_2OH•HCl, 167 mM) was added to 89 mL of sodium hydroxide (NaOH, 33.3 mM). Ten mL of silver nitrate ($AgNO_3$, 10 mM) solution was then rapidly added to the solution, and the solution was left stirring for 15 min at room temperature.

III.2.iii Nanoparticle Functionalization

The approach for nanoparticle functionalization and labelling was adapted based on the protocol previously described by Schechinger *et al*.[163] The oligonucleotide probes were designed with a THIOL end modification which allowed the probe to be immobilized on the nanoparticle surface. Briefly, the oligonucleotide solution of ssDNA labelled as Probe 1 was reduced by combining 100 µL of 20 mM TCEP with 100 µL of the oligonucleotide solution (100 µM). The sample was then left at room RT for 60 min.

Next, the solution was subjected to 3 consecutive wash cycles using a desalting column (3 kDa, Nanoseps) to remove existing reaction byproducts and TCEP in solution. For each cycle, the desalting column containing the sample was centrifuged (5 min at 5.0 rcf). The filtered waste was then removed from the bottom of the collection tube and 300 µL of suspension solution was added to the top of the desalting column. The first 2 wash cycles used DDW as the suspension solution. For the third and final wash, 0.3 M PBS solution (pH 7.4) was used. The sample was then collected and stored in 0.3 M PBS hybridization buffer. This procedure was repeated using the Probe 2 oligonucleotides.

The value for the number of immobilized oligonucleotides on the surface of a single nanoparticle used during nanoparticle functionalization was set at 1500 oligos/NP. Beer-Lambert's Law was used to calculate the concentration of each sample of reduced oligonucleotide using the extinction coefficients and absorption maxima of each probe as provided by IDT. Next, 1 mL of AgNPs was placed in a new vial. The calculated volume of Probe 1 was added to the vial, and the sample was left to shake overnight for approximately 8 hours. The following morning, a 250 mM solution of citrate/HCl buffer

(pH 3) was prepared and used to promote complete coverage of the nanoparticle surface. Citrate buffer (20 µL) was added to the AgNPs/DNA solution and then shaken for a few seconds. This process was repeated 3 times, adding a total of 60 µL of citrate solution to each sample. The sample was left shaking for 20 min and then centrifuged (20 min at 3.3 rcf).[164] The supernatant was collected and discarded, thereby removing any free floating oligonucleotides. The remaining pellet, formed at the bottom of the tube, was resuspended in PBS buffer (pH 7.4). The same process was carried out for Probe 2.

III.2.iv Labelling Using Raman Dye

Following functionalization, the solution of nanoparticles coated with Probe 1 was labelled using the photoactive dye, MGITC. No dye was added to nanoparticles functionalized with Probe 2. The value of dye molecules bound to each nanoparticle was set at 1000. The appropriate volume of dye was calculated and then added to the 1 mL solution of nanoparticles functionalized with Probe 1. The sample was left to shake for 1 h and then set aside to react overnight (~8 hours) at room temperature. The following morning, the sample was centrifuged (20 min at 3.3 rcf) and the supernatant was discarded, thereby removing the excess unreacted dye in solution. PBS buffer (pH 7.4) was then used to resuspend the remaining nanoparticle pellet.

III.2.v Oligonucleotide-Nanoparticle Probe for miRNA-17

A sandwich assay incorporating the nanoparticle probes was designed for the selective capture of miRNA-17.[151] This design consisted of two probes—Probe 1

(Sequence: $^{5'}$TAA GCA CTT TG HEG THIOL$^{3'}$) and Probe 2 (Sequence: $^{5'}$THIOL HEG CTA CCT GCA CTG$^{3'}$)—each complementary to half of the target miRNA-17 strand ($^{5'}$CAA AGU GCU UAC AGU GCA GGU AG$^{'3}$) (Figure 15). THIOL and HEG modifiers were added to enable the oligonucleotide probes to attach to nanoparticle surfaces. The binding of thiolated oligonucleotide probes on the nanoparticle surface was confirmed by a slight redshift in the LSPR or maximum peak in the absorption spectra (Figure S1). This small LSPR shift is due to an increase in the refractive index at the surface of the nanoparticle following the binding of the oligonucleotide probes.[165] The nanoparticle size was defined based on the absorption maximum at 408 nm and was then confirmed as ~35 nm using TEM images (Figure S2).

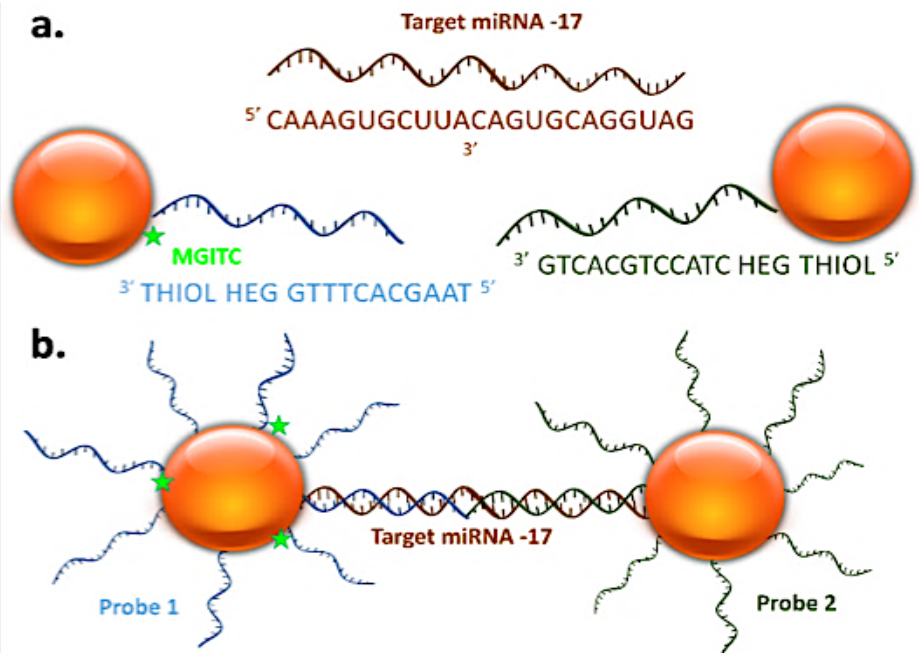

Figure 15 Basic overview of a) the sandwich assay design for miRNA-17 showing the individual probes and b) the resultant binding of miRNA-17 with the functionalized nanoparticles

The assay was engineered to enable the conjugated nanoparticles to remain suspended and stable in a physiological buffer solution (0.3 M PBS, pH 7.4) similar to blood plasma. The zeta potential, a parameter related to surface charge, is typically used for understanding nanoparticle stability. The effective surface charge is key to maintaining necessary electrostatic interactions that support the colloid suspension. A negative surface charge is typical of hydroxyl amine reduced metallic nanoparticles, like silver, due to the presence of orientation of the molecules that results in hydroxyl groups at their surface. These negatively charged surface ions provide the electrostatic repulsion to sustain the colloid.[166] The zeta potential of both the functionalized solution of nanoparticles was around -32 mV.[167]

The combined solutions of nanoparticles with Probe 1 and nanoparticles with Probe 2 produces the diagnostic assay. As described, the assay avoids premature nanoaggregate formation due to the incompatible base pairing because the orientation sterics of the two probes will form a dsDNA complex. Upon addition of the target miRNA-17 strand, nanoaggregates form, as gaps where the Raman reporter probe is located, on the order of 10^3 for this specific assay particles from the Probe 1 and Probe 2 populations bind to the same strand of miRNA-17. The high affinity between DNA and miRNA overcomes the repulsion of negatively charged nanoparticles, bringing particles close enough together to allow for their individual plasmons to couple. This generates 'hot spots' of increased SERS intensity at the particle gaps where the Raman reporter probe is located,[168] on the order of 10^3 for this specific assay (Figure 16). TEM images of the

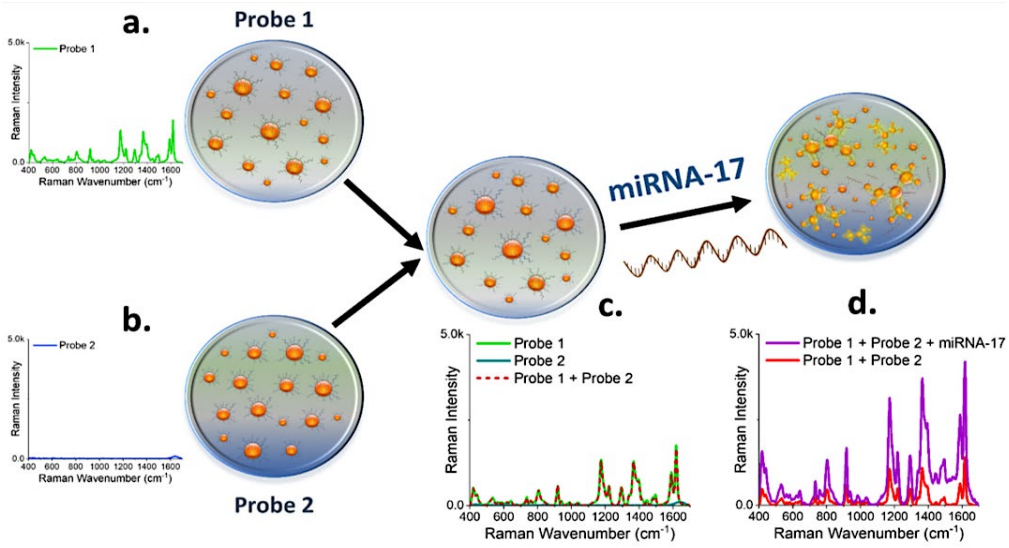

Figure 16 Representative SERS spectra of the assay nanoparticles: (a) Probe 1 provides a visible SERS spectra from its MGITC reporter dye; (b) Probe 2 lacks any discernible signal thereby demonstrating the DNA probes do not contribute to the spectra; (c) the combined miRNA-17 assay solution combining nanoparticle Probe 1 + Probe 2, which produces no change in the signal indicating no nonspecific DNA hybridization occurs between probes; (d) the assay response upon the addition of miRNA-17, which causes an increase in the SERS signal due to the formation of aggregates resulting from DNA-RNA hybridization

plasmonic nanoparticles aggregates resulting from the addition of miRNA-17 are provided in Appendix A (Figure S3).

III.2.vi Analysis of the SERS Assay's Response to miRNA-17 Presence

MGITC was used as the RRM to indirectly sense the target analyte, miRNA-17. This was performed by examining changes in the analyte's relative SERS intensity, which increases as a function of nanoaggregate formation. The area of known peaks at Raman wavenumbers of 1177 cm^{-1}, 1220 cm^{-1}, 1290 cm^{-1}, 1586 cm^{-1}, and 1618 cm^{-1} were used to

define the relative SERS intensity observed for different target concentrations. The Integrate Peak function in Origin Lab was used to calculate the peak area.

To reduce instrumental noise, Savitzky-Golay smoothing was applied.[169] The calculated values were plotted alongside their prospective target concentrations and then fit with a Hill curve. The curve was used to obtain a representative linear lookup table describing the relationship between the target concentration in solutions and the observed relative SERS intensity. The LOD and coefficient of determination were calculated to determine the lowest concentration that can be distinguished from a PBS blank. To determine the selectivity of the assay, 10 pM of a non-complementary strand of miRNA was added to the assay in lieu of miRNA-17. The resultant SERS spectra were analyzed and compared to the corresponding sample containing miRNA-17. This process was performed for 5 different non-complementary negative control strands: miRNA 34a-3p, miRNA 126a-3p, miRNA 155-3p, miRNA 210-3p, and U6.

III.2.vii Evaluation of SERS Assay in a Complex Biological Sample

The designed nanoparticle detection assay for miRNA-17 was further evaluated in diluted bovine serum to determine its functionality within a complex biological sample. The bovine serum was isolated from whole bovine blood by centrifuging the sample at 1.3 rcf for 10 min and collecting the supernatant. The supernatant (serum) was then diluted to 20% (*v/v*) in 0.3M PBS. The Raman spectra of the diluted serum solution was then collected with a 532 nm excitation laser using the same collection parameters previously described. The individual assay components along with the combined sensing assay were

each mixed with diluted bovine serum. The three sample solutions of nanoparticles were then incubated at room temperature. After 1 h, the SERS spectra of the different reference solutions of nanoparticles were collected. The designed sensing assay was further tested to confirm its quantitative capacity for miRNA-17 within bovine serum. The diluted bovine serum was doped with different concentrations of the target, miRNA-17. The assay components were combined with the target suspended in diluted bovine serum and incubated at room temperature for 1 h. The SERS signal was then collected and analyzed based on the previous methods.

To contribute to the complexity of the biological medium, the diluted bovine serum was doped with a non-complementary oligonucleotide strand in addition to the target miRNA-17. The non-complementary strand was chosen based on the results of the assay specificity study in PBS. In accordance with the earlier study, a concentration of 10 pM was used for both the target miRNA and non-complementary oligonucleotide strand. The resulting SERS spectra was then compared to data obtained from the assay combined with 10 pM of miRNA-17 in PBS and diluted bovine serum. In order to determine the presence of miRNA-17 prior to doping, the diluted bovine serum was analyzed using qRT-PCR.

III.3 Results and Discussion

III.3.i Proof of Concept for Detection of miRNA-17 Using SERS

The robustness of assay was first tested in PBS by individually examining the baseline SERS spectra of the two assay components—AgNPs functionalized with Probe

1 and labelled with MGITC, and AgNPs functionalized with Probe 2 only (Figure 16). The solutions of nanoparticles were then combined, and the SERS spectrum was collected and designated as the reference spectrum.

The SERS spectra of the combined sensing assay had a maximum signal intensity comparable to that of the solution of nanoparticles with Probe 1. This was as expected, indicating that there is no nonspecific binding between the probes when no miRNA is present. The solution of nanoparticles with Probe 2 had a negligible signal due to the absence of a Raman reporter molecule, thus validating that there is no contribution to the spectra from the DNA probes themselves.

The sensing assay was then further analyzed with the addition of 1 nM of miRNA-17. A previous study revealed that a 1 h incubation or reaction time was required for the assay to reach steady-state—as indicated by a stable SERS maximum.[163] The SERS spectra for the sensing assay with 1 nM of miRNA-17 was obtained following this incubation period. The resultant spectra had a notably higher maximum relative SERS intensity, hybridization of the target miRNA and oligonucleotide probes by way of formation of aggregates (Figure 16). These findings indicate the assay's potential to successfully detect the presence of miRNA-17. To avoid particle saturation the assay was optimized based on the sensing criteria and the necessary detection range for miRNA-17.

III.3.ii Quantification of miRNA-17 Using Normalized SERS

The nanoparticle assay as described was then used to determine the quantitative capacity of MGITC to indirectly sense for miRNA-17 in both PBS and serum. The assay

was first tested in PBS without the presence of non-complementary competing analytes. The SERS intensity of the assay was examined for different concentrations of miRNA-17 ranging from 10 fM to 10 nM (Figure S4). As discussed in the previous section, a visible jump in the relative SERS intensity occurs when miRNA-17 is added and appears at first glance to be concentration dependent in the range of 1 pM - 1 nM. The spectra displayed represent the mean of three individual replicates gathered for each incremental miRNA-17 concentration. The signal was baseline corrected prior to peak analysis using asymmetric least squared smoothing (Figure 17). [170] The overlay of the average spectra obtained for the various sample concentrations in Figure 17 visually suggests a possible relationship between target concentration and SERS intensity.

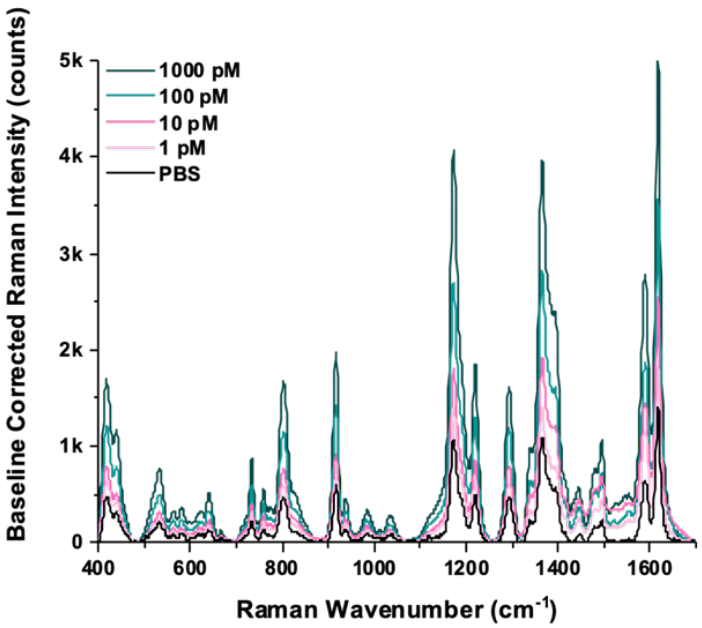

Figure 17 Baseline-corrected SERS spectra of the nanoparticle assay in response to 1pM - 1nM miRNA-17, demonstrating the concentration dependence of the assay

The largest relative SERS intensity was observed when at least 1 nM of miRNA-17 was present. Additionally, as the amount of miRNA in solution decreased to less than 1 pM, the decreases in relative SERS intensity became negligible. This same general trend was observed by Graham *et al* for a DNA-DNA hybridization assay suspended in PBS.[164] Thus, initial results indicate that the designed scheme may be altered to suit various nucleic acid and biomarker conformations.

III.3.iii Multiple Peak Analysis of SERS Signal to Determine LOD

To more closely study the relationship between target concentration and the resultant SERS signal, the relative SERS intensity was defined by calculating the peak area for multiple characteristic peaks associated with MGITC. The characteristic peaks chosen were centered at 1177 cm^{-1}, 1220 cm^{-1}, 1290 cm^{-1},[171] 1586 cm^{-1}, and 1618 cm^{-1} [158] (Table 3). These peaks are commonly used to analyze the SERS spectra of MGITC, and they also help avoid overlap peaks from common interference from blood located in the fingerprint region, such as aromatic rings (828, 872, 1000, 1110, 1204, 1546 cm^{-1}),

Table 3 Vibrational peak assignment for five characteristic peaks of MGITC

RAMAN PEAK (cm^{-1})	SERS PEAK (cm^{-1})	VIBRATIONAL ASSIGNMENT
1176	1177	In-Plane C-H Bend, Benzene v_9 Mode
1221	1220	N-C Stretch, NR_2 Bend
1295	1290	In-Plane C-H and C-C-H
1590	1586	Stretch/Bend of In-Plane Ring
1619	1618	Stretch of C-C and N-Phenyl Ring

methylene vibrational modes (1266, 1320, 1365, 1449 cm^{-1}), carboxylic group vibrations (620, 964, 1397, 1584 cm^{-1}), stretching of disulfide bonds (500 – 550 cm^{-1} and 650 – 675 cm^{-1}), and α-helical secondary structures (890-960 cm^{-1}).[172]

The average area calculated for each chosen peak was then binned by peak location as a function of concentration (error bars correspond to 1 standard deviation) (Figure 18). Before normalization, the peaks at 1177 cm^{-1} and 1618 cm^{-1} provided the largest relative SERS intensity when examined across different miRNA-17 concentrations and thus would be expected to provide the lowest LOD, whereas the peaks with weaker relative SERS intensity were associated with the peaks centered at 1220 cm^{-1} and 1290 cm^{-1}. Interestingly, when normalized to the control spectra (assay without any miRNA, labelled PBS only), all peak locations exhibited a similar concentration dependence (Figure 18(b)), but the lowest LOD was associated with the less obvious peak at 1586 cm^{-1}.

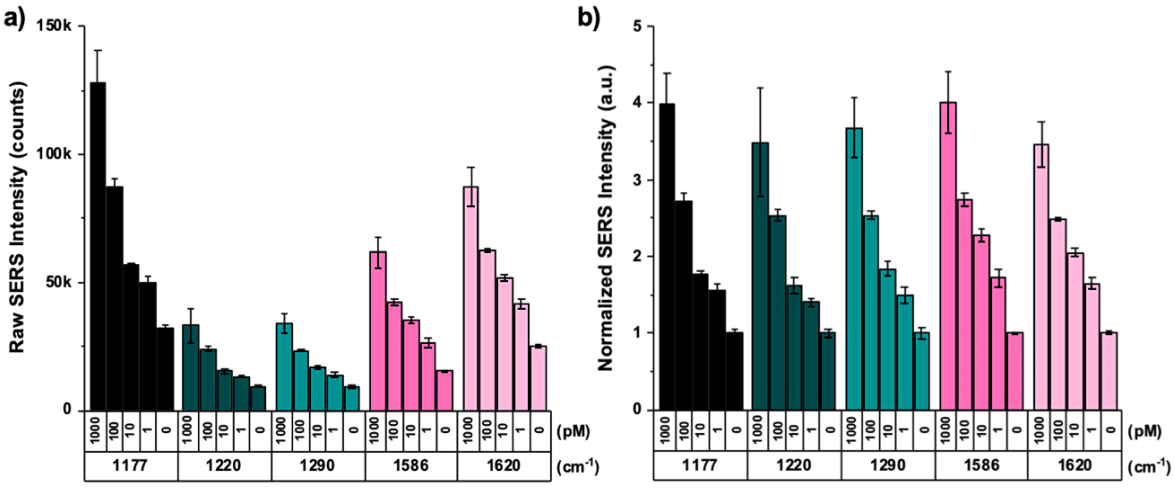

Figure 18 Bar graphs defining the a) peak area SERS intensity at five characteristic peaks of MGITC for various miRNA-17 concentrations; b) the data for the peak area SERS intensity normalized to PBS

The LOD is calculated based on the intensity limit determined at each peak. The I_{LIMIT} was calculated based on the average SERS intensity and standard deviation compared to the PBS reference (Equation 2)[169]

$$I_{LIMIT} = I_{BLANK} + 3 * SD_{BLANK} \quad \text{Equation 2}$$

The I_{LIMIT} was then used to specify the miRNA-17 concentration associated with the LOD. The representative equations that relate miRNA-17 concentration (x) and SERS signal intensity (y) for each of the characteristic peaks was used to determine the corresponding target concentration for the LOD. Linear regression analysis was used to relate signal intensity to target concentration for the I_{LIMIT} as seen in Equation 3

$$y = m * log(x) + k \quad \text{Equation 3}$$

Table S2 provides the values for the equation constants and the calculated target concentration for and intercept calculated for each peak. The target concentration associated with the calculated I_{LIMIT} was determined using a representative equation for predicting miRNA-17 concentrations from relative SERS intensity. The LOD ranged from 0.16 pM (Peak at 1586 cm^{-1}) to 0.91 pM (Peak at 1220 cm^{-1}) (Table S1and Table S2).

III.3.iv Evaluation of SERS Detection Assay Dose-Response Curves to Determine Variations in Relative Binding Avidity & Dynamic Range

The data was replotted using a scatter plot and fit to a curve to better visualize the relationship between peak area and target concentration. The SERS intensity at various miRNA-17 concentrations was fit to a dose-response curve using the Hill Equation:

$$y = START + (END - START)\frac{x^n}{k^n + x^n} \quad \text{Equation 4}$$

However, the Hill1 Equation is only valid for intensities within the range defined by the START and END values (Table S5). As a result, the target concentrations calculated based on the Hill1 equation were undefined for the intensity values at the LOD. To determine the representative Hill equation, the miRNA-17 detection assay was tested using a concentration range of 0.01 pM to 10000 pM. The SERS spectra obtained for this entire range is provided in Figure S4. Across data sets, a similar general sigmoidal dose-response was observed corresponding to different locations of the peak center, thereby signifying coherence in the assay response regardless of which peak is analyzed. Data was then fit to a dose-response curve using the Hill1 equation in Origin Pro (Figure 19). From these fits, we observed effective dissociation constants of 129 pM, 143 pM, 155 pM, 756 pM, and 195 pM for the peaks centered at 1177 cm^{-1}, 1220 cm^{-1}, 1290 cm^{-1}, 1586 cm^{-1}, and 1618 cm^{-1}, respectively (Table S3). The values for the dissociation constant and Hill coefficient are provided alongside the calculated statistical fit (COD and adjusted R^2) for

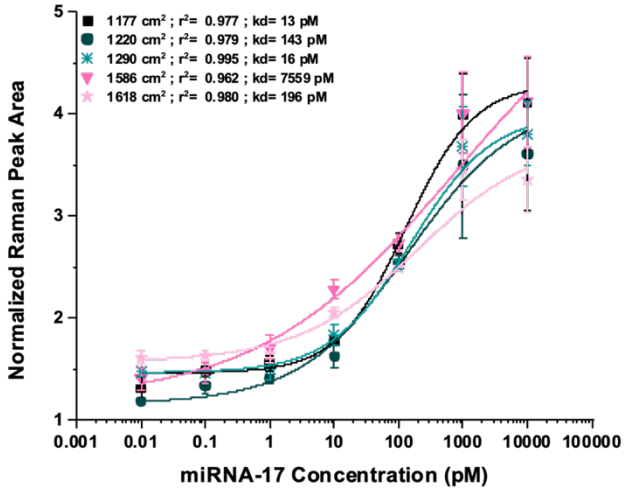

Figure 19 The semi-log plot of the peak area for the characteristic peaks of MGITC (1177 cm^{-1}, 1220 cm^{-1}, 1290 cm^{-1}, 1586 cm^{-1}, and 1618 cm^{-1}) fit to the Hill1 equation

the Hill1equation for five characteristic peaks of MGITC whose intensity is associated with the capture probes, and in turn relates to the sensitivity of the assay. A higher binding affinity corresponds in an increase in the sensitivity of the detection assay.[173] A Hill coefficient of less than 1 signifies negative cooperativity in which the binding of a ligand miRNA-DNA binding event. The k_d describes the affinity between the target analyte for (miRNA-17) to a receptor (capture probes) decreases the binding affinity of subsequent receptors.[174] All five characteristic peaks produced a n of less than 1, indicating that the assay exhibits negative cooperativity, as expected due to steric hindrance caused by the dense packing of ligands on the nanoparticle surface. However, it is worth noting that, depending on the peak being analyzed, this value ranges significantly from 0.284 - 0.820, despite being derived from the same binding event. This thus highlights the importance of multi-peak analysis and peak choice in the design of SERS assays with a single reporter molecule. Ultimately, the Hill coefficients were used to define a representative equation relating SERS signal intensity with miRNA-17 concentration (Equation 4).

Paired t-tests ($\alpha = 0.05$) were used to determine if the samples tested could be differentiated with 95% confidence (Table S4 and Table S5). The peak centered at 1618 cm^{-1} was chosen to perform these tests because it had the best linear fit in the 1 pM – 1 nM range (Table S6). The signal for each miRNA-17 concentration tested was differentiable with 95% confidence from the baseline signal for the assay with PBS, without any correction factors applied. However, the signal was not differentiable at the highest (10 nM and 1 nM) and lowest target concentrations (1 pM, 100 fM, and 10 fM)

tested. Therefore, the range of quantification for the designed assay was determined to exist from 1 pM to 1 nM, as was expected by our earlier visual assessment of the spectra.

A strong logarithmic fit was observed across all peak locations, irrespective of which peak was used to generate the calibration curve. That is, a statistically significant relationship between the relative SERS intensity and the concentration of the target miRNA-17 was observed at a significance level, α, of 0.05. Thus, the equations for each dataset have high predictive value. The linear regression for the peak at 1618 cm^{-1} was the most statistically significant. It provided the highest values for the correlation coefficient ($R = 0.975$) and the smallest p-value ($p = 0.0253$).

Additionally, this peak's calibration curve showed the second strongest raw SERS intensity, thus making it easily detectable in post processing. The data collected from this peak were used to develop a representative lookup table for predicting miRNA-17 concentrations from relative SERS intensity (Figure 20). Linear regression analysis for the

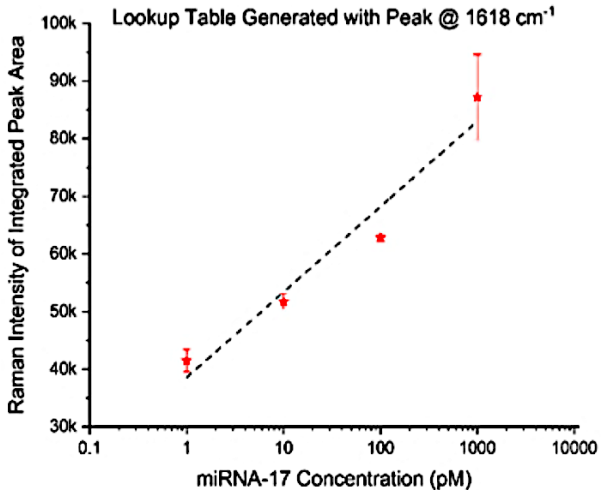

Figure 20 The semi-log plot with the representative logarithmic equation *(*Equation 5*)*, where *x* is the concentration in pM and *I* is the SERS intensity in counts

peak at 1618 cm^{-1} resulted in the following representative logarithmic equation:

$$Intensity = 1.48 * 10^4 \, log(Concentration) + 2.16 * 10^5 \qquad \text{Equation 5}$$

A summary of the figures of merit, which includes parameters typically used for analyzing SERS assays, is provided in Table 4. While the results provided in Table 4 represent the overall performance of the designed SERS biomarker detection assay, they are predicated on the peak centered at 1618 cm^{-1}.

The significance of the peak location for SERS signal intensity was further examined using descriptive statistics and one-way ANOVA. Using a significance level (α) of 0.05, ANOVA analysis determined that Raman peak location significantly influenced the SERS signal intensity (Table S7). This information substantiates the data obtained using regression analysis, as demonstrated by the variation in slope and intercept across peaks. Therefore, identifying a statistically significant peak is key in determining the

Table 4 Summary of figures of merit for the miRNA-17 detection assay using the peak centered at 1618 cm^{-1}

	PEAK AT 1618 cm^{-1}
SENSITIVITY	1.48 x 10^4 (counts/pM)
LIMIT OF DETECTION (LOD)	0.26 pM
DYNAMIC RANGE (LOQ)	1 - 1000 pM
INTERCEPT (BASELINE INTENSITY)	2.16 x 10^5 (counts)
PEARSONS CORRELATION	0.975
p-VALUE FOR H_0: SLOPE=0	0.0253

relationship between signal intensity and concentration of the target analyte. A one-way ANOVA was also used to confirm the statistical significance of the relationship between miRNA-17 concentration and SERS signal intensity (Table S8).

The figures presented in Table 4 indicate the potential of SERS as a diagnostic platform for the early detection of preeclampsia as compared to traditional techniques. The designed sensor has a lower LOD than both northern blotting and microarrays, and a comparable LOD to RT-PCR. This high degree of sensitivity and quantitative capacity makes a SERS coupled nanoparticle detection assay an attractive alternative to current laboratory techniques. Indeed, the designed SERS assay reliably produces quicker results than traditional methods because it requires fewer steps.

III.3.v Specificity of miRNA-17 Assay

The specificity of the assay for sensing miRNA-17 was determined using 4 different non-complementary strands of miRNA (34a-3p, 126a-3p, 155-3p, 210-3p) and a small strand of non-coding nuclear RNA (U6). A 10 pM concentration of each of the non-complementary strands was added in place of the complementary strand (miRNA-17). The spectra analysis was performed by calculating the total area for the SERS peaks centered at 1177 cm^{-1}, 1220 cm^{-1}, 1290 cm^{-1}, 1586 cm^{-1}, and 1618 cm^{-1} (Figure 21).

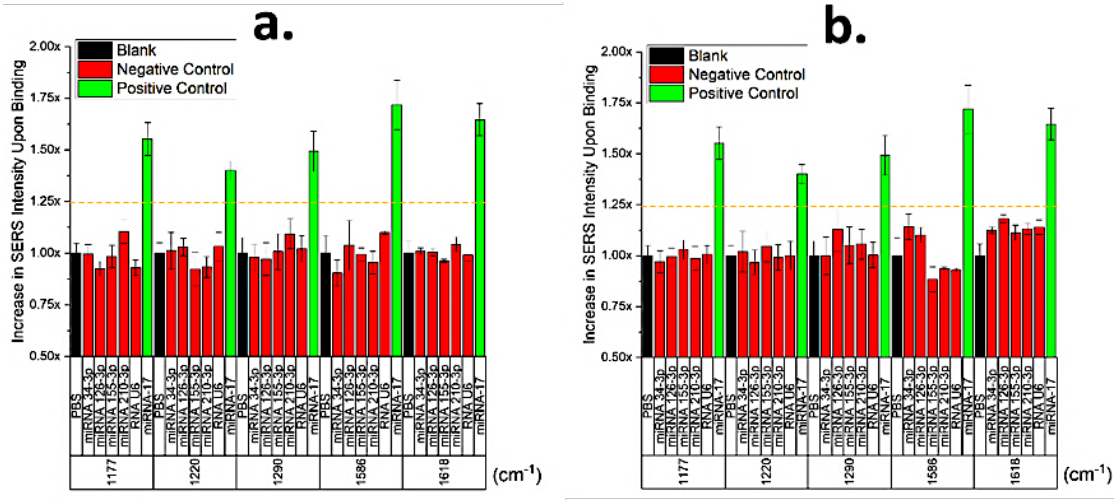

Figure 21 Peak area normalized to PBS, of the various a) forward and b) reverse non-complementary strands of negative control RNA compared to the blank and positive control (target miRNA-17). In both scenarios, a threshold can be set at a signal intensity increase of *1.25x* that of PBS

The combination of sensing assays with non-complementary target strands provided SERS spectra with low relative intensities comparable to that observed for the blank (Figure 21). The low relative intensity indicates the absence of large aggregates that enhance the SERS signal; the SERS signal observed is most likely due to the localized surface plasmon effect. In comparison, the assay containing the complementary target, miRNA-17, produced drastically higher SERS intensity due to its potential to form aggregates with high-energy "hot spots." Once again, the largest values for peak area were associated with the peaks centered at 1177 cm^{-1} and 1618 cm^{-1}, and the smallest peak areas were calculated for the peaks centered at 1220 cm^{-1} and 1290 cm^{-1}. Furthermore, paired t-tests ($\alpha = 0.05$) were used to determine the differentiability of the non-complementary strands from the baseline (Table S9). The forward and reverse of the non-complementary strands were not differentiable with 95% confidence from the assay with PBS.

Overall, the results collected using both complementary and non-complementary strands of miRNA indicate that the assay exhibits a degree of specificity for the target, miRNA-17. When the assay was introduced to similar strands of miRNA, the resultant signal fell below the LOD. Thus, based on the weak signals observed with the non-complementary strands of miRNA, a degree of selectivity within the assay can be inferred.

III.3.vi Analysis of SERS Assay in Complex Biological Medium

The designed nanoparticle detection assay was then tested using diluted bovine serum (20% *v/v*), a complex biological medium similar to human serum. The Raman spectra of the diluted bovine serum solution were first collected to determine the underlying baseline Raman signal present when testing the detection assay in serum (Figure 22). The resulting spectra contained multiple characteristic peaks. These peaks exist because of the various biomolecules present in serum [175, 176] (Table S10). To

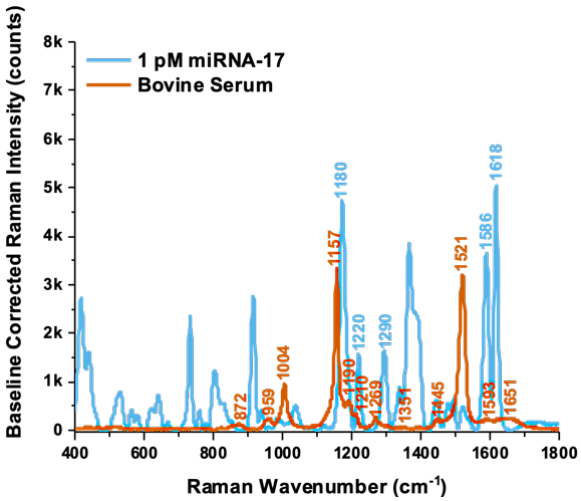

Figure 22 Raman spectra of diluted bovine serum (20% *v/v*) with the significant peaks labelled, alongside the SERS spectra of the detection assay

determine potential peak overlap, the MGITC SERS signal for the detection assay with 1 pM of miRNA-17 was plotted alongside the Raman spectra for serum (Figure 22). The resulting plot showed serum peaks, between 1000 cm^{-1} to 1550 cm^{-1}, that could potentially influence the signal intensity of the 5 characteristic peaks of MGITC previously analyzed. While none of the serum peaks directly coincided with the specific peaks examined for MGITC, some peak overlap did exist. This overlap primarily occurred for the MGITC peaks centered at 1180 cm^{-1}, 1220 cm^{-1}, and 1290 cm^{-1}, with the most overlap occurring at 1180 cm^{-1}. Before adding the designed nanoparticle detection assay, the bovine serum was analyzed using qRT-PCR to determine if miRNA-17 was present in the sample. The results indicated that a small concentration of miRNA-17 did exist within the bovine serum sample (Figure S5). This underlying miRNA-17 concentration was referred to as the baseline signal (Figure S6).

The nanoparticle detection assay suspended in diluted bovine serum was analyzed at various miRNA-17 concentrations (Figure 23(a)). To ascertain the relationship between target concentration and signal intensity, the assay was tested from 10 fM to 10 nM (Figure S7). The same overall trend was observed as described above for PBS. However, the maximum signal intensity was collectively higher for the results collected in serum as compared to PBS. A comparison of the characteristic SERS spectra showed that the results from the assay in serum produced a more prominent peak at 1180 cm^{-1} with a higher maximum signal intensity. This likely resulted from the underlying Raman signal of the serum solution and its existing peak overlap with the spectra for MGITC. Similarly, the integral for each of the five characteristic peaks of MGITC was calculated from the

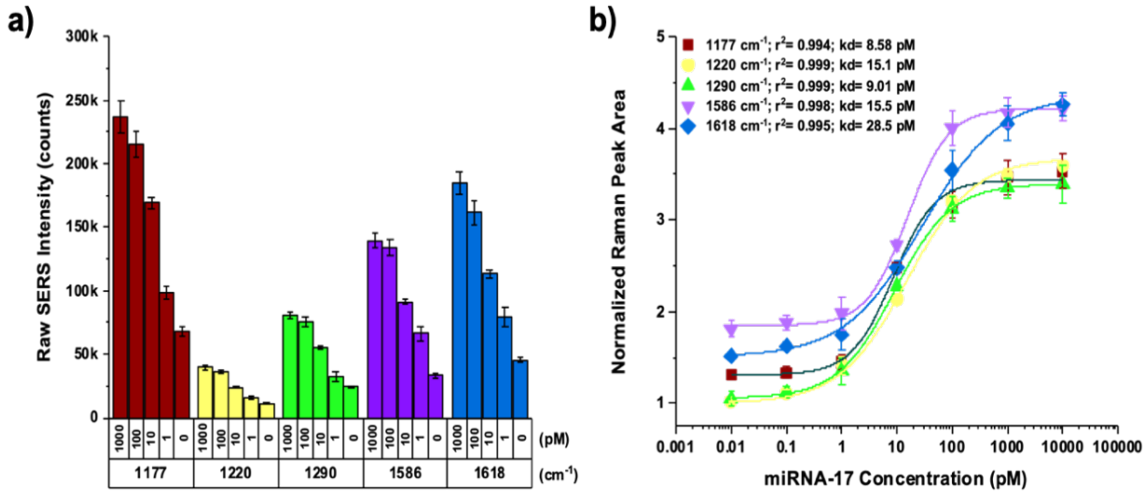

Figure 23 The (a) integrated peak area of the characteristic peaks of MGITC for the assay in diluted bovine serum and (b) the Hill1 fit for the relative equation of the characteristic peaks

resultant spectra of the assay in serum. The calculated values for the integrated peaks once again resulted in a higher SERS intensity compared to the assay in PBS.

Due to the differences in the maximum signal intensity and the presence of an underlying baseline signal, further comparison was performed based on the normalized results of the assays (Figure S8). The results from the assay in serum were normalized to the control spectra: the Raman spectra of the assay in serum without the target analyte. The LOD was then calculated based on the normalized results of the integrated peak area (Table S2). The values for the LOD calculated for assay in serum ranged from 0.22 pM (1586 cm^{-1}) to 2.89 pM (1220 cm^{-1}). Compared to the LOD for the assay in PBS, the assay in serum produced slightly higher values for the LOD. When tested in complex solutions like serum, increases in the LOD have been reported for sensing assays with uncoated functionalized nanoparticles.[177, 178] This increase is commonly attributed with serum-

protein-induced dissociation of Raman reporter molecules and capture probes from the nanoparticle surface.[52, 179] Thus, the observed increase in LOD for the assay in serum indicates some degree of dissociation of the reporter molecules and oligonucleotide probes from the nanoparticle surface.

The normalized results of the integrated peak area from assay in serum were fitted to a Hill1 equation to establish a representative equation of the assay's sensing characteristics (Figure 23(b)). The sensing parameters obtained from the Hill1 Fit include the dissociation constant and the Hill coefficient (Table S5). As compared to the assay in PBS, the assay in serum produced lower values for the apparent dissociation constant obtained from the following peaks: 8.58 pM (1177 cm^{-1}), 15.1 pM (1220 cm^{-1}), 9.01 pM (1290 cm^{-1}), 15.5 pM (1586 cm^{-1}), and 28.5 pM (1618 cm^{-1}). A decrease in the k_d is related to an increased affinity for the target, miRNA-17.[180] The observed shift in the k_d is likely due to the dissociation of oligonucleotide probes from the nanoparticle surface, previously mentioned. The dissociation results in a decrease in the probe density on the nanoparticle surface, which for a fixed sample volume, is linked to the apparent k_d.[181]

In addition to the dissociation constant, variation in the reported Hill coefficient, n, among the different peaks indicates changes in the detection assay's sensing efficiency when incorporated into a complex biological sample such as serum. At each peak examined, the Hill coefficient for the assay in PBS had a value of less than 1, indicating the assay exhibited negative cooperativity. Meanwhile, the assay in serum positive exhibited more variation in the Hill coefficient with the peaks at 1177 cm^{-1} and 1586 cm^{-1}, resulting in values greater than 1 or cooperativity. The remaining peaks centered at 1220

cm^{-1}, 1290cm^{-1}, and 1618 cm^{-1} produced negative values for the Hill coefficient. Therefore, the cooperativity for the assay in serum varied based on peak location so the overall cooperativity of the assay could not be determined.

The serum data was also subjected to linear regression analysis resulting in a logarithmic fit of the representative equation of the assay. Once again, the relationship between the SERS intensity and target concentration was determined to be statistically significant ($\alpha = 0.05$). Compared to predictive equations derived from the assay PBS, the assay in serum yielded a stronger logarithmic fit at each of characteristic peaks (Table S6). Specifically, the peak at 1618 cm^{-1} had the highest R-value of 0.992 while also having one of the smallest p-values ($p = 0.0162$).

The competency of representative equations, derived from different curve fitting methods, was evaluated using the additional miRNA-17 concentrations of 5 pM and 30 pM. The resultant samples consisted of the detection assay suspended in separate solutions of diluted bovine serum doped with either 5 pM or 30 pM of miRNA-17. These samples were then used to assess the different representative equations obtained from both PBS and serum. The resultant SERS spectra were collected for both sample solutions of nanoparticles. The equations were tested using the assay in serum and evaluated in regard to the peak at 1618 cm^{-1}. The resulting SERS spectra were obtained for the assay with 5 pM and 30 pM of miRNA-17 (Figure 24). The peak at 1618 cm^{-1} was chosen based on its superior overall fit. The integrated SERS intensity calculated for the two assays doped with 5 pM and 30 pM of target was $1.02 * 10^5$ counts and $1.35 * 10^5$ counts for the assay with 30 pM of target. These values were then used to assess the representative equations.

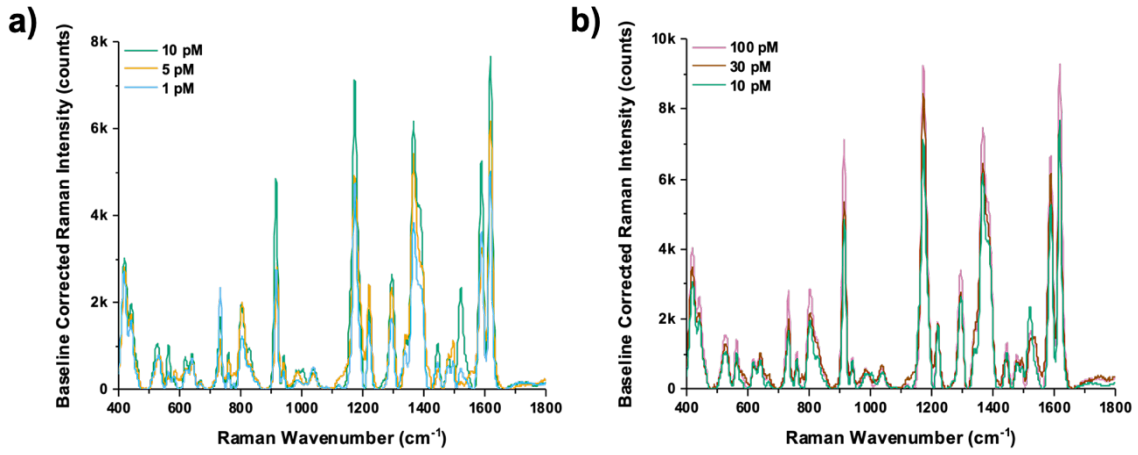

Figure 24 The test concentrations of (a) 5 pM and (b) 30 pM were plotted individually alongside the upper and lower concentrations used to obtain the representative equation.

Likewise, the two representative equations previously derived based on the assay in PBS were evaluated using alongside the equations obtained from assay in serum. The equations were rearranged to solve for the target concentration with regards to the observed SERS intensity. Ideally, the calculated value provided by the representative equations should correspond to the known target concentration associated with either signal intensity. The calculated target concentrations are provided in Table 5 based on the

Table 5 Comparison of the representative equations calculated for assay in PBS and serum using both linear regression analysis and Hill fit

	LINEAR REGRESSION ANALYSIS				HILL FIT			
	PBS		Bovine Serum		PBS		Bovine Serum	
	SERS Intensity	Concentration (pM)	SERS Intensity	Concentration (pM)	SERS Intensity	Concentration (pM)	SERS Intensity	Concentration (pM)
5 pM	1.02E+05	1.98E+04	1.02E+05	4.70	1.02E+05	Undefined	1.02E+05	5.02
30 pM	1.35E+05	3.58E+06	1.35E+05	37.77	1.35E+05	Undefined	1.35E+05	30.70

on the representative equations resulting from linear regression analysis or Hill fit of either the assay in PBS or the assay in bovine serum.

The representative equation obtained using the Hill fit for the assay in bovine serum was the best for predicting target concentration based on the integrated peak intensity. Compared with linear regression analysis, the Hill fit was able to account for the dose-response nature of the sigmoidal curve. However, the use of the Hill equation is limited to the upper and lower bounds, START and END, of the linear portion of the sigmoidal curve. As a result, intensity values outside this range result in an 'undefined' value. The equations calculated using linear regression have no restrictions and can be used with any value. The results also showed the representative equations calculated based on the assay in PBS were not indicative of the assay in a more complex medium.

III.4 Summary

In summary, biomarker detection is a useful tool for diagnosing disease, but its application in clinical settings is limited. In this paper, a SERS-based assay using functionalized metallic nanoparticles labelled with Raman reporter molecules was designed, developed, characterized, and used to target miRNA17 in solution. The design showed successful detection of miRNA-17 within the range of 1 nM to 1 pM. Linear regression analysis of the data demonstrated statistical significance, and it was used to develop an equation for predicting the target concentration based on the observed relative SERS intensity. Increases in SERS intensity were only observed to be specific to miRNA-17 when compared to 5 different non-complementary strands. The detection of miRNA-

17 in this study shows that SERS-based biomarker detection has a high potential to facilitate diagnosis of preeclampsia and potentially other diseases.

Furthermore, our results highlight the value of multiple peak analysis. The capacity of the designed SERS assay for detecting and quantifying miRNA-17 was calculated using the peak area of 5 characteristic peaks of MGITC. While each one of the characteristic peaks was effective in establishing a relationship for quantifying miRNA-17, the combined data demonstrate the consistency of the results obtained. This is important because multiple peaks are rarely simultaneously analyzed when evaluating SERS spectra; SERS results are thus often reported based on arbitrary binding ranges and commonly omit calculations of fit and significance. Indeed, differences in SERS spectra analysis and the inconsistency of reported results have led to poor reproducibility. In contrast, multiple peak analysis provides more comprehensive results and comparative determinations of optimal binding ranges, as well as additional insight into the analysis methods of others. As advances in computing emerge, instantaneous multiple peak analysis may efficiently promote the reproducibility of the optical platform. Thus, our designed nanoparticle detection assay for miRNA-17 demonstrates the diagnostic potential for using SERS to create a non-invasive platform for miRNA detection.

CHAPTER IV

A MULTIPLEX 3D PAPERFLUIDIC PLATFORM FOR SERS DETECTION OF PREECLAMPTIC BIOMARKERS

IV.1 Introduction

Nowadays, a multitude of different cellulous paper membranes are commercially available that vary in pore size, flow rate/ particle retention, and thickness. These characteristics play a significant role in dictating flow and therefore need to be chosen based on the function and composition of the designed sensing assay.[76] In regard to the designed assay for miRNA detection, Whatman Grade 1 Chromatography paper was used for all of the layers except for the final layer, the capture readout layer. The high affinity of nitrocellulose for proteins allows for direct immobilization of proteins without the need for modification. Additionally, the small pore size and uniform membrane, are characteristic that make nitrocellulose a useful capture membrane.[182]

In order to control the multidirectional flow within 3D paper fluidic devices, hydrophobic barriers are created via physical/chemical modification of the cellulose membrane.[183, 184] Compared to other approaches, wax patterning is commonly used because it's a low cost, quick and simple technique that is useful for large scale prototyping.[92]

IV.1.i Overview

The detection assay for the paper fluidic device was adapted from the previously designed assay for miRNA-17 in solution. The solution-based assay used free floating functionalized nanoparticles in solution to create a sandwich assay capable of quantifying miRNA-17 concentration within 1 nM to 1 pM range.[185] Compared to the assay solution, the paper-based assay required one portion of the sandwich assay to be immobilized onto the paper surface within a specific region of the fluid pathway. A streptavidin-biotin binding approach was based on the natural high affinity of nitrocellulose membranes for proteins. Streptavidin is large protein that is easily immobilized by absorption.[98] Meanwhile, biotin can easily be added to an oligonucleotide by replacing the thiol end modification with a biotin modification. The strong non-covalent bond between streptavidin and biotin allows the probe to be immobilized when combined with streptavidin.[186] With one probe immobilized on the surface, the other subsequent probe can remain functionalized to gold nanoparticles labeled with MGITC.

IV.2 Experimental

IV.2.i Instrumentation

The size and zeta potential of the synthesized gold nanoparticles were determined using a Zetasizer Nano ZS90 (Malvern, UK). The absorbance spectra of the various assay components were obtained with an Infinite®200 Pro multimode microplate reader (Tecan, Switzerland). The SERS spectra were obtained using the Ocean Optics IDRaman Mini.

IV.2.ii Overview of Paper Fluidic Platform Design

The designed 3D paper fluidic platform, including the individually wax patterned layers, is provided in Figure 25. This figure features the path of fluid flow as directed by the designed hydrophobic barriers. The circular holes observed on the outsides of the top three layers behave as viewing windows which allow the user to observe the potential color change of the control line and test line. Furthermore, the viewing window is used to direct the user to the alignment of the handheld Raman microscope.

IV.2.iii Gold Nanoparticle Synthesis and Characterization

Gold nanoparticles were synthesized using a modified version of the Turkevich Method.[187] 1mM $HAuCl_4$ was added to 100 mL of DDW water. The solution was then heated while vigorously stirring. Once boiling, 15 mL of 1% (*w/v*) sodium citrate was added to solution. While maintaining vigorous stirring, the solution was left boiling for 15 min to allow for nanoparticle formation. During this time, a visible change in color was

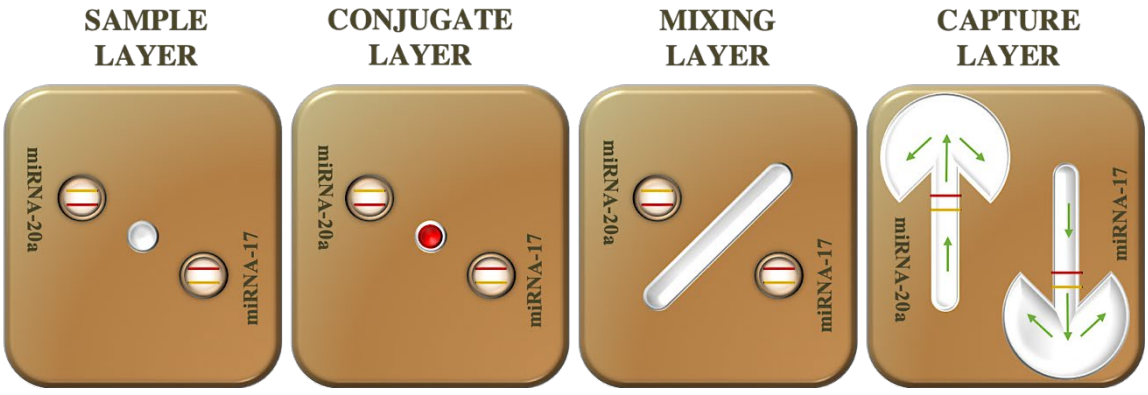

Figure 25 An overview of the wax patterned design used for each layer for multiplexed SERS detection of the two specific PE related biomarkers and control

observed that resulted in a deep red. The nanoparticle solution was then removed from heat and left to cool at room temperate. The highly concentrated nanoparticle solution was diluted by a factor of 10. The Extinction spectrum of the diluted nanoparticle solution produced an absorbance maximum of 0.234 (λ_{max} = 520 nm). Based on the absorbance data, the average diameter of the nanoparticles in solution was estimated as ~16 nm. Furthermore, the maximum absorbance was used to calculate the nanoparticle concentration. Using the Beer-Lambert Equation and an extinction coefficient of 3.56 $*10^8$, [188, 189] the concentration was calculated to be 1.15 * 10^{-5} M.

IV.2.iv Design of Sensing Probes for Dual Biomarker Detection

As seen with miRNA-17 and miRNA-20a, miRNAs exhibit a high degree of homogeneity and as a result require highly specific sensing mechanisms. The RNA sequences for miRNA-17 and miRNA-20a are both 23 nucleotides long and only differ by two nucleotides. Therefore, if sensing probes for miRNA-20a were designed using the previous approach created for miRNA-17, it would result in two sensing probes that each differ by only one nucleotide.(Figure 26) Moreover, having only one mismatched

Figure 26 Overview of the design of the sensing probes for miRNA-17 and miRNA-20a

nucleotide increases the likelihood of nonspecific binding and false positives for both strands of miRNAs. As a result, the sensing assays for miRNA-17 and miRNA-20a were redesigned to include both mismatched bases within one of the two probes. The subsequent probe would therefore be identical to both assays. In order to increase the specificity of the assay, the sensing probes for both Additionally, having fewer probes, decreases the amount of optimization necessary to achieve ideal binding conditions. As a result, the assay was designed to include a single universal sensing probe and two target-specific capture probes. In order to distinguish between the two analytes, the target-specific capture probes were immobilized on two different regions of the NC membrane. One region would be specific to miRNA-17 while the other region would be specific to miRNA-20a. The subsequent universal sensing probe would be functionalized to the gold nanoparticles.

IV.2.v Nanoparticle Functionalization of Universal Sensing Probe

The universal sensing probe was reduced by combining 100 µL of 100 µM Probe solution with 100 µL of 100 mM TCEP. The solution was then incubated for 1 h at room temperature. Once reduced, the solution was filtered using a standard desalting column (3 kDa, Nanoseps). The column was centrifuged for 5 min at 5.0 rcf.

In view of functionalization, 2 mL of AuNP solution was obtained and underwent continuous mixing using a shaker. While shaking, 60 µL of reduced probe was added to 2 mL of nanoparticle solution to achieve a functionalization concentration of 5000 oligos/AuNPs. The solution was left shaking to allow the samples to interact. After 5 min,

120 uL of sodium citrate buffer [250 mM, pH 3] was added to solution while shaking. The solution remained shaking for another 5 min, during which time, 20 μL of the RRM, MGITC [10 mM], was mixed into solution. The sample continued shaking for a final 5 min to allow for optimal functionalization. Any remaining oligonucleotide probe in solution was removed by centrifugation (9.5 rcf, 10 min). Following centrifugation, the supernatant was discarded, and the nanoparticle pellet was resuspended in 100 μL of eluent buffer (20 mM Na_3PO_4, 5% (*w/v*) BSA, 10% (*w/v*) sucrose, and 0.25% (*v/v*) Tween-20 in 0.3M PBS). The resultant solution had on OD of 5.

IV.2.vi Fabrication of Paper Fluidic Platform

The paper fluidic platform was fabricated using a multistep approach involving the design of fluid flow using hydrophobic barriers, chemical pretreatment of hydrophilic regions, and construction of the 3D sensing platform. A Xerox ColorCube 8580 printer was used to print the individual patterned layers shown in Figure 25. The top 3 layers (Sample Layer, Conjugate Layer, and Mixing Layer) were printed on Whatman Grade 1 Chromatography paper. The printed paper was heated at 120 °C for 1 min. The paper was placed in the oven with the wax side facing up to allow wax to penetrate down through the porous membrane. The paper was then cooled at room temperature. Notably, nitrocellulose is a highly flammable substance. In order to avoid degradation, an alternative approach was used to melt the printed wax and create a hydrophobic barrier. The membrane was slowly passed between two metal plates that were heated to 50 °C.

This allowed for enough heat to melt the printed wax on the top of the membrane while minimizing the effects of high temperature on membrane degradation.

A double-sided adhesive was used to bind the different paper layers. Using a benchtop cutting plotter, the adhesive was cut into squares with the same dimensions as the individual paper layers. To allow fluid to pass vertically, holes were made in relation to the designed flow path. As a result, the hydrophobic wax barriers constricted the flow in the lateral direction while the double-sided adhesive blocked flow in the vertical direction.

The design of the paper fluidic platform includes a viewing window of the control and test line for both biomarkers. This was incorporated into the design to remove the need to peel back the paper layers in order to see the results. However, by including a viewing window, the test region is exposed to the environment and is thereby influenced by additional factors including evaporation and humidity. A clear non-Raman active plastic sheet was placed over the nitrocellulose layer to keep it closed off. The transparent sheet was cut to include an inlet that aligned with an outlet from the layer above to allow the fluid to flow onto the nitrocellulose layer.

IV.3 Results and Discussion

IV.3.i Optimization of Conjugate Layer

The paper fluidic platform was optimized based on the function of the different paper layers. The conjugate layer was designed to store the gold nanoparticles functionalized with the universal sensing probe. Different volumes of functionalized

nanoparticles were tested to determine the optimal conditions. The signal intensity of the control line was obtained from the RGB values and used to determine the optimal value based on the highest signal intensity. Meanwhile, to ensure optimal resuspension of gold nanoparticles from conjugate layer, the RGB values on the conjugate storage region were collected. The RGB values were then used to determine if the conjugate region needed to be treated with a buffer and, if so, what volume was necessary. The buffer tested was 10% (*w/v*) BSA in 1X PBS.

Using 4 µL of functionalized gold nanoparticles, the results showed that a conjugate layer buffer was necessary to minimize nanoparticle loss to the membrane (Figure 27(a)). The minimal number of nanoparticles remaining on the conjugate region was observed at 2.5 µL and no further decrease in signal was observed for 3 µL. As a result, 2.5 µL of conjugate buffer was used to pretreat the conjugate region and used in determining the optimal nanoparticle volume (Figure 27(b)). The volume was tested using 1 µL, 1.5 µL, 2 µL, 2.5 µL, 3 µL, 3.5 µL and 4 µL. Since the control probe is the reverse

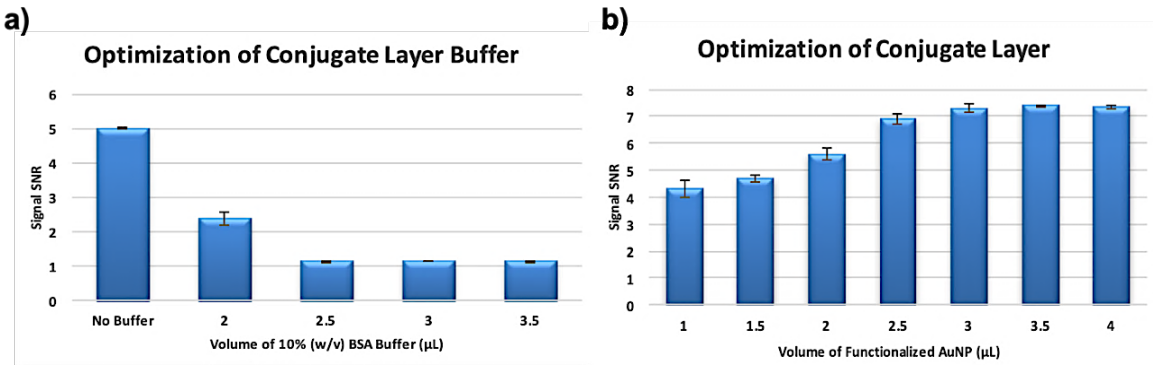

Figure 27 Optimization of conjugate layer in terms of a) conjugate buffer and b) nanoparticle volume

complement of the universal sensing probe, the addition of analytes (miRNA-17 and miRNA-20a) was not necessary. As such, the use of the control line rather than the test line avoided the use of an additional variable. The results showed that the signal intensity reached a maximum at 3 μL of nanoparticles. No increase in intensity was observed for larger nanoparticle volumes and it is believed that the control probes become saturated at 3 μL. Therefore, 2.5 μL of conjugate buffer and 3 μL of functionalized nanoparticles was used for all subsequent tests.

IV.3.ii Optimization of Mixing Layer

As done previously for the conjugate layer, the mixing layer was tested with different buffers. The function of the mixing layer is to promote interaction and binding between the universal sensing probes and target analytes. The amount of nanoparticles captured in the cellulose membrane of the mixing layer needs to be reduced to avoid loss of signal. It was previously determined that a minimal volume of 10 μL was required to coat the entire channel. 10 μL of buffers with 1%, 2%, and 3% (*w/v*) BSA in 1X M PBS with 0.1% (*v/v*) Tween-20 were tested. Tween-20 is a surfactant used to promote flow through the membrane but is also known to dislodge proteins immobilized on NC by absorption. Therefore, the amount of Tween-20 added to the buffer was minimal. As previously done, the RGB values of the control line were used in determining the optimal buffer conditions. (Figure 28)

An interesting trend was observed from the results for the different mixing layer buffers. The signal intensity increased from 1% to 2% BSA in buffer but at 3% no change

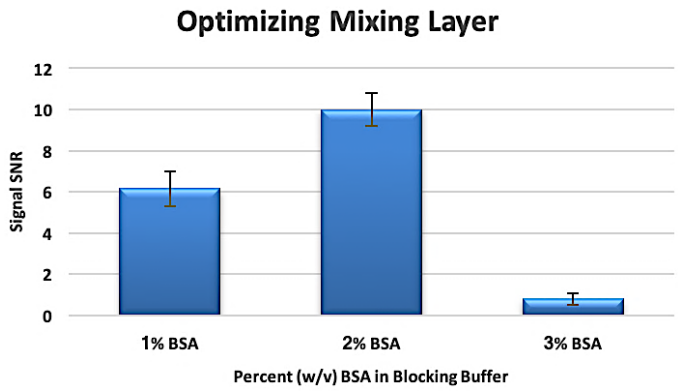

Figure 28 Optimization of mixing layer in regards to buffer conditions

in color was observed for the test line. In order to determine what had happened the 3D platform was deconstructed. Upon deconstruction, it was clearly observed that the flow of the resuspended nanoparticles had come to a stop halfway through the channel. This corresponds to the earlier observation in which only a clear solution was observed to flow over the test region. Based on this information, it is believed that at higher BSA concentrations the membrane becomes clogged and behaves like a filter. Therefore, 2% (*w/v*) BSA with 0.1% (*v/v*) Tween-20 in 1X M PBS was used to treat the mixing layer and is referred to as the Blocking Buffer.

IV.3.iii Testing of Paper Fluidic Platform

The optimized paper fluidic platform was tested using different concentrations of miRNA-17 and miRNA-20a. The SERS spectra were collected for concentrations from 100 pM too 100 fM for both miRNA-17 and miRNA-20a. Based on the obtained spectra provided in Figure 29 spectra were then analyzed based on the integrated peaks at 1177 cm^{-1} and 1618 cm^{-1}.

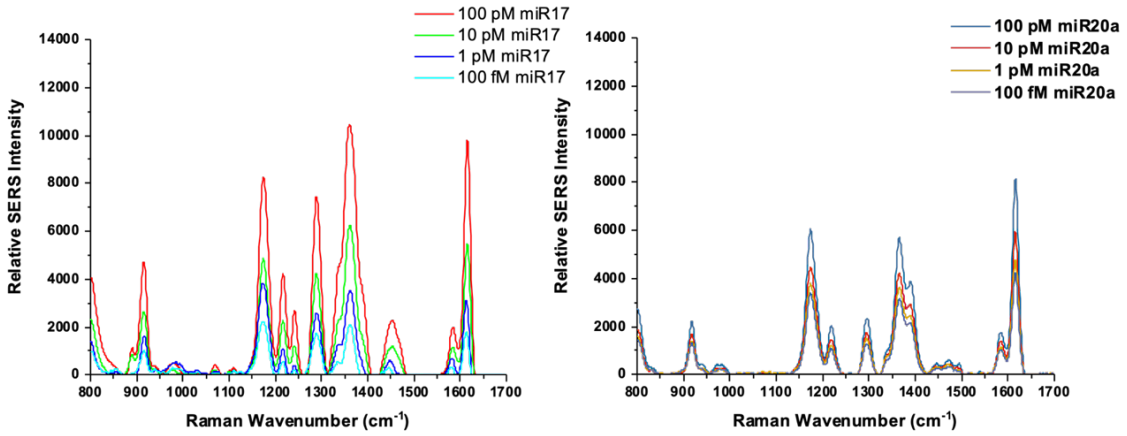

Figure 29 SERS spectra for miRNA-17 and miRNA-20a obtained from the designed 3D paper fluidic platform

IV.4 Summary

The paper fluidic device was designed using a combination of both lateral and vertical flow. The addition of vertical flow into our paper fluidic design allows us to easily incorporate and optimize for additional biomarkers with minimal influence on existing biomarkers. This new and substantially different approach to the early detection of PE using these novel early biomarkers, and a 3D layered paper-based device is expected to allow us to overcome the current limitations, particularly of producing robust SERS and of lateral flow POC tests, thereby opening new horizons for early PE detection.

CHAPTER V

CONCLUSIONS

The experiments and results included throughout this dissertation signify the adaptability of SERS detection assays for miRNA detection and its potential for point-of-care applications. While the transition to POCT still requires optimization and additional testing using human samples, the results presented support the application of multiplex miRNA sensing and quantification using the combination of SERS and paper fluidics. The 3D paper fluidic platform and SERS detection assay used in this dissertation include various optimization parameters, some of which have been exploited throughout this work, that can be explored for further optimization in future work.

The addition of a 3D paper fluidic platform for the purpose of transitioning toward POCT was one of the hallmarks of this work. Previously, very little work had been performed in the area of paper fluidics using a combination of lateral and vertical flow for optimized detection of miRNA using SERS. Moreover, the import of this work is enhanced in light of the potential application of this technology for use in the early detection of preeclampsia based on changes in miRNA concentration. Notably, diagnostic techniques for preeclampsia are currently heavily focused on the detection of proteinuria, which is a symptom that may or may not develop in women with preeclampsia. For this reason, exploring alternative biomarkers through new sensing technology, as done here, has the potential to improve diagnosis and treatment of preeclampsia.

Future work should focus on the application of this technology in clinical settings. Optimization of the paper fluidic platform will involve incorporating a blood separation membrane for testing both doped bovine samples and then moving to human clinical samples. A number of different commercial blood separation membranes are currently available. The degree of plasma separation that may be achieved with these commercially available membranes will need to be tested and optimized based on the necessary volume required to run the paper-based assay.

In addition, with the increase in plasma proteins resulting from more complex samples comes a need for a higher degree of specificity in the assay. A change from ssDNA oligonucleotides to customized peptide nucleic acids has the potential to improve the assay's sensing capacity. The use of PNA probes has been utilized in various publications and has shown improved specificity and selectivity.[190] The use of PNA probes provides the additional benefit of covalently immobilizing the sensing probes onto the NC surface.[191, 192] However, due to the limited availability of commercial PNA probes, their use coincides with increased costs.

In sum, this work highlights the development of a highly specific assay capable of detecting low concentrations of miRNAs in solution. Accordingly, the designed SERS detection assay is a promising diagnostic tool for the detection of blood-based biomarkers associated with the early onset of preeclampsia.

REFERENCES

1. Mahato, K., P.K. Maurya, and P. Chandra, *Fundamentals and commercial aspects of nanobiosensors in point-of-care clinical diagnostics.* 3 Biotech, 2018. **8**(3): p. 149.

2. Rangaswami, J., M. Naranjo, and P.A. McCullough, *Preeclampsia as a Form of Type 5 Cardiorenal Syndrome: An Underrecognized Entity in Women's Cardiovascular Health.* Cardiorenal Med, 2018. **8**(2): p. 160-172.

3. Vaught, A.J., et al., *Acute Cardiac Effects of Severe Pre-Eclampsia.* J Am Coll Cardiol, 2018. **72**(1): p. 1-11.

4. Bibbins-Domingo, K., et al., *Screening for Preeclampsia: US Preventive Services Task Force Recommendation Statement.* JAMA, 2017. **317**(16): p. 1661-1667.

5. Stevens, W., et al., *Short-term costs of preeclampsia to the United States health care system.* Am J Obstet Gynecol, 2017. **217**(3): p. 237-248.e16.

6. Poon, L.C., et al., *The International Federation of Gynecology and Obstetrics (FIGO) initiative on pre-eclampsia: A pragmatic guide for first-trimester screening and prevention.* Int J Gynaecol Obstet, 2019. **145**: p. 1-33.

7. Brown, M.A., et al., *The hypertensive disorders of pregnancy: ISSHP classification, diagnosis & management recommendations for international practice.* Pregnancy Hypertens, 2018. **13**: p. 291-310.

8. *ACOG Committee Opinion No. 743 Summary: Low-Dose Aspirin Use During Pregnancy.* Obstet Gynecol, 2018. **132**(1): p. 254-256.

9. LeFevre, M.L., *Low-dose aspirin use for the prevention of morbidity and mortality from preeclampsia: U.S. Preventive Services Task Force recommendation statement.* Ann Intern Med, 2014. **161**(11): p. 819-26.

10. Long, Q., et al., *Clinical practice patterns on the use of magnesium sulphate for treatment of pre-eclampsia and eclampsia: a multi-country survey.* BJOG, 2017. **124**(12): p. 1883-1890.

11. Riise, H.K., et al., *Incident Coronary Heart Disease After Preeclampsia: Role of Reduced Fetal Growth, Preterm Delivery, and Parity.* J Am Heart Assoc, 2017. **6**(3): p. e004158.

12. Adams, T., et al., *Long-term maternal morbidity and mortality associated with ischemic placental disease.* Semin Perinatol, 2014. **38**(3): p. 146-50.

13. Fox, R., et al., *Preeclampsia: Risk Factors, Diagnosis, Management, and the Cardiovascular Impact on the Offspring.* J Clin Med, 2019. **8**(10): p. 1625.

14. van Esch, J.J., et al., *Early-onset preeclampsia is associated with perinatal mortality and severe neonatal morbidity.* J Matern Fetal Neonatal Med, 2017: p. 1-6.

15. Petersen, E.E., et al., *Racial/ethnic disparities in pregnancy-related deaths—United States, 2007–2016.* Morb Mortal Wkly Rep, 2019. **68**(35): p. 762-765.

16. Vousden, N., et al., *Incidence of eclampsia and related complications across 10 low- and middle-resource geographical regions: Secondary analysis of a cluster randomised controlled trial.* PLoS Med, 2019. **16**(3): p. e1002775.

17. Silva, L.M., et al., *Low socioeconomic status is a risk factor for preeclampsia- the Generation R Study.* J Hypertens, 2008. **26**: p. 1200-1208.

18. *ACOG Practice Bulletin No. 202: Gestational Hypertension and Preeclampsia.* Obstet Gynecol, 2019. **133**(1): p. e1-e25.

19. Shahul, S., et al., *Racial Disparities in Comorbidities, Complications, and Maternal and Fetal Outcomes in Women With Preeclampsia/eclampsia.* Hypertens Pregnancy, 2015. **34**(4): p. 506-515.

20. Breathett, K., et al., *Differences in preeclampsia rates between African American and Caucasian women: trends from the National Hospital Discharge Survey.* J Womens Health (Larchmt), 2014. **23**(11): p. 886-93.

21. Magee, L.A. and P. von Dadelszen, *State-of-the-Art Diagnosis and Treatment of Hypertension in Pregnancy.* Mayo Clin Proc, 2018. **93**(11): p. 1664-1677.

22. Duhig, K., B. Vandermolen, and A. Shennan, *Recent advances in the diagnosis and management of pre-eclampsia.* F1000Res, 2018. **7**: p. 242.

23. Cerdeira, A.S., et al., *Randomized Interventional Study on Prediction of Preeclampsia/Eclampsia in Women With Suspected Preeclampsia: INSPIRE.* Hypertension, 2019. **74**(4): p. 983-990.

24. National Institute for Health and Care Excellence (NICE). *Hypertension in pregnancy: diagnosis and management*. NICE Guideline [NG133]. 2019 [cited 2019 November 18]; Available from: www.nice.org.uk/guidance/ng133.

25. Bernstein, P.S., et al., *National Partnership for Maternal Safety: Consensus Bundle on Severe Hypertension During Pregnancy and the Postpartum Period.* Obstet Gynecol, 2017. **130**(2): p. 347-357.

26. Leeman, L., L.T. Dresang, and P. Fontaine, *Hypertensive Disorders of Pregnancy.* Am Fam Physician, 2016. **93**(2): p. 121-7.

27. Bell, M.J., *A Historical Overview of Preeclampsia-Eclampsia.* J Obstet Gynecol Neonatal Nurs, 2010. **39**(5): p. 510-518.

28. Landeck, L., et al., *Biomarkers and personalized medicine: current status and further perspectives with special focus on dermatology.* Exp Dermatol, 2016. **25**(5): p. 333-9.

29. Lock, E.A. and J.V. Bonventre, *Biomarkers in translation; past, present and future.* Toxicology, 2008. **245**(3): p. 163-6.

30. Chuang, J.C. and P.A. Jones, *Epigenetics and microRNAs.* Pediatr Res, 2007. **61**(5 Pt 2): p. 24R-29R.

31. Leavey, K., et al., *Epigenetic regulation of placental gene expression in transcriptional subtypes of preeclampsia.* Clin Epigenetics, 2018. **10**: p. 28.

32. Choudhury, M., et al., *Epigenetics and microRNA as a unifying mechanism in severe preeclampsia.* Am J Obstet Gynecol, 2014. **210**(1): p. S5.

33. Choudhury, M. and J.E. Friedman, *Epigenetics and microRNAs in preeclampsia.* Clin Exp Hypertens, 2012. **34**(5): p. 334-41.

34. Kamrani, A., et al., *The role of epigenetic changes in preeclampsia.* Biofactors, 2019. **45**(5): p. 712-724.

35. Dong, H., et al., *MicroRNA: function, detection, and bioanalysis.* Chem Rev, 2013. **113**(8): p. 6207-33.

36. Ouyang, T., et al., *MicroRNA Detection Specificity: Recent Advances and Future Perspective.* Anal Chem, 2019. **91**(5): p. 3179-3186.

37. *Circulating microRNAs in Disease Diagnostics and their Potential Biological Relevance*. 1 ed. Experientia Supplementum. 2015: Springer Basel.

38. Weber, J.A., et al., *The microRNA spectrum in 12 body fluids.* Clin Chem, 2010. **56**(11): p. 1733-41.

39. Zhu, C.S., et al., *Avenues Toward microRNA Detection In Vitro: A Review of Technical Advances and Challenges.* Comput Struct Biotechnol J, 2019. **17**: p. 904-916.

40. Blondal, T., et al., *Assessing sample and miRNA profile quality in serum and plasma or other biofluids.* Methods, 2013. **59**(1): p. S1-6.

41. D'Agata, R. and G. Spoto, *Advanced methods for microRNA biosensing: a problem-solving perspective.* Anal Bioanal Chem, 2019. **411**(19): p. 4425-4444.

42. de Planell-Saguer, M. and M.C. Rodicio, *Analytical aspects of microRNA in diagnostics: a review.* Anal Chim Acta, 2011. **699**(2): p. 134-52.

43. Clancy, E., et al., *Amplification-free detection of microRNAs via a rapid microarray-based sandwich assay.* Anal Bioanal Chem, 2017. **409**(14): p. 3497-3505.

44. Woolley, A.T., *ABC Spotlight on emerging microRNA analysis methods.* Anal Bioanal Chem, 2015. **407**(22): p. 6579-81.

45. Wu, L., et al., *Circulating microRNAs are elevated in plasma from severe preeclamptic pregnancies.* Reproduction, 2012. **143**(3): p. 389-97.

46. Bounds, K.R., et al., *MicroRNAs: New Players in the Pathobiology of Preeclampsia.* Front Cardiovasc Med, 2017. **4**: p. 60.

47. Choudhury, M., et al., *8: Epigenetics and microRNA as a unifying mechanism in severe preeclampsia.* Am J Obstet Gynecol, 2014. **210**(1): p. S5.

48. Heegaard, N.H.H., et al., *Circulating Extracellular microRNA in Systemic Autoimmunity*, in *Circulating microRNAs in Disease Diagnostics and their Potential Biological Relevance*, P. Igaz, Editor. 2015, Springer Basel: Basel. p. 171-195.

49. Turchinovich, A., L. Weiz, and B. Burwinkel, *Extracellular miRNAs: the mystery of their origin and function.* Trends Biochem Sci, 2012. **37**(11): p. 460-5.

50. Kwan, J.Y., et al., *The complexity of microRNAs in human cancer.* J Radiat Res, 2016. **57**(S1): p. i106-i111.

51. Zhang, L., et al., *Individual Au-Nanocube Based Plasmonic Nanoprobe for Cancer Relevant MicroRNA Biomarker Detection.* ACS Sens, 2017. **2**(10): p. 1435-1440.

52. Zhang, H., et al., *A magnetic-based SERS approach for highly sensitive and reproducible detection of cancer-related serum microRNAs.* Anal Methods, 2018. **10**(6): p. 624-633.

53. Vaca, L., *Point-of-care diagnostic tools to detect circulating microRNAS as biomarkers of disease.* Sensors, 2014. **14**(5): p. 9117-31.

54. Kilic, T., et al., *microRNA biosensors: Opportunities and challenges among conventional and commercially available techniques.* Biosens Bioelectron, 2018. **99**: p. 525-546.

55. Johnson, B.N. and R. Mutharasan, *Biosensor-based microRNA detection: techniques, design, performance, and challenges.* Analyst, 2014. **139**(7): p. 1576-88.

56. Tian, T., J. Wang, and X. Zhou, *A review: microRNA detection methods.* Org Biomol Chem, 2015. **13**(8): p. 2226-38.

57. Koshiol, J., et al., *Strengths and limitations of laboratory procedures for microRNA detection.* Cancer Epidemiol Biomarkers Prev, 2010. **19**(4): p. 907-11.

58. Chandrasekaran, A.R., et al., *DNA nanotechnology approaches for microRNA detection and diagnosis.* Nucleic Acids Res, 2019. **47**(20): p. 10489-10505.

59. Hunt, E.A., et al., *MicroRNA Detection: Current Technology and Research Strategies.* Annu Rev Anal Chem, 2015. **8**: p. 217-37.

60. de Planell-Saguer, M. and M.C. Rodicio, *Detection methods for microRNAs in clinic practice.* Clin Biochem, 2013. **46**(10-11): p. 869-78.

61. Hartman, M., et al., *National Health Care Spending In 2018: Growth Driven By Accelerations In Medicare And Private Insurance Spending.* Health Aff (Millwood), 2020. **39**(1): p. 8-17.

62. Sikaris, K.A., *Enhancing the Clinical Value of Medical Laboratory Testing.* Clin Biochem Rev, 2017. **38**(3): p. 107-114.

63. Sautter, R.L., D.M. Earnest, and D.C. Halstead, *What's Old Is New Again: Laboratory Oversight of Point of Care Testing—Guidelines, Challenges, and Practical Strategies.* Clin Microbiol Newsl, 2018. **40**(23): p. 191-198.

64. Wang, P. and L.J. Kricka, *Current and Emerging Trends in Point-of-Care Technology and Strategies for Clinical Validation and Implementation.* Clin Chem, 2018. **64**(10): p. 1439-1452.

65. Rohr, U.P., et al., *The Value of In Vitro Diagnostic Testing in Medical Practice: A Status Report.* PLoS One, 2016. **11**(3): p. e0149856.

66. Haleyur Giri Setty, M.K. and I.K. Hewlett, *Point of Care Technologies for HIV.* AIDS Res Treat, 2014. **2014**: p. 497046.

67. Primiceri, E., et al., *Key Enabling Technologies for Point-of-Care Diagnostics.* Sensors, 2018. **18**(11).

68. Barbosa, A.I. and N.M. Reis, *A critical insight into the development pipeline of microfluidic immunoassay devices for the sensitive quantitation of protein biomarkers at the point of care.* Analyst, 2017. **142**(6): p. 858-882.

69. Gubala, V., et al., *Point of care diagnostics: status and future.* Anal Chem, 2012. **84**(2): p. 487-515.

70. Verbakel, J.Y., et al., *Common evidence gaps in point-of-care diagnostic test evaluation: a review of horizon scan reports.* BMJ Open, 2017. **7**(9): p. e015760.

71. Sohn, A.J., J.M. Hickner, and F. Alem, *Use of Point-of-Care Tests (POCTs) by US Primary Care Physicians.* J Am Board Fam Med, 2016. **29**(3): p. 371-6.

72. Shaw, J.L.V., *Practical challenges related to point of care testing.* Pract Lab Med, 2016. **4**: p. 22-29.

73. Kettler, H., K. White, and S. Hawkes, *Mapping the landscape of diagnostics for sexually transmitted infections*, in *Special Programme for Research and Training in Tropical Diseases*, U.U.W.B. World Health Organization, Editor. 2004, World Health Organization (WHO).

74. Smith, S., et al., *The potential of paper-based diagnostics to meet the ASSURED criteria.* RSC Adv, 2018. **8**(59): p. 34012-34034.

75. Land, K.J., et al., *REASSURED diagnostics to inform disease control strategies, strengthen health systems and improve patient outcomes.* Nat Microbiol, 2019. **4**(1): p. 46-54.

76. Gao, B., et al., *Emerging paper microfluidic devices.* Analyst, 2019. **144**(22): p. 6497-6511.

77. Darwish, N.T., S.D. Sekaran, and S.M. Khor, *Point-of-care tests: A review of advances in the emerging diagnostic tools for dengue virus infection.* Sens Actuators B Chem, 2018. **255**: p. 3316-3331.

78. Ahn, H., et al., *Emerging optical spectroscopy techniques for biomedical applications—A brief review of recent progress.* Appl Spectrosc Rev, 2017. **53**(2-4): p. 264-278.

79. Yang, J., et al., *Detection platforms for point-of-care testing based on colorimetric, luminescent and magnetic assays: A review.* Talanta, 2019. **202**: p. 96-110.

80. Li, P., et al., *Fundamentals and applications of surface-enhanced Raman spectroscopy–based biosensors.* Curr Opin Biomed Eng, 2020. **13**: p. 51-59.

81. Choi, J.R., et al., *Advances and challenges of fully integrated paper-based point-of-care nucleic acid testing.* Trends Analyt Chem, 2017. **93**: p. 37-50.

82. Yamada, K., et al., *Toward practical application of paper-based microfluidics for medical diagnostics: state-of-the-art and challenges.* Lab Chip, 2017. **17**(7): p. 1206-1249.

83. Martinez, A.W., S.T. Phillips, and G.M. Whitesides, *Diagnostics for the Developing World- Microfluidic Paper-Based Analytical Devices.* Anal Chem, 2010. **82**(1): p. 3-10.

84. Channon, R.B., et al., *Critical Components and Innovations in Paper-Based Analytical Devices*, in *Paper-based Diagnostics: Current Status and Future Applications*, K.J. Land, Editor. 2019, Springer International Publishing: Cham. p. 47-87.

85. Yetisen, A.K., M.S. Akram, and C.R. Lowe, *Paper-based microfluidic point-of-care diagnostic devices.* Lab Chip, 2013. **13**(12): p. 2210-51.

86. Hristov, D.R., et al., *Designing Paper-Based Immunoassays for Biomedical Applications.* Sensors, 2019. **19**(3): p. 554.

87. Credou, J. and T. Berthelot, *Cellulose: from biocompatible to bioactive material.* J Mater Chem B, 2014. **2**(30): p. 4767-4788.

88. Sher, M., et al., *Paper-based analytical devices for clinical diagnosis: recent advances in the fabrication techniques and sensing mechanisms.* Expert Rev Mol Diagn, 2017. **17**(4): p. 351-366.

89. Hosseini, S., P. Vázquez-Villegas, and S.O. Martínez-Chapa, *Paper and Fiber-Based Bio-Diagnostic Platforms: Current Challenges and Future Needs.* Applied Sciences, 2017. **7**(8): p. 863.

90. Hurk, R.V.d. and S. Evoy, *A Review of Membrane-Based Biosensors for Pathogen Detection.* Sensors, 2015. **15**(6): p. 14045-14078.

91. Petryayeva, E. and W.R. Algar, *Toward point-of-care diagnostics with consumer electronic devices: the expanding role of nanoparticles.* RSC Adv, 2015. **5**(28): p. 22256-22282.

92. Almeida, M.I.G.S., et al., *Developments of microfluidic paper-based analytical devices (μPADs) for water analysis: A review.* Talanta, 2018. **177**: p. 176-190.

93. Dou, M., et al., *Low-cost bioanalysis on paper-based and its hybrid microfluidic platforms.* Talanta, 2015. **145**: p. 43-54.

94. Yang, Y., et al., *Paper-Based Microfluidic Devices: Emerging Themes and Applications.* Anal Chem, 2017. **89**(1): p. 71-91.

95. Jiang, N., et al., *Lateral and Vertical Flow Assays for Point-of-Care Diagnostics.* Adv Healthc Mater, 2019. **8**(14): p. e1900244.

96. Borse, V. and R. Srivastava, *Process parameter optimization for lateral flow immunosensing.* Materials Science for Energy Technologies, 2019. **2**(3): p. 434-441.

97. Kuswandi, B. and A.A. Ensafi, *Perspective—Paper-Based Biosensors: Trending Topic in Clinical Diagnostics Developments and Commercialization.* J Electrochem Soc, 2019. **167**(3).

98. Holstein, C.A., et al., *Immobilizing affinity proteins to nitrocellulose: a toolbox for paper-based assay developers.* Anal Bioanal Chem, 2016. **408**(5): p. 1335-46.

99. Quesada-González, D. and A. Merkoçi, *Nanoparticle-based lateral flow biosensors.* Biosens Bioelectron, 2015. **73**: p. 47-63.

100. Lim, W.Y., B.T. Goh, and S.M. Khor, *Microfluidic paper-based analytical devices for potential use in quantitative and direct detection of disease biomarkers in clinical analysis.* J Chromatogr B Analyt Technol Biomed Life Sci, 2017. **1060**: p. 424-442.

101. Fu, L.-M. and Y.-N. Wang, *Detection methods and applications of microfluidic paper-based analytical devices.* Trends Analyt Chem, 2018. **107**: p. 196-211.

102. Ma, J., et al., *Paper Microfluidics for Cell Analysis.* Adv Healthc Mater, 2019. **8**(1): p. e1801084.

103. Akyazi, T., L. Basabe-Desmonts, and F. Benito-Lopez, *Review on microfluidic paper-based analytical devices towards commercialisation.* Analytica Chimica Acta, 2018. **1001**: p. 1-17.

104. Ahmed, S., M.P. Bui, and A. Abbas, *Paper-based chemical and biological sensors: Engineering aspects.* Biosens Bioelectron, 2016. **77**: p. 249-63.

105. Joung, H.A., et al., *Paper-based multiplexed vertical flow assay for point-of-care testing.* Lab Chip, 2019. **19**(6): p. 1027-1034.

106. Schonhorn, J.E., et al., *A device architecture for three-dimensional, patterned paper immunoassays.* Lab Chip, 2014. **14**(24): p. 4653-8.

107. Loo, J.F.C., et al., *Integrated Printed Microfluidic Biosensors.* Trends Biotechnol, 2019. **37**(10): p. 1104-1120.

108. Chen, P., et al., *Paper-based Vertical Flow Immunoassay (VFI) for detection of bio-threat pathogens.* Talanta, 2019. **191**: p. 81-88.

109. Das, R.S. and Y.K. Agrawal, *Raman spectroscopy: Recent advancements, techniques and applications.* Vib Spectrosc, 2011. **57**(2): p. 163-176.

110. McCreery, R.L., *Raman Spectroscopy for Chemical Analysis*. Vol. 225. 2005, New York: John Wiley & Sons.

111. Rostron, P. and D. Gerber, *Raman Spectroscopy, a review.* Int J Res Eng Technol, 2016. **6**: p. 50-64.

112. Lewandowska, R., *Raman Microscopy: Analysis of Nanomaterials*, in *Encyclopedia of Materials: Science and Technology*, K.H.J. Buschow, et al., Editors. 2010, Elsevier: Oxford. p. 1-6.

113. Xu, Z., et al., *Topic Review: Application of Raman Spectroscopy Characterization in Micro/Nano-Machining.* Micromachines, 2018. **9**(7).

114. Campion, A. and P. Kambhampati, *Surface-enhanced Raman scattering.* Chem Soc Rev, 1998. **27**(4): p. 241-250.

115. Petry, R., M. Schmitt, and J. Popp, *Raman spectroscopy--a prospective tool in the life sciences.* ChemPhysChem, 2003. **4**(1): p. 14-30.

116. Langer, J., et al., *Present and Future of Surface-Enhanced Raman Scattering.* ACS Nano, 2020. **14**(1): p. 28-117.

117. Lee, H.K., et al., *Designing surface-enhanced Raman scattering (SERS) platforms beyond hotspot engineering: emerging opportunities in analyte manipulations and hybrid materials.* Chem Soc Rev, 2019. **48**(3): p. 731-756.

118. Schlücker, S., *Surface-Enhanced Raman Spectroscopy-Concepts and Chemical Applications.* Angew Chem Int Ed, 2014. **53**: p. 4756-4795.

119. Guo, L., et al., *Strategies for enhancing the sensitivity of plasmonic nanosensors.* Nano Today, 2015. **10**(2): p. 213-239.

120. Pilot, R., et al., *A Review on Surface-Enhanced Raman Scattering.* Biosensors, 2019. **9**(2).

121. Willets, K.A. and R.P. Van Duyne, *Localized surface plasmon resonance spectroscopy and sensing.* Annu Rev Phys Chem, 2007. **58**: p. 267-297.

122. Meyer, S.A., E.C. Le Ru, and P.G. Etchegoin, *Combining surface plasmon resonance (SPR) spectroscopy with surface-enhanced Raman scattering (SERS).* Anal Chem, 2011. **83**(6): p. 2337-44.

123. Gu, X., et al., *SERS Sensors: Recent Developments and a Generalized Classification Scheme Based on the Signal Origin.* Annu Rev Anal Chem, 2018. **11**(1): p. 147-169.

124. Su, K.H., et al., *Interparticle Coupling Effects on Plasmon Resonances of Nanogold Particles.* Nano Lett, 2003. **3**(8): p. 1087-1090.

125. Langer, J., et al., *Present and Future of Surface-Enhanced Raman Scattering.* ACS Nano, 2020. **14**(1): p. 28-117.

126. Hering, K., et al., *SERS: a versatile tool in chemical and biochemical diagnostics.* Anal Bioanal Chem, 2008. **390**(1): p. 113-24.

127. Wang, Y., B. Yan, and L. Chen, *SERS tags: novel optical nanoprobes for bioanalysis.* Chem Rev, 2013. **113**(3): p. 1391-428.

128. Wang, Z., et al., *SERS-Activated Platforms for Immunoassay: Probes, Encoding Methods, and Applications.* Chem Rev, 2017. **117**(12): p. 7910-7963.

129. Jackson, J.B. and N.J. Halas, *Surface-enhanced Raman scattering on tunable plasmonic nanoparticle substrates.* PNAS, 2004. **101**(52): p. 17930-17935.

130. Guerrini, L. and D. Graham, *Molecularly-mediated assemblies of plasmonic nanoparticles for Surface-Enhanced Raman Spectroscopy applications.* Chem Soc Rev, 2012. **41**(21): p. 7085-107.

131. Walton, B.M., et al., *Surface-enhanced Raman spectroscopy competitive binding biosensor development utilizing surface modification of silver nanocubes and a citrulline aptamer.* J Biomed Opt, 2017. **22**(7): p. 1-7.

132. Haes, A.J. and R.P. Van Duyne, *A Nanoscale Optical Biosensor: Sensitivity and Selectivity of an Approach Based on the Localized Surface Plasmon Resonance Spectroscopy of Triangular Silver Nanoparticles.* J Am Chem Soc, 2002. **124**(35): p. 10596-10604.

133. Cialla, D., et al., *Surface-enhanced Raman spectroscopy (SERS): progress and trends.* Anal Bioanal Chem, 2012. **403**(1): p. 27-54.

134. Betz, J.F., et al., *Simple SERS substrates: powerful, portable, and full of potential.* Phys Chem Chem Phys, 2014. **16**(6): p. 2224-39.

135. Granger, J.H., et al., *Prospects for point-of-care pathogen diagnostics using surface-enhanced Raman scattering (SERS).* Chem Soc Rev, 2016. **45**(14): p. 3865-82.

136. Leopold, N. and B. Lendl, *A new method for fast preparation of highly surface-enhanced Raman scattering (SERS) active silver colloids at room temperature by reduction of silver nitrate with hydroxylamine hydrochloride.* J Phys Chem, 2003. **107**: p. 5723-5727.

137. Michota, A. and J. Bukowska, *Surface-enhanced Raman scattering (SERS) of 4-mercaptobenzoic acid on silver and gold substrates.* J Raman Spectrosc, 2003. **34**(1): p. 21-25.

138. Lin, C.C., et al., *A new protein A assay based on Raman reporter labeled immunogold nanoparticles.* Biosens Bioelectron, 2008. **24**(2): p. 178-83.

139. Batista, E., et al., *Using Polycarbonate Membranes as Templates for the Preparation of Au Nanostructures for Surface-Enhanced Raman Scattering.* J Nanosci Nanotechnol, 2009. **9**(5): p. 3233-3238.

140. Israelsen, N.D., C. Hanson, and E. Vargis, *Nanoparticle properties and synthesis effects on surface-enhanced Raman scattering enhancement factor: an introduction.* ScientificWorldJournal, 2015. **2015**: p. 124582.

141. Chang, C.-W.C.J.-D.L.H.-C., et al., *Fabrication of nano-indented cavities on Au for the detection of chemically-adsorbed DTNB molecular probes through SERS effect.* J Colloid Interface Sci, 2011. **358**: p. 384-391.

142. Reichman, J., *Handbook of Optical Filters for Fluorescence Microscopy*. 1998: Chroma Technology Corp.

143. Guven, B., et al., *SERS-based direct and sandwich assay methods for mir-21 detection.* Analyst, 2014. **139**(5): p. 1141-7.

144. Wang, Y., et al., *Direct detection of microRNA based on plasmon hybridization of nanoparticle dimers.* Analyst, 2015. **140**(4): p. 1140-8.

145. Donnelly, T., K. Faulds, and D. Graham, *Investigation of Silver Nanoparticle Assembly Following Hybridization with Different Lengths of DNA.* Part Part Syst Charact, 2016. **33**(7): p. 404-411.

146. Barrett, L., et al., *Stable dye-labelled oligonucleotide-nanoparticle conjugates for nucleic acid detection.* Nanoscale, 2011. **3**(8): p. 3221-7.

147. Mabbott, S., et al., *From synthetic DNA to PCR product: detection of fungal infections using SERS.* Faraday Discuss, 2016. **187**: p. 461-72.

148. Dougan, J.A., et al., *Enhanced oligonucleotide-nanoparticle conjugate stability using thioctic acid modified oligonucleotides.* Nucleic Acids Res, 2007. **35**(11): p. 3668-75.

149. Laing, S., K. Gracie, and K. Faulds, *Multiplex in vitro detection using SERS.* Chem Soc Rev, 2016. **45**(7): p. 1901-18.

150. Pekdemir, M.E., et al., *Ultrasensitive and selective homogeneous sandwich immunoassay detection by Surface Enhanced Raman Scattering (SERS).* Analyst, 2012. **137**(20): p. 4834-40.

151. Donnelly, T., et al., *Silver and magnetic nanoparticles for sensitive DNA detection by SERS.* Chem Commun, 2014. **50**(85): p. 12907-10.

152. *Thermo Scientific DXR Raman Microscope*. 2013, Thermo Scientific: Online.

153. *IDRaman mini*, in *Online*. 2017, Ocean Optics: https://oceanoptics.com//wp-content/uploads/IDRaman_Mini_Product_Sheet.pdf.

154. *IDRaman Reader Product Sheet*, in *Online*. 2017, Ocean Optics: https://oceanoptics.com//wp-content/uploads/IDRaman_Reader_Product_Sheet.pdf.

155. *IDRaman mini 2.0 Installation and Operation Manual*, in *Online*. 2015, Ocean Optics: https://oceanoptics.com/wp-content/uploads/IDRamanmini2manual.pdf.

156. Zhang, X., M.R. Servos, and J. Liu, *Fast pH-assisted functionalization of silver nanoparticles with monothiolated DNA.* Chem Commun, 2012. **48**(81): p. 10114-6.

157. Li, M., S.K. Cushing, and N. Wu, *Plasmon-enhanced optical sensors: a review.* Analyst, 2015. **140**(2): p. 386-406.

158. Kamińska, A., et al., *Highly reproducible, stable and multiply regenerated surface-enhanced Raman scattering substrate for biomedical applications.* J Mater Chem, 2011. **21**(24): p. 8662.

159. Grubisha, D.S., et al., *Femtomolar Detection of Prostate-Specific Antigen- An Immunoassay Based on Surface-Enhanced Raman Scattering and Immunogold Labels.* Anal Chem, 2003. **75**(21): p. 5936-5943.

160. Shrestha, Y.K. and F. Yan, *Determination of critical micelle concentration of cationic surfactants by surface-enhanced Raman scattering.* RSC Adv, 2014. **4**(70): p. 37274.

161. Lin, C.C. and C.W. Chang, *AuNPs@mesoSiO2 composites for SERS detection of DTNB molecule.* Biosens Bioelectron, 2014. **51**: p. 297-303.

162. Vo-Dinh, T., et al., *SERS nanosensors and nanoreporters: golden opportunities in biomedical applications.* WIREs Nanomed Nanobiotechnol, 2015. **7**(1): p. 17-33.

163. Schechinger, M., et al., *Development of a miRNA surface-enhanced Raman scattering assay using benchtop and handheld Raman systems.* J Biomed Opt, 2018. **23**(1): p. 1-11.

164. Graham, D., et al., *Control of enhanced Raman scattering using a DNA-based assembly process of dye-coded nanoparticles.* Nat Nanotechnol, 2008. **3**(9): p. 548-51.

165. Anker, J.N., et al., *Biosensing with plasmonic nanosensors.* Nat Mater, 2008. **7**: p. 442-453.

166. Faulds, K., A. Hernandez-Santana, and W.E. Smith, *The inorganic chemistry of surface enhanced Raman scattering (SERS)*, in *Spectroscopic Properties of Inorganic and Organometallic Compounds: Techniques, Materials and Applications*. 2010, The Royal Society of Chemistry. p. 1-21.

167. Alvarez-Puebla, R.A., et al., *Role of Nanoparticle Surface Charge in Surface-Enhanced Raman Scattering.* J Phys Chem B, 2005. **109**(9): p. 3787-3792.

168. Zhou, W., et al., *Simultaneous Surface-Enhanced Raman Spectroscopy Detection of Multiplexed MicroRNA Biomarkers.* Anal Chem, 2017. **89**(11): p. 6120-6128.

169. Lopez, M.I., I. Ruisanchez, and M.P. Callao, *Figures of merit of a SERS method for Sudan I determination at traces levels.* Spectrochim Acta A Mol Biomol Spectrosc, 2013. **111**: p. 237-41.

170. Gracie, K., et al., *Simultaneous detection and quantification of three bacterial meningitis pathogens by SERS.* Chem Sci, 2014. **5**(3): p. 1030-1040.

171. Lueck, H.B., D.C. Daniel, and J.L. McHale, *Resonance Raman Study of Solvent Effects on a Series of Triarylmethane Dyes.* J Raman Spectrosc, 1993. **24**: p. 363-370.

172. Atkins, C.G., et al., *Raman Spectroscopy of Blood and Blood Components.* Appl Spectrosc, 2017. **71**(5): p. 767-793.

173. Weaver, J., et al., *Sensitivity Limits for in vivo ELISA Measurements of Molecular Biomarker Concentrations.* Int J Mag Part Imag, 2017. **3**(2): p. 4.

174. Prinz, H., *Hill coefficients, dose-response curves and allosteric mechanisms.* J Chem Biol, 2010. **3**(1): p. 37-44.

175. Movasaghi, Z., S. Rehman, and I.U. Rehman, *Raman Spectroscopy of Biological Tissues.* Appl Spectrosc Rev, 2007. **42**(5): p. 493-541.

176. Talari, A.C.S., et al., *Raman Spectroscopy of Biological Tissues.* Appl Spectrosc Rev, 2014. **50**(1): p. 46-111.

177. Lin, M., et al., *Detection of melamine in gluten, chicken feed, and processed foods using surface enhanced Raman spectroscopy and HPLC.* J Food Sci, 2008. **73**(8): p. T129-34.

178. Golightly, R.S., W.E. Doering, and M.J. Natan, *Surface-Enhanced Raman Spectroscopy and Homeland Security: A Perfect Match?* ACS Nano, 2009. **3**(10): p. 2859-2869.

179. Zhang, H., et al., *SERS detection of microRNA biomarkers for cancer diagnosis using gold-coated paramagnetic nanoparticles to capture SERS-active gold nanoparticles.* RSC Adv, 2017. **7**(83): p. 52782-52793.

180. Laguna, M., et al., *Antigen-Antibody Affinity for Dry Eye Biomarkers by Label Free Biosensing. Comparison with the ELISA Technique.* Sensors, 2015. **15**(8): p. 19819-29.

181. Esteban Fernández de Ávila, B., et al., *Determinants of the Detection Limit and Specificity of Surface-Based Biosensors.* Anal Chem, 2013. **85**(14): p. 6593-6597.

182. Lu, Y., et al., *Fabrication and characterization of paper-based microfluidics prepared in nitrocellulose membrane by wax printing.* Anal Chem, 2010. **82**(1): p. 329-35.

183. Altundemir, S., A.K. Uguz, and K. Ulgen, *A review on wax printed microfluidic paper-based devices for international health.* Biomicrofluidics, 2017. **11**(4): p. 041501.

184. Carrilho, E., A.W. Martinez, and G.M. Whitesides, *Understanding Wax Printing: A Simple Micropatterning Process for Paper-Based Microfluidics.* Anal Chem, 2009. **81**(16): p. 7091-7095.

185. Schechinger, M., et al., *A SERS approach for rapid detection of microRNA-17 in the picomolar range.* Analyst, 2019. **144**(13): p. 4033-4044.

186. Nimse, S.B., et al., *Immobilization techniques for microarray: challenges and applications.* Sensors, 2014. **14**(12): p. 22208-29.

187. Enustun, B.V. and J. Turkevich, *Coagulation of Colloidal Gold.* J Am Chem Soc, 1963. **85**(21): p. 3317-3328.

188. Dolinnyi, A.I., *Extinction coefficients of gold nanoparticles and their dimers. Dependence of optical factor on particle size.* Colloid J, 2017. **79**(5): p. 611-620.

189. Tang, J., et al., *Calculation extinction cross sections and molar attenuation coefficient of small gold nanoparticles and experimental observation of their UV–vis spectral properties.* Spectrochim Acta A Mol Biomol Spectrosc, 2018. **191**: p. 513-520.

190. Gasparello, J., et al., *Demonstrating specificity of bioactive peptide nucleic acids (PNAs) targeting microRNAs for practical laboratory classes of applied biochemistry and pharmacology.* PLoS One, 2019. **14**(9): p. e0221923.

191. Wu, J.-c., et al., *Recent advances in peptide nucleic acid for cancer bionanotechnology.* Acta Pharmacologica Sinica, 2017. **38**(6): p. 798-805.

192. Gupta, A., et al., *Nanotechnology for delivery of peptide nucleic acids (PNAs).* J Control Release, 2016. **240**: p. 302-311.

APPENDIX A

SUPPLEMENTAL INFORMATION FROM PUBLICATIONS

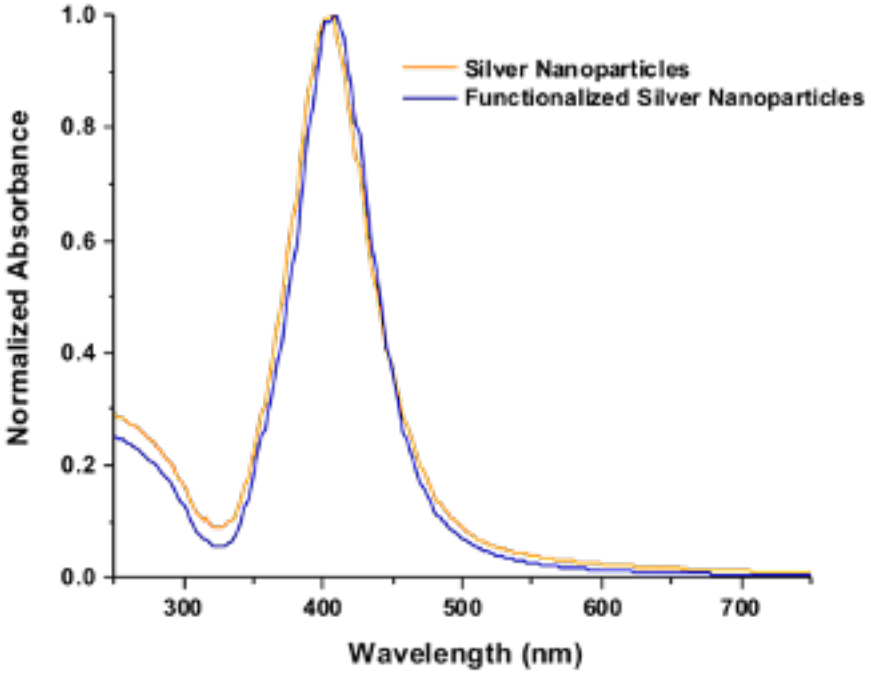

Figure S1 The absorption spectra of bare AgNPs and AgNPs functionalized with ssDNA capture probes

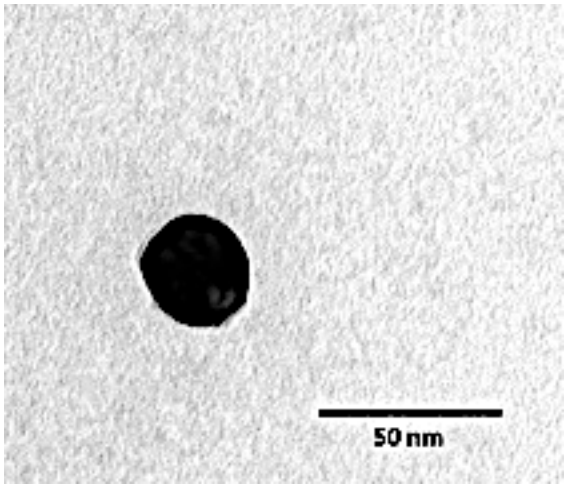

Figure S2 TEM image of synthesized AgNPs

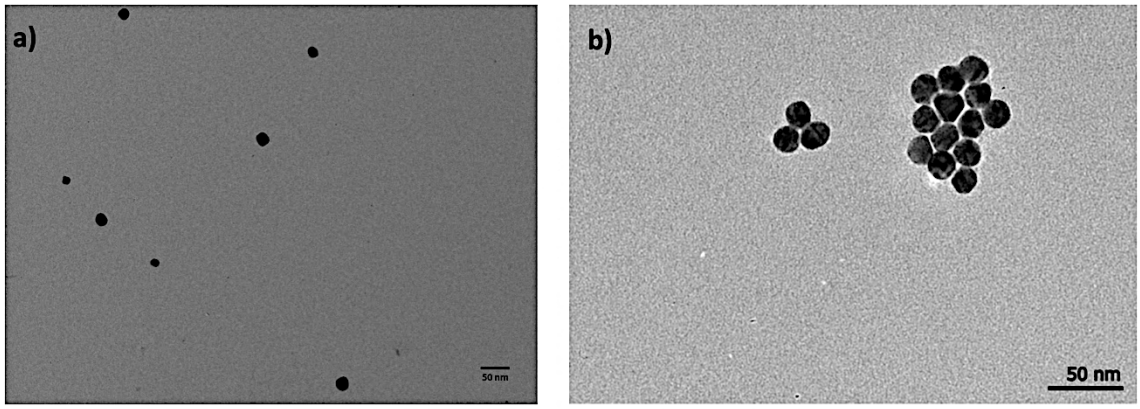

Figure S3 TEM images of (a) functionalized AgNPs without the presence of miRNA-17 and (b) the AgNPs plasmonic aggregates formed in the presence of the target analyte, miRNA-17. The images were obtained by combining the synthesized nanoparticle detection assay (AgNPs conjugated with Probe 1 and labelled with MGITC + AgNPs conjugated with Probe 2) with or without miRNA-17 target and allowing the solution to react at room temperature. The resultant aggregates that formed in response to miRNA-17 varied in the number of nanoparticles per cluster. aggregates ranges from 2 nanoparticles per cluster to an upward amount of 15 nanoparticles per cluster

Table S1 The intensity limit calculations of the blank for the characteristic peaks of MGITC

LIMIT OF DETECTION (LOD) CALCULATIONS USING LINEAR REGRESSION ANALYSIS						
	DETECTION ASSAY IN PBS			*DETECTION ASSAY IN 20% (v/v) BOVINE SERUM*		
	I_{tBlank}	SD_{tBlank}	I_{Limit}	I_{tBlank}	SD_{tBlank}	I_{Limit}
1177 cm^{-1}	3.2×10^4	1.5×10^3	3.70×10^4	6.8×10^4	1.1×10^4	7.95×10^4
1220 cm^{-1}	9.5×10^3	4.8×10^2	1.09×10^4	1.1×10^4	3.1×10^3	1.44×10^4
1290 cm^{-1}	9.2×10^3	6.7×10^2	1.12×10^4	2.4×10^4	3.6×10^3	2.78×10^4
1586 cm^{-1}	1.5×10^4	1.8×10^2	1.55×10^4	3.3×10^4	5.3×10^3	3.87×10^4
1618 cm^{-1}	2.5×10^4	1.6×10^3	2.99×10^4	4.6×10^4	7.5×10^3	5.31×10^4

Table S2 The target concentrations for the LOD calculated for the five characteristic peaks analyzed

LIMIT OF DETECTION (LOD) CALCULATIONS USING LINEAR REGRESSION ANALYSIS								
	DETECTION ASSAY IN PBS				*DETECTION ASSAY IN 20% (v/v) BOVINE SERUM*			
	y	k	m	LOD (M)	y	k	m	LOD (M)
1177 cm^{-1}	3.70E+04	3.60E+05	2.66E+04	6.89E-13	6.8E+04	7.42E+05	5.29E+04	1.82E-13
1220 cm^{-1}	1.09E+04	9.33E+04	6.84E+03	9.10E-13	1.1E+04	1.17E+05	8.38E+03	2.24E-13
1290 cm^{-1}	1.12E+04	9.24E+04	6.70E+03	7.62E-13	2.4E+04	2.22E+05	1.52E+04	9.41E-14
1586 cm^{-1}	1.55E+04	1.60E+05	1.13E+04	1.64E-13	3.3E+04	3.83E+05	2.64E+04	5.53E-14
1618 cm^{-1}	2.99E+04	2.16E+05	1.48E+04	2.62E-13	4.6E+04	5.20E+05	3.69E+04	1.43E-13

Table S3 Results of paired t-Test between consecutive target analyte concentrations

	PBS	10 nM	1 nM	100 pM	10 pM	1 pM	100 fM	10 fM
PBS		3.6E-4	0.0035	1.8E-4	7.7E-4	0.014	0.0023	0.0010
10 nM	52.8		0.62	8.5E-4	8.7E-4	4.2E-4	7.7E-5	2.3E-4
1 nM	16.9	0.579		0.027	0.014	0.012	0.0084	0.0074
100 pM	74.5	34.4	6.00		0.0023	0.0046	1.4E-4	2.0E-4
10 pM	36.1	33.9	8.33	21.0		0.031	0.0043	0.0021
1 pM	8.30	49.0	9.22	14.7	5.54		0.86	0.60
100 fM	20.8	114	10.8	85.1	15.3	0.196		0.14
10 fM	31.2	66.2	11.5	72.0	21.6	0.610	2.34	

Table S4 Paired t-Test of signal intensity at different miRNA-17 Target concentrations using the peak at 1618 cm^{-1}

	STATISTICAL ANALYSIS USING PAIRED t-TEST					
	DETECTION ASSAY IN PBS			*DETECTION ASSAY IN 20% (v/v) BOVINE SERUM*		
	t Value	**p Value**	**SIGNIFICANT**	**t Value**	**p Value**	**SIGNIFICANT**
PBS vs. 10 nM	52.8	0.00036	YES	19.4	0.0027	YES
10 nM vs. 1 nM	***-0.579***	***0.62***	***NO***	***23.5***	***0.144***	***NO***
1 nM vs. 100 pM	6.00	0.027	YES	-62.4	0.00026	YES
100 pM vs. 10 pM	21.0	0.023	YES	13.3	0.00056	YES
10 pM vs. 1 pM	5.54	0.031	YES	-12.7	0.0061	YES
1 pM vs. 100 fM	***0.196***	***0.86***	***NO***	***1.80***	***0.215***	***NO***
100 fM vs. 10 fM	***2.34***	***0.14***	***NO***	***12.1***	***0.052***	***NO***
10 fM vs. PBS	31.2	0.0010	YES	-50.6	0.00039	YES

Table S5 Hill equation coefficients for the characteristic peaks of MGITC

	DOSE-RESPONSE ANALYSIS USING HILL EQUATION											
	DETECTION ASSAY IN PBS						*DETECTION ASSAY IN 20% (v/v) BOVINE SERUM*					
	k (pM)	n	COD	R^2	START	END	k (pM)	n	COD	R^2	START	END
1177 cm^{-1}	0.129	0.820	0.990	0.977	4.67E+4	1.38E+5	8.58	1.15	0.997	0.994	8.94E+4	2.34E+5
1220 cm^{-1}	0.143	0.517	0.990	0.980	1.11E+4	3.93E+4	15.1	0.674	0.999	0.999	1.13E+4	4.19E+4
1290 cm^{-1}	0.155	0.692	0.998	0.995	1.35E+4	3.69E+4	9.01	0.849	0.999	0.999	2.56E+4	8.22E+4
1586 cm^{-1}	0.756	0.284	0.981	0.962	1.82E+4	8.74E+4	15.5	1.17	0.999	0.998	6.17E+4	1.41E+5
1618 cm^{-1}	0.196	0.471	0.990	0.981	3.97E+4	9.49E+4	28.5	0.618	0.998	0.995	6.88E+4	1.99E+5

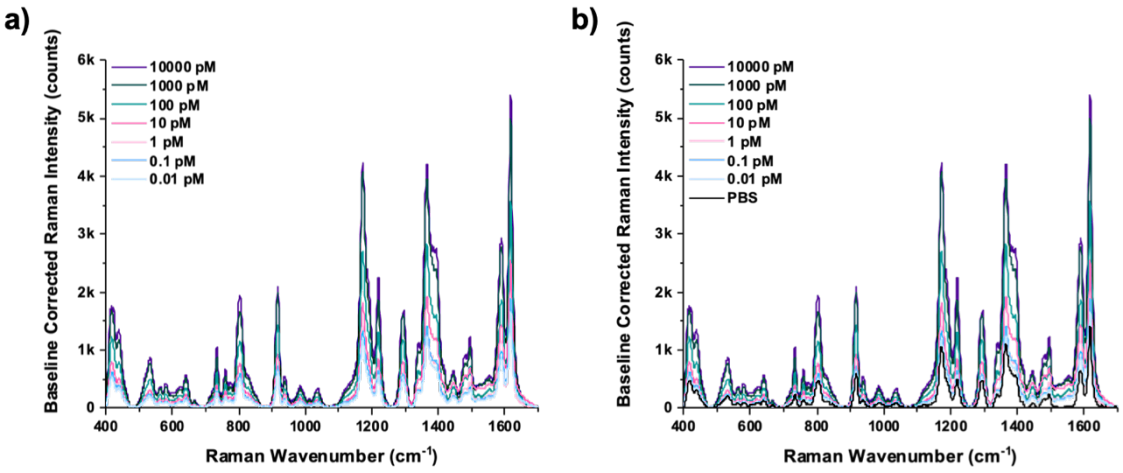

Figure S4 The (a) SERS plot of the entire concentration range of miRNA-17 target tested and (b) the plot of entire range of miRNA-17 and the assay without target (PBS)

Table S6 Summary of fit parameters from the linear regression analysis of the assay in PBS and diluted bovine serum

	LINEAR REGRESSION ANALYSIS									
	DETECTION ASSAY IN PBS					*DETECTION ASSAY IN 20% (v/v) BOVINE SERUM*				
PEAK (cm^{-1})	1180	1220	1290	1618	1620	1180	1220	1290	1618	1620
SLOPE	2.66E4	6.84E3	6.70E3	1.13E4	1.48E4	5.29E4	8.38E3	1.52E4	2.64E4	3.69E4
INTERCEPT	3.60E5	9.33E4	9.24E4	1.60E5	2.16E5	7.42E5	1.17E4	2.22E4	3.83E5	5.20E5
ADJ R-SQUARED	0.884	0.915	0.913	0.911	0.925	0.910	0.952	0.917	0.916	0.977
PEARSON'S R	0.961	0.971	0.970	0.970	0.975	0.969	0.984	0.972	0.972	0.992
R-SQUARE (COD)	0.923	0.943	0.942	0.941	0.950	0.940	0.952	0.945	0.944	0.985
F VALUE	23.9	33.2	32.3	31.8	38.0	31.2	129	33.8	34.1	60.1
p VALUE	0.0393	0.0289	0.0296	0.0300	0.0253	0.0306	0.00768	0.0284	0.0281	0.0162

Table S7 Summary of results of a One-Way ANOVA analysis of the SERS signal intensity to determine the significance of Raman peak location

	COMPARISON OF SERS SIGNAL INTENSITY VERSUS MIRNA-17 TARGET CONCENTRATION								
	DETECTION ASSAY IN PBS				*DETECTION ASSAY IN 20% (v/v) BOVINE SERUM*				
PEAK LOCATION	DF	SUM OF SQUARES	MEAN SQUARE	F	P-VALUE	SUM OF SQUARES	MEAN SQUARE	F	P-VALUE
1177 cm^{-1}	3	1.15E10	3.82E9	88.1	1.81E-6	3.36E10	1.12E10	146	2.52E-7
1220 cm^{-1}	3	7.43E8	2.48E8	21.5	3.50E-4	1.07E9	3.57E8	219	5.11E-8
1290 cm^{-1}	3	7.15E8	2.38E8	65.2	5.78E-6	4.37E9	1.46E9	178	1.16E-7
1586 cm^{-1}	3	2.03E9	6.77E8	60.8	7.53E-6	1.10E10	3.67E9	130	4.03E-7
1618 cm^{-1}	3	2.66E9	8.88E8	55.0	1.11E-5	2.03E10	6.75E9	113	6.79E-7

Table S8 Summary of results of a One-Way ANOVA analysis of the SERS signal intensity to determine the significance of the target concentration

	COMPARISON OF SERS SIGNAL INTENSITY WITH RAMAN PEAK LOCATION								
	DETECTION ASSAY IN PBS					*DETECTION ASSAY IN 20% (v/v) BOVINE SERUM*			
TARGET CONCENTRATION	DF	SUM OF SQUARES	MEAN SQUARE	F	P-VALUE	SUM OF SQUARES	MEAN SQUARE	F	P-VALUE
1 nM	4	1.91E10	4.78E9	78.1	1.68E-7	7.45E10	1.86E10	333	1.37E-10
100 pM	4	8.94E9	2.23E9	831	1.45E-12	5.99E10	1.50E10	301	2.24E-10
10 pM	4	4.37E9	1.09E9	859	1.23E-12	3.70E10	9.24E9	1350	1.27E-13
1 pM	4	3.21	8.02E8	272	3.74E-10	1.38E10	3.45E9	128	1.53E-8

Table S9 Paired t-Test of the signal intensity of the forward and reverse non-complementary strands of the negative control RNA

	FORWARD STRAND		REVERSE STRAND	
	t Value	p Value	t Value	p Value
miRNA 34-3p vs. PBS	0.904	0.42	-1.18	0.30
miRNA 126-3p vs. PBS	0.629	0.56	-1.56	0.19
miRNA 155-3p vs. PBS	2.38	0.076	-0.792	0.47
miRNA 210-3p vs. PBS	-1.06	0.35	-0.624	0.57
RNA U6 vs. PBS	-0.169	0.87	-0.670	0.54

Table S10 Vibrational peak assignment of the prominent Raman peaks of diluted bovine serum

PEAK (cm^{-1})	VIBRATIONAL MODE	MAJOR ASSIGNMENT
872	ν(C-C)	Tyrosine, Proline, Hydroxyproline
959	δ_{oop} (Deformed) Hydroxyapatite, carotenoid, cholesterol	Lipid, Protein
1004	ν_s(C-C)	Phenylalanine (Protein)
1157	ν(C-C) and ν(C-N)	β -Carotenoids (Protein)
1190	δ(C-H)	Tryptophan (Protein), Phenylalanine (Protein)
1210	Tryptophan and Phenylalanine	Tryptophan (Protein), Phenylalanine (Protein)
1269	ν(C-N), δ(N-H)	Amide III (Protein), Collagen
1351	CH_3CH_2 Wagging	Collagen (Protein)
1445	δ(CH_2)	Collagen (Protein), Phospholipids (Lipids)
1521	ν(C=C)	β -Carotenoids (Protein)
1593	δ(C=C)	Phenylalanine (Protein), Hemoglobin
1691	Amide 1, α-helix ν(C=O)	Protein, Phospholipids

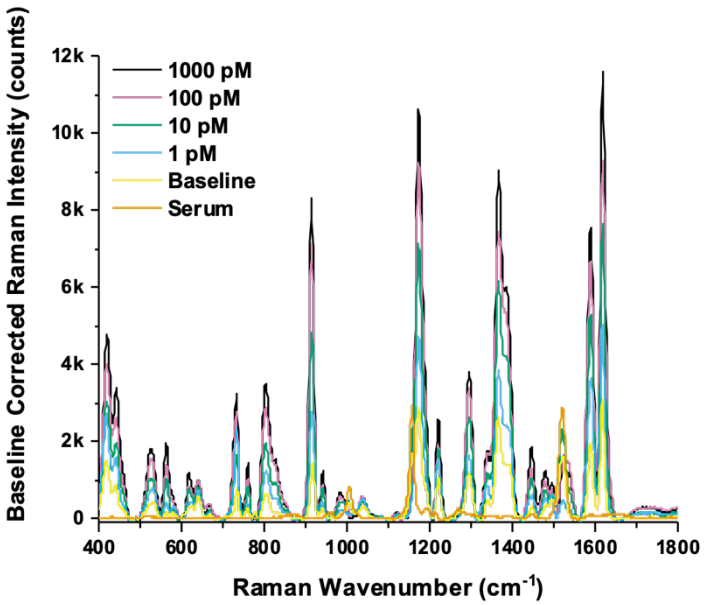

Figure S5 Raman spectra of the diluted bovine serum and the normalized SERS signal of the miRNA-17 detection assay tested in diluted bovine serum

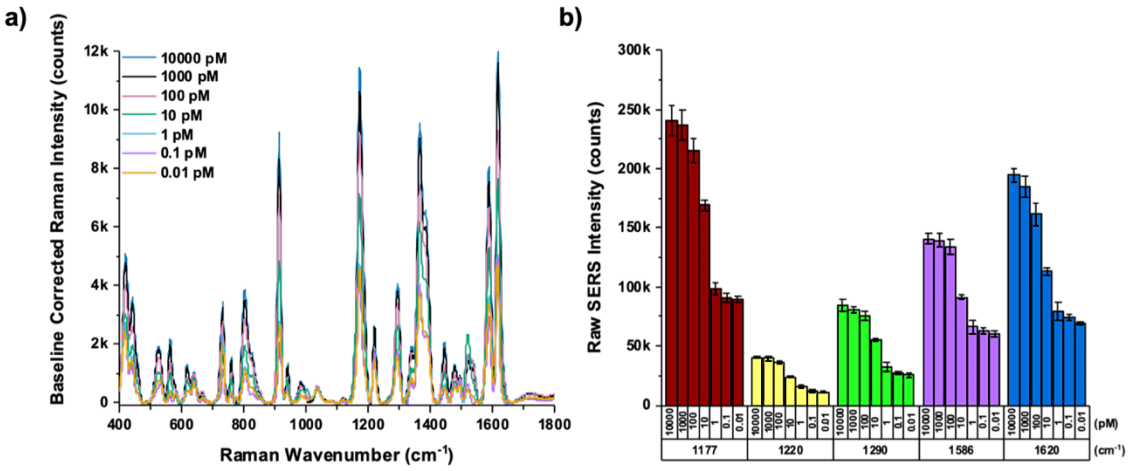

Figure S6 The (a) raw SERS spectra for the entire target range and (b) integrated peak area for the characteristic peak of MGITC centered at 1618 cm^{-1} for different concentrations of miRNA-17 suspended in diluted bovine serum

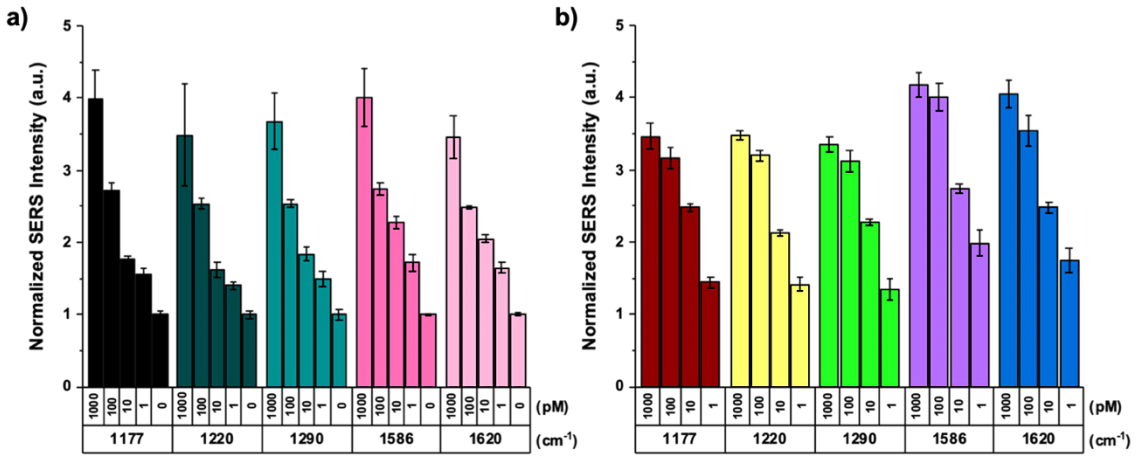

Figure S7 The normalized peak area of the for the characteristic peaks of MGITC at different concentrations of miRNA-17 for the assay in (a) PBS and(b) diluted bovine serum

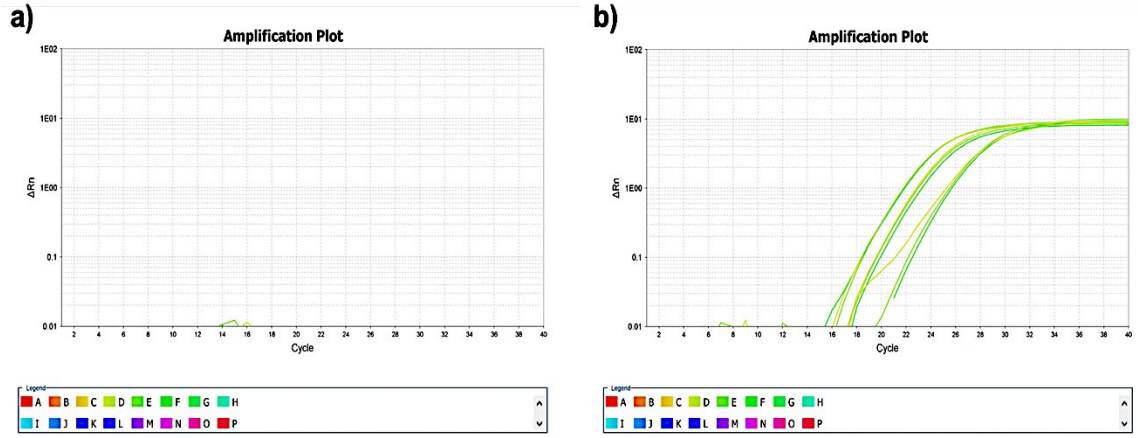

Figure S8 The resultant amplification plots obtained from the real-time reverse transcription PCR (qRT-PCR) for miRNA-17 in a) water and b) bovine serum solution

Table S11 Summary of flow parameters of both the cellulose and nitrocellulose membranes used in the designed 3D microfluidic paper-based analytical device

	Whatman Grade 1 Chromatography Paper	*FF120HP Nitrocellulose Membrane*
Thickness	180 μm	100 μm*
Weight	87 g/m^2	--
Pore Size/ Particle Retention	11 μm	--
Flow Rate	130 mm/ 30 min	4 cm/ 90-150 seconds

*Nitrocellulose membrane without backing